

ALMA MATER STUDIORUM - UNIVERSITÀ DI BOLOGNA

---

---

FACOLTÀ DI SCIENZE MATEMATICHE FISICHE E NATURALI  
DOTTORATO DI RICERCA IN FISICA, XXI CICLO

Ph.D. Thesis

# **Drift Tubes Trigger System of the CMS Experiment at LHC : Commissioning and Performances**

Dott. Carlo Battilana

Advisor:

Chiar.mo Prof.

PAOLO CAPILUPPI

Co-Advisor:

Dott.

STEFANO MARCELLINI

Ph.D. Coordinator:

Chiar.mo Prof.

FABIO ORTOLANI

---

---

Bologna, Italy, March 2009



ALMA MATER STUDIORUM - UNIVERSITÀ DI BOLOGNA

---

---

FACOLTÀ DI SCIENZE MATEMATICHE FISICHE E NATURALI  
DOTTORATO DI RICERCA IN FISICA, XXI CICLO

Ph.D. Thesis

# **Drift Tubes Trigger System of the CMS Experiment at LHC : Commissioning and Performances**

Dott. Carlo Battilana

Advisor:

Chiar.mo Prof.

PAOLO CAPILUPPI

Co-Advisor:

Dott.

STEFANO MARCELLINI

Ph.D. Coordinator:

Chiar.mo Prof.

FABIO ORTOLANI

FIS/01

---

---

Bologna, Italy, March 2009



# Contents

<b>Introduction</b>	<b>7</b>
<b>1 The LHC Project</b>	<b>9</b>
1.1 The Large Hadron Collider . . . . .	9
1.2 Physics at the LHC . . . . .	13
1.2.1 Cross Sections and Rates . . . . .	15
1.2.2 Higgs Search . . . . .	17
1.2.3 Standard Model Physics and Precision Measurements . . . . .	23
1.2.4 Beyond the Standard Model and Supersymmetry . . . . .	25
<b>2 The Compact Muon Solenoid</b>	<b>27</b>
2.1 Overall Design and Physical Requirements . . . . .	27
2.2 The Tracking System . . . . .	31
2.2.1 The Pixel Detectors . . . . .	32
2.2.2 The Silicon Microstrip Detectors . . . . .	33
2.3 The Electromagnetic Calorimeter . . . . .	34
2.4 The Hadron Calorimeter . . . . .	36
2.5 The Magnet . . . . .	37
2.6 The Muon System . . . . .	38
2.6.1 The Drift Tube Chambers . . . . .	39
2.6.2 The Cathode Strip Chambers . . . . .	41
2.6.3 The Resistive Plates Chambers . . . . .	43
2.7 Trigger and Data Acquisition . . . . .	44
2.7.1 The Level-1 Trigger System . . . . .	46
2.7.2 The High Level Trigger and DAQ . . . . .	51

## CONTENTS

---

<b>3</b>	<b>The Drift Tubes System and Trigger Electronics</b>	<b>55</b>
3.1	The Drift Tubes System . . . . .	55
3.1.1	The Drift Chamber . . . . .	56
3.1.2	The Drift Cell . . . . .	57
3.2	DT Local Trigger . . . . .	65
3.2.1	The Bunch and Track Identifier . . . . .	66
3.2.2	The Track Correlator . . . . .	69
3.2.3	The Trigger Server . . . . .	74
3.2.4	The Sector Collector . . . . .	77
3.3	DT Regional Trigger . . . . .	78
3.3.1	The Phi Track Finder . . . . .	79
3.3.2	The Eta Track Finder . . . . .	81
3.3.3	The Muon Sorter . . . . .	81
<b>4</b>	<b>DT Local Trigger Emulation and Monitoring</b>	<b>85</b>
4.1	DT Local Trigger Emulation . . . . .	85
4.2	Data Quality Monitoring in CMS . . . . .	92
4.2.1	DT and DT Local Trigger Online Monitoring . . . . .	95
<b>5</b>	<b>DT Local Trigger Commissioning with Cosmic Rays</b>	<b>103</b>
5.1	CMS Commissioning with Cosmic Rays . . . . .	103
5.1.1	DT Subsystem Commissioning with Cosmic Rays . . . . .	106
5.2	DT Trigger Configuration during Commissioning . . . . .	109
5.2.1	Data Selection for Performance Studies . . . . .	111
5.3	DT Local Trigger Performances . . . . .	112
5.3.1	BX Identification and Primitives Quality . . . . .	113
5.3.2	Comparison with Local Reconstruction . . . . .	124
5.3.3	Effects of the Magnetic Field . . . . .	133
5.4	Synchronization Studies . . . . .	136
5.5	Comparison with the Emulator . . . . .	141
	<b>Conclusions</b>	<b>149</b>
	<b>Bibliography</b>	<b>151</b>

# Introduction

The Standard Model is a highly successful theory, being able to describe a wide range of phenomena with high accuracy. A remarkable degree of consistency exists between precise measurements of electroweak observables and theoretical predictions. Anyhow the problem of the origin of the masses of the particles within the model has still to be solved. The Higgs mechanism addresses the issue and seems to be a good candidate to solve this enigma. However, among other things, it predicts the existence of a scalar particle, the Higgs boson, which has not yet been experimentally observed. Moreover there are already indications that the Standard Model is only an approximation of a more fundamental theory that could manifest itself at energies higher than the ones reached by the accelerators of the present generation.

To shed light to these questions the Large Hadron Collider (LHC), a collider able to provide  $p$ - $p$  interactions at a center of mass energy up to 14 TeV, has been built at CERN, in the 27 km underground tunnel that previously hosted the LEP accelerator. This machine is presently being commissioned and it is expected to produce first collisions by the end of 2009.

The LHC is designed to operate at a bunch crossing frequency of 40 MHz and reach a luminosity of  $10^{34} \text{cm}^{-2} \text{s}^{-1}$ . This will lead to a total event rate of about  $6 \cdot 10^8 \text{ events/s}$ . The expected cross sections for many interesting physics processes are actually many orders of magnitude smaller than the total inelastic cross section; experiments have therefore to operate very efficient selections to isolate these kind of interactions.

The Compact Muon Solenoid (CMS) is one of the two general purpose detectors that will operate at LHC. To cope with the extremely high collision rate, a very efficient and complex trigger system was developed for this experiment. This system has to perform event rate reduction of a factor of about  $10^6$  as up to 100 events per second can be delivered to storage system, to be available for offline analyses. Trigger operations will be performed at two

different processing levels. Initially a Level-1 Trigger system, implemented using custom electronics, operates a first reduction of a factor of about  $10^4$  on the basis of information coming from calorimeters and muon spectrometer. Then a High Level Trigger, implemented using software programs running on a farm of commercial processors, performs further reduction up the 100 Hz rate expected by the storage system.

In order to have a fully operative detector in time for first LHC collisions, a long commissioning phase of the CMS experiment using cosmic rays started already before the first detector component was lowered in the underground cavern. Many globally coordinated runs have been performed, including an entire month of data taking exercise where the full detector has been operated as a whole. During this phase the data acquisition sequence has been driven by the Level-1 muon trigger. The trigger subsystem equipping the drift tubes barrel detector (DTs) has taken part to this process since the beginning of the tests, being a fundamental element during every commissioning phase.

The work for this thesis concerns the study of the performances of the DT local trigger system during commissioning. Analyses on the behaviour of the various components of the system were carried out. These include studies on the precision and accuracy of the trigger reconstruction mechanism and measurement of the trigger efficiency. The description of a method to perform system synchronization is also reported. The software code used to emulate trigger reconstruction mechanism in simulations was adapted, as part of the work for this thesis, to correctly operate on data coming from the real detector. Therefore a comparison between hardware and emulator results is also shown. Furthermore some of the algorithms used for this study were migrated to the CMS Data Quality Monitoring system. These have been used to monitor the trigger performances during data acquisition and to operate prompt offline analysis devoted to the validation of the detector response.

In Chapter 1 a introduction to the LHC project and its physics program is given. The CMS detector and its overall trigger and data acquisition system are described in Chapter 2. In Chapter 3 a more in depth report of the DT system and its related trigger electronics is presented. Chapter 4 includes the description of the DT trigger online monitoring system and software emulation code. Finally, in Chapter 5, the results of a detailed analysis of the system performances are reported.

# Chapter 1

## The LHC Project

The Large Hadron Collider (LHC) is the accelerating machine built at CERN and is designed to collide *proton beams* with a center-of-mass energy up to 14 TeV at luminosity of  $10^{34} \text{ cm}^{-2} \text{ s}^{-1}$ . It is also capable to accelerate *lead ions* up to a center-of-mass energy of 2.76 TeV per nucleon pair. The LHC is burden to study a wide range of possible physical phenomena which are suppose to happen at the TeV energy scale (such as the Higgs mechanism) and to check the overall Standard Model (SM) consistency; it is also called to investigate a wide range of possible scenarios *beyond the SM*, as well as look for the way toward unification of fundamental forces of nature. The LHC was operated for the first time in September 2008, but a technical incident forced a stop, which is presently undergoing, in order to repair the damaged parts and understand what caused the fault.

### 1.1 The Large Hadron Collider

The LHC machine [1, 2, 3] has been installed in the 27 km tunnel previously used for LEP (Large Electron Positron) collider. It profits of the existing CERN accelerator chain (Fig. 1.1) in order to obtain an injection energy of 450 GeV. The availability of existing infrastructures led to technical advantages as well as economical savings, the only drawback coming from this solution is the fact that the use of the LEP tunnel implies a fixed curvature for the collider, thus setting stringent constraint on its design concept.

High field superconducting magnetic dipoles, able to reach a stable 8.3 T field, are needed in order to bend the beam trajectory in the existing tunnel

## THE LHC PROJECT

---

and acceleration up to design energy can be achieved using superconducting radio-frequency cavities. The whole system has to be kept at a temperature of 2.1 K using superfluid helium, in order to maintain the superconducting regime. The LHC is developed to collide bunches of  $1.1 \cdot 10^{11}$  protons each, with a beam spot size of  $\sigma_z \simeq 53 \text{ mm}$  and  $\sigma_{xy} \simeq 15 \mu\text{m}$ , at a design bunch crossing ( $BX$ ) frequency of  $40 \text{ MHz}$ .

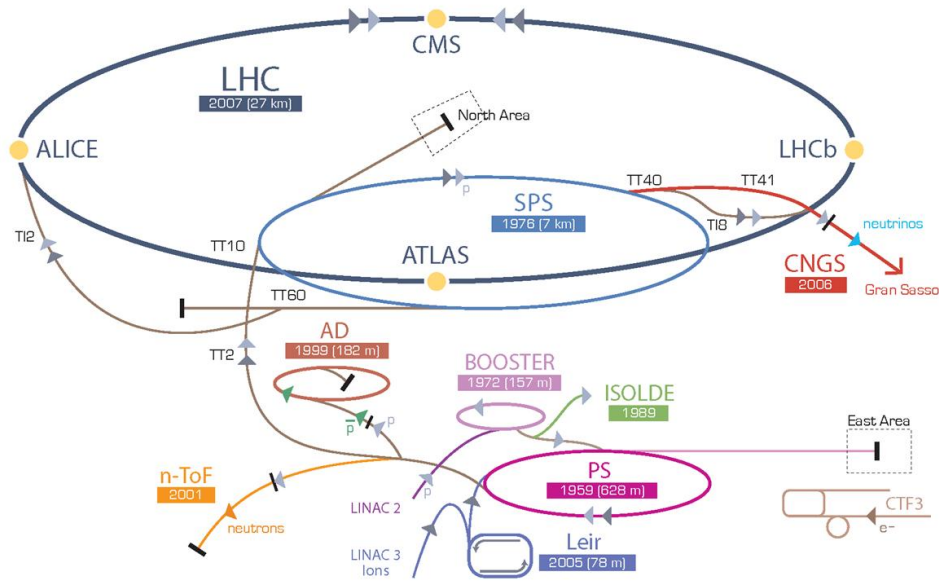


Figure 1.1: *The CERN accelerator complex. The LHC injection chain starts with proton production by hydrogen ionization (750 keV); LINAC2 acceleration up to 50 MeV follows; in the BOOSTER rearrangement in  $10^{11}$  proton packets of 1.1 GeV occurs; PS further increase energy up to 25 GeV and finally SPS brings the beam energy up to 450 GeV.*

The design choice to collide proton-proton beams has several advantages which can be explained by the following considerations:

- The usage of hadrons allows to explore phenomena in a wide range of energies using fixed-energy beams. This comes from the fact that protons are not elementary particles, hence, in hard collisions, the interaction involves the particle constituents, which do not carry a fixed

fraction of the hadron energy. The choice of protons beams thus comes natural if a *discovery machine* is intended to be built.

- Despite their difference in the low energy regime,  $p$ - $p$  and  $p$ - $\bar{p}$  total cross sections are very close at high energies (as shown in Fig. 1.3). Moreover proton production is faster and more efficient with respect to antiproton one, thus allowing to reach higher luminosity and keep beam stability. The only drawback of this solution is due to the fact that two separate beam pipes are needed in order to manage bunches of protons circulating in opposite directions.
- In case of circular motion of charged particles the energy loss due to synchrotron radiation is proportional to the inverse of the fourth power of the particle mass. Hence by using bunches of protons, whose mass is almost 2000 times higher than the one of electrons, is possible to re-use the existing LEP tunnel in order to build a collider able to reach higher energy with respect to its predecessor.

The key parameters that characterize the overall machine performance are the high design *luminosity* ( $\mathcal{L}$ ) and the unprecedented *center-of-mass energy* ( $\sqrt{s}$ ). The former is strictly related to the *interaction rate* and, together with the development of a high rejection and efficient trigger system of the experiments, will allow to investigate many interesting physical phenomena with low cross section (as explained in section 1.2).

$\mathcal{L}$  can be computed using the:

$$\mathcal{L} = \frac{\gamma f k_B N_P^2}{4\pi \epsilon_n \beta^*} F \quad (1.1)$$

where  $\gamma$  is the Lorentz factor,  $f$  is the revolution frequency,  $k_B$  is the number of bunches,  $N_P$  is the number of protons per bunch,  $\epsilon_n$  is the normalized transverse emittance (which design value is  $3.75 \mu m$ ),  $\beta^*$  is the betatron function at the interaction point and  $F$  is a reduction factor due to the crossing angle. This leads, for the LHC, to a design luminosity of  $10^{34} \text{ cm}^{-2} \text{ s}^{-1}$ , a hundred times higher than the one previously reached at the Tevatron at Fermilab.

The total interaction rate is thus given by:

$$R = \sigma \cdot \mathcal{L} \quad (1.2)$$

which, for a predicted total cross section of  $80 \text{ mb}$ , gives an expected event rate around  $0.7 \cdot 10^9 \text{ events/s}$ .

The limit on the center-of-mass energy is imposed by the LHC radius ( $\sim 4.3 \text{ km}$ ) and by the maximum reliable field achievable using the superconducting bending dipoles. It can be computed using the:

$$p(\text{TeV}) = \frac{q}{e} \cdot 0,3 \cdot B(\text{Tesla}) \cdot R(\text{km}) \quad (1.3)$$

this leads to a value of 14 TeV, roughly seven times the one reached by the Tevatron. It is important to point out that the above computation is performed using only an average magnetic field of  $5.4 \text{ T}$ . This is due to the fact that beam bending is not applied everywhere along the LHC tunnel, thus a reduction factor has to be introduced. Some of the relevant LHC parameters, are summarized in tables 1.1 and 1.2.

Parameter		$p$ - $p$	$Pb$ - $Pb$	M.U.
Energy per nucleon	$TeV$	E	7	2.76
Design Luminosity	$cm^{-2}s^{-1}$	$\mathcal{L}$	$10^{34}$	$10^{27}$
Bunch Separation	$ns$		25	100
Numb. of bunches		$N_B$	2808	592
Particles per bunch		$N_p$	$1.15 \cdot 10^{11}$	$7.0 \cdot 10^7$
$\beta$ value at IP	$m$	$\beta^*$	0.55	0.5
RMS of beam radius at IP	$\mu m$	$\sigma^*$	16.7	15.9
Luminosity lifetime	$h$	$\tau_X$	15	6
Number of collision/crossing	$n_c$	20	-	
Bunch length ( $\sigma_z$ )	$mm$		53	
Beam current	$mA$		560	

Table 1.1: *Beam parameters of the LHC.*

Four experiments will be installed in as many interaction points along the collider ring (Fig. 1.2): ATLAS (**A** **T**oroidal **L**H**C** **A**pparatus) and CMS (**C**ompact **M**uon **S**olenoid) are general purpose detectors devoted to the study of many SM and beyond the SM phenomena, ALICE (**A** **L**arge **I**on **C**ollider **E**xperiment) will mainly probe the heavy ions physics focusing on the study of the *quark-gluon plasma* and LHCb (**L**H**C** **b**eauty experiment) will be called to investigate the CP violation mechanism in b-physics.

Parameter	Value
Radius	$\sim 4.3 \text{ km}$
Dipole field	8.3 T
Number of dipoles	1232
Number of quadrupoles	520
Number of sextupoles	2x1232
Number of octupoles	1232

Table 1.2: *Machine parameters of the LHC.*

Original plans for the LHC schedule foresaw that an initial commissioning phase, characterized by a low luminosity (around  $10^{32} \text{ cm}^{-2}\text{s}^{-1}$ ) and 75 ns bunch spacing, was supposed to start in late 2008. Then three years of data-taking at a peak luminosity of  $2 \cdot 10^{33} \text{ cm}^{-2}\text{s}^{-1}$  (the so called “*low luminosity*” scenario) were expected before reaching the design “*high luminosity*” value of  $10^{34} \text{ cm}^{-2}\text{s}^{-1}$ . However, after the incident occurred on the 19th of September 2008, the LHC schedule has been further postponed. First collisions are expected for the late 2009, afterwards a first period of data taking at lower center-of-mass energy (10 TeV or even less) with a low, still not established, luminosity will follow.

## 1.2 Physics at the LHC

The Standard Model of particle physics [4] is among the most successful achievements of modern science. It describes three of the four fundamental forces of nature with high accuracy, in fact it is able to explain a wide range of experimental facts passing precise test at the 0.1% to 1% level.

Within the model, nature is described using half-integer (fermionic) and integer (bosonic) fields whose quantization implies the existence of point-like fundamental particles. Fermions are further split in two different families (quark and leptons) and both of them are replicated into three *generations*, characterized by different mass parameters. Interaction between particles arises asking the invariance of the field lagrangian under  $SU(3)_C \otimes SU(2)_L \otimes U(1)_Y$  gauge transformations, where  $SU(3)_C$  is responsible to of the strong (*colour*) interaction while  $SU(2)_L \otimes U(1)_Y$  describes the electroweak sec-

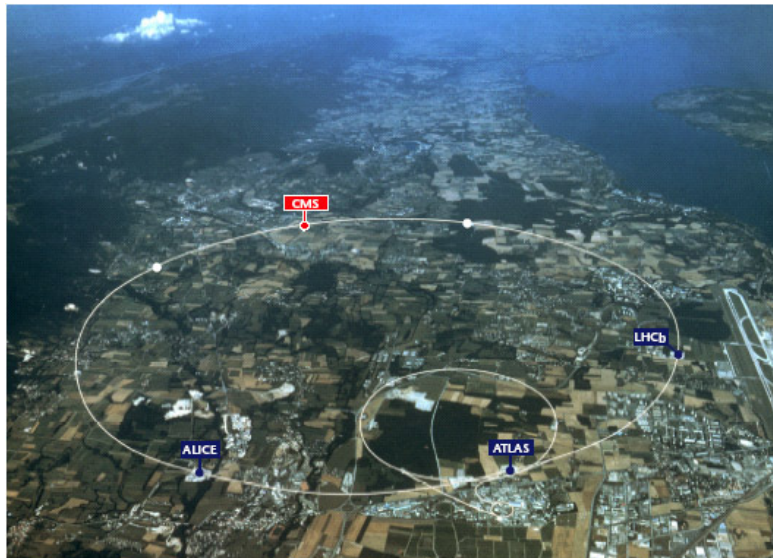


Figure 1.2: *View of the location of the LHC and LHC related experiment in the Geneva region.*

tor of the SM on the basis of *left-handed* lepton doublets and *hypercharge* singlets. Mixing between quark generation is explained using the CKM (*Cabibbo-Kobayashi-Maskawa*) mechanism and further separation between weak and electromagnetic interactions is obtained introducing a spontaneous-symmetry-breaking mechanism, known as Higgs mechanism, which is also responsible of the generation of the masses of the weak interacting vector bosons.

The adoption of spontaneous-symmetry-breaking allows to preserve the gauge invariance of the theory that would be manifestly violated in the case of the insertion of ad-hoc mass terms in the field lagrangians. Moreover as a consequence of the Higgs mechanism the existence of a scalar bosonic particle, the Higgs boson, is also predicted.

Despite the formal elegance of the model, the Higgs boson has not yet been experimentally discovered, but both, experimental and theoretical arguments [1.2.2], suggest that its existence could very likely be proved by an experiment able to probe the TeV scale. Moreover a wide range SM direct and indirect measurements could be made at that energy scale in order to

check the consistency of the model itself, and look for deviations as signal of new physics.

Finally the SM is supposed to be only a low-energy effective model of nature, since it leaves too many unanswered questions to be considered as a fundamental theory. First of all it does not explain why fermions are replicated in three copies and why their mass pattern is so bizarre. In addition it does not give a proper description of neutrino masses and of their oscillation mechanism. Furthermore the CP violation mechanism of the SM is unable to explain the matter-antimatter asymmetry of the Universe. Additionally the SM does not take into account gravitational interactions and is not suitable for the unification of strong and electroweak couplings at high energies. Finally the hierarchy problem, that arises taking into account Higgs boson mass renormalization, suggests the existence of some hidden mechanism responsible for the fine cancellation of quadratic divergences needed to keep the Higgs mass parameter small at high energy scales.

Many theoretical frameworks have been developed to overcome these problems (*supersymmetry* and *extra-dimensions*, to name a few), thus besides the main topic related to the search of the Higgs, the LHC physics programme [5, 6] foresees a wide spectrum of analysis related to physics phenomena beyond the standard model.

### 1.2.1 Cross Sections and Rates

As described in 1.1 the high LHC design luminosity, together with the total inelastic cross section at  $\sqrt{s} = 14 \text{ TeV}$ , lead to an impressive event rate of about  $0.7 \cdot 10^9 \text{ events/s}$ . This means that, for a 40 MHz bunch crossing frequency, an average value of  $\sim 17$  interaction per BX is foreseen.

This number is just an average computation obtained considering that every 25 ns a bunch crossing will occur. Actually not all the LHC bunches will be full, thus a correction factor has to be applied raising the aforementioned number to a value of  $\sim 22$  interaction per “*effective*” BX in the high luminosity scenario (4 events per “*effective*” BX are expected at low luminosity). Therefore, at LHC nominal conditions, every interesting physical process will be overlapped with an average value of more than 20 other interactions, whose take the name of *pile-up* events.

Moreover the range of cross sections related to most of the physical interesting phenomena is many order of magnitude smaller than the total inelastic

## THE LHC PROJECT

cross section, as depicted in Fig. 1.3. An analysis of the various typology of events produced at the LHC is thus needed in order to define an effective trigger strategy for data acquisition.

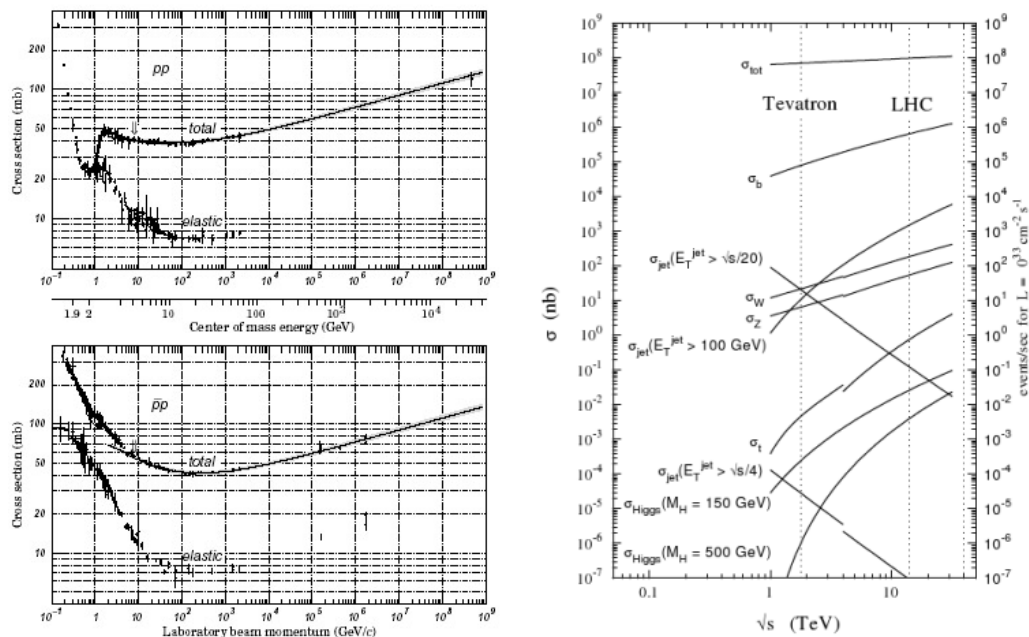


Figure 1.3: Total and elastic cross sections for  $p - p$  and  $p - \bar{p}$  collision as a function of the laboratory beam momentum (left). Production cross sections for many of the LHC processes as a function of the center-of-mass energy (right).

Most of the collisions produced at the LHC will be due to “soft interactions”, where the transverse momentum ( $p_T$ ) exchanged between particles is small and almost all the collision energy escapes down the beam pipe. These events are called “minimum bias” and will be the largest fraction of LHC collisions but, due to the small transverse energy transfer, their physical content will not allow many of the aforementioned studies. On the other hand most interactions of physical interest will involve “hard scattering” head-on collision, where the transferred energy will be enough to create massive and/or high  $p_T$  particles.

Generally in hadron colliders these kind of events are dominated by QCD

jet production due to the fragmentation of the incoming partons. This is especially true in the case of high center-of-mass energy accelerators since the cross section of jet production increases with  $\sqrt{s}$  much faster than the one of the typical electroweak processes. In any case, although the lower branching-ratio ( $br$ ), final states including leptons and photons are preferred for physical analysis due to the simpler signature and low background. Hence high  $p_T$  leptons and photons are widely used for triggering purposes in LHC experiments.

### 1.2.2 Higgs Search

The most prominent question the LHC is called to answer is the one concerning the origin of masses in the electroweak sector of the SM [8, 9]. Theoretical and experimental bounds suggest that, if a Standard Model Higgs ( $H_{SM}$ ) exists, it has to be found in a mass range roughly spanning from 100 to  $\sim 1000$   $GeV/c^2$ .

The Feynman diagrams displaying the processes that mainly contribute to the  $H_{SM}$  production at LHC are shown in Fig. 1.4. Fig. 1.5 shows the cross sections of the different processes as a function of the  $H_{SM}$  mass as well as the  $H_{SM}$  decay branching ratios.

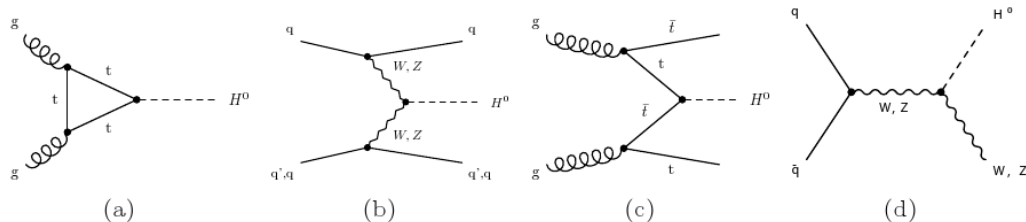


Figure 1.4: *Feynman diagrams of the principal Standard Model Higgs boson production mechanism at LHC: a) gluon-gluon fusion; b) W,Z fusion; c) top-antitop associated production; W,Z associated production.*

At LHC the SM Higgs production will mainly occur through gluon-gluon fusion and only at very high Higgs masses the vector boson fusion process becomes comparable. However, despite the smallest cross section, the WW scattering is a very promising channel since the presence of two spectator jets

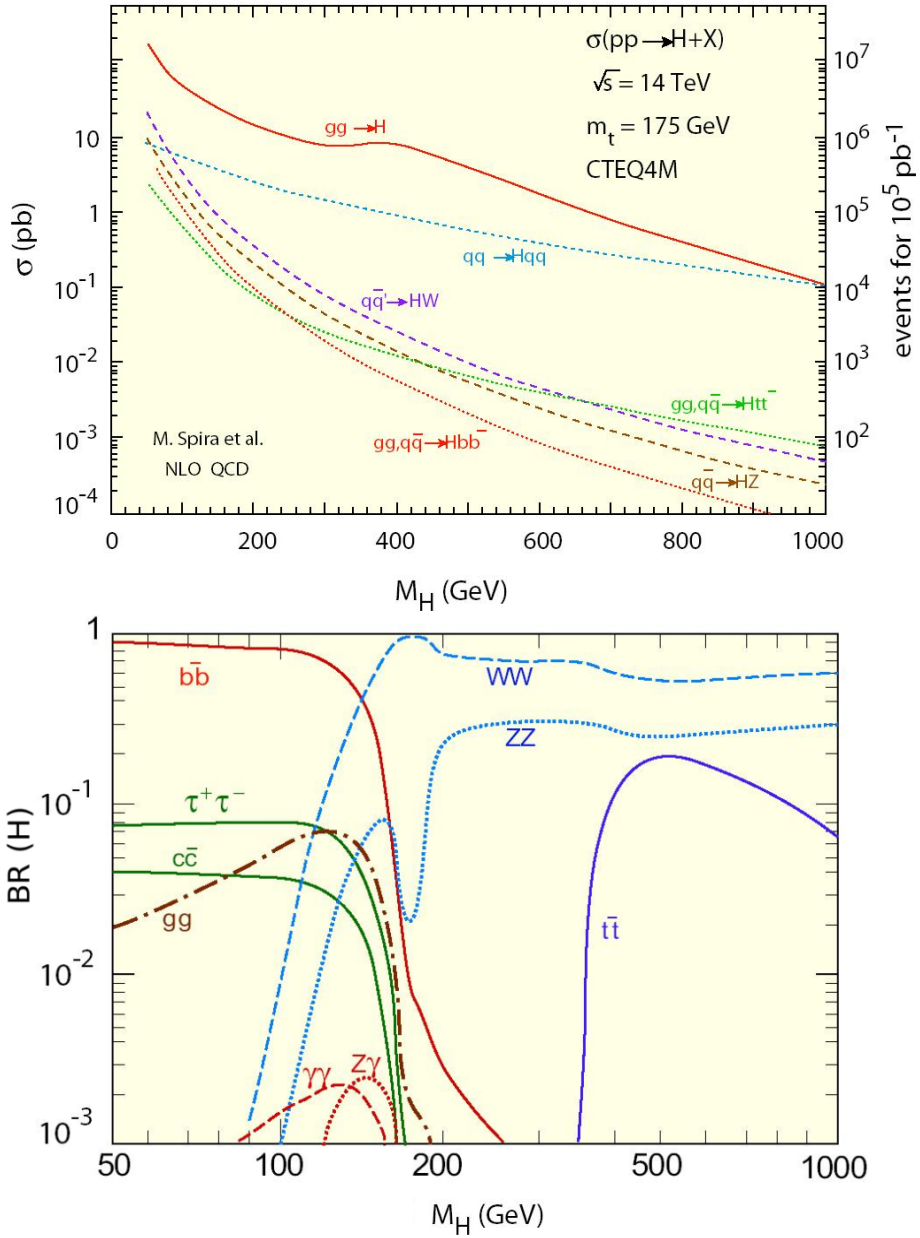


Figure 1.5: Standard Model Higgs production cross sections (top) and decay branching ratios (bottom) as a function of the Higgs mass.

provides a very clear signature which allows to discriminate the signal from the background. Other production channels, such as the W and Z associated production, or the  $gg, q\bar{q} \rightarrow t\bar{t}H$  have cross section are a couple of orders of magnitude smaller than the gluon-gluon fusion. Anyway, even in these channels, additional bosons or jets assure a clear signature to be used for tagging.

The total cross section is of the order of  $pb$ , thus leading to a total production rate of  $10^{-2} Hz$  at the LHC designed luminosity. However a further reduction to the rate accessible for data analysis, due to decay branching ratios and to the fact that not all possible final states will be observable, has to be applied.

The branching ratios shown in Fig. 1.5 (bottom) can be interpreted on the basis of the  $H_{SM}$  coupling to fermions and gauge bosons:

$$g_{Hff} \propto m_f \tag{1.4}$$

$$g_{HWW} \propto 2m_W^2 \tag{1.5}$$

$$g_{HZZ} \propto m_Z^2 \tag{1.6}$$

In fact, as can be seen from the formulas, the first is proportional to the fermion mass whereas the second and the third grow linearly with the square of the boson masses, therefore the dominant contribution due to ZZ and WW decay at high Higgs mass is foreseen.  $t\bar{t}$  final state becomes accessible if  $m_H > 2m_t$ , though it never has a dominant contribution due to the high vector boson branching ratio in that mass range. As a function of the Higgs mass is thus possible to identify three main regions where different analysis strategies can be carried out:

**low mass region** ( $m_H < 130 GeV/c^2$ ): the  $H \rightarrow b\bar{b}$  dominates in this mass region but, due to the high QCD background, this channel is not easily observable (some advantages could however be taken using  $t\bar{t}H$  or  $WH$  production). In any case, despite the low branching ratio,  $H \rightarrow \gamma\gamma$  decay can be used in these region because of its extremely clear signature and sharp reconstructed mass peak.

**intermediate mass region** ( $130 GeV/c^2 < m_H \leq 500 GeV/c^2$ ): the WW and ZZ becomes accessible and has a very high branching ratio.  $H \rightarrow 4l$  is the most promising (“golden-plated”) channel for Higgs search in this region: this is obviously due to its clear leptonic signature which

allows precise reconstruction of the Higgs mass. It however suffers from the low leptonic branching ratio of the Z boson and the small  $H_{SM}$  production cross section at high  $m_H$  values. The  $H \rightarrow WW$  is also a valuable discovery channel around  $m_H = 170 \text{ GeV}/c^2$  due to its high branching ratio in this region. In any case the presence of undetected neutrino(es) in the final state does not allow precise mass measurements.

**high mass region ( $m_H > 500 \text{ GeV}/c^2$ ):** in this region the production cross section becomes small, therefore semi-leptonic final states have to be included in data analysis. Moreover the Higgs resonance width becomes broad (Fig. 1.6), and the experimental measurement of  $m_H$  is no longer precise.

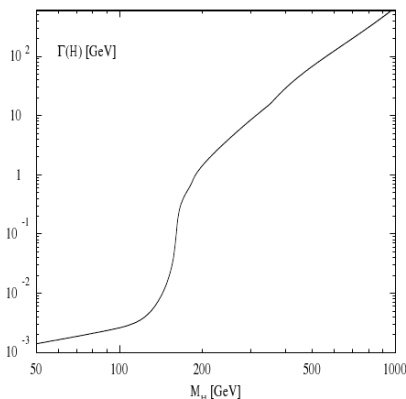


Figure 1.6: *Standard Model Higgs width as a function of the particle mass.*

### Higgs Mass Bounds and Limits

The theoretical requirement of asking the SM model to be a valid (consistent) physical approximation of the real world up to a certain energy scale  $\Lambda$  imposes constraints to the possible range of values that  $m_H$  can assume in the model. A lower limit on the Higgs mass [10] can in fact be imposed requiring vacuum stability of the Higgs potential  $V(\phi^\dagger\phi)$  under renormalization. This comes from the fact that quantum loop corrections to  $V(\phi^\dagger\phi)$  may

cause the potential derivative to become negative at high values of  $\phi$ , thus making it unbounded from below. The  $V(\phi^\dagger\phi)$  stability for  $\phi \sim \Lambda \gg m_z$  is ensured requiring that the Higgs self coupling never becomes negative up to the energy scale where the model is supposed to be consistent.

Moreover the requirement that no Landau poles appear up to the breakdown scale [11] ensures the presence of an upper bound to the  $H_{SM}$  mass (*triviality*). Considering in fact the simplified renormalization group equation for the Higgs quartic potential term  $\lambda$ , obtained neglecting gauge and Yukawa couplings:

$$\Lambda < m_H \exp\left(\frac{4\pi^2 v^2}{3m_H^2}\right) \quad (1.7)$$

is possible to evince that for a given Higgs mass the theory only makes sense up to a finite energy scale  $\Lambda$

Fig. 1.7 shows the theoretical bounds on Higgs mass as a function of the energy scale. In order to ensure that the SM remains valid up to the Planck Scale ( $10^{19} \text{ GeV}$ ) a constraint on the Higgs mass in the  $130\text{-}190 \text{ GeV}/c^2$  is needed. Assuming the SM validity up to the TeV scale only, an upper bound of  $600\text{-}800 \text{ GeV}/c^2$  arises. This explains why the LHC is a good candidate to find the Higgs in a SM scenario if it exists.

Furthermore experimental limits on the Higgs mass come from measurements performed at LEP, SLC and Tevatron. Direct searches excluded the existence of a Higgs boson with a mass up to  $114.4 \text{ GeV}$  at 95% confidence limit [12]. In addition, as electroweak quantities as top and W masses and Z decay parameters are logarithmically sensitive to  $m_H$  through radiative correction, it is possible to perform indirect  $m_H$  determination using precise electroweak measurements [13].

Fitting these data and performing a  $\chi^2$  analysis taking the Higgs mass as a free parameter it is possible to impose an upper limit to its value to be around  $150 \text{ GeV}/c^2$  at 95% confidence level. This estimation is obtained computing  $\Delta\chi^2 = \chi^2 - \chi_{min}^2$  as a function of  $m_H$  (Fig. 1.8). The solid curve represents the result of the fit itself while the shaded band takes into account the uncertainty due to high order correction that have not been calculated yet.

Direct W and Top mass measurements can also be compared with indirect estimations coming from electroweak loop corrections. Figure 1.8 (right) shows results coming from these measurements, as well as the SM prediction

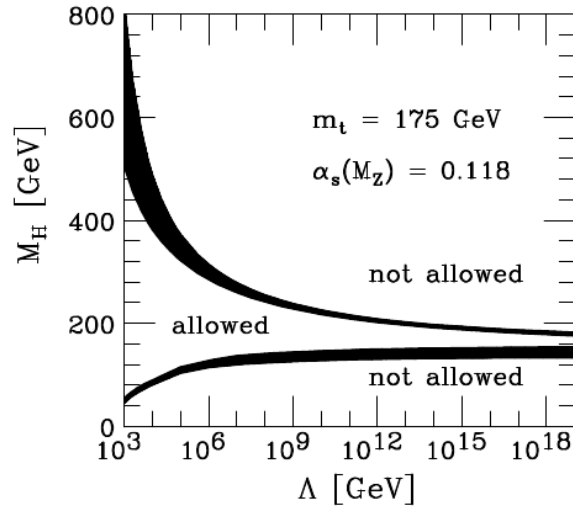


Figure 1.7: *Theoretical bounds on the Standard Model Higgs mass as a function of the energy-scale ( $\Lambda$ ) up to where the model is valid.*

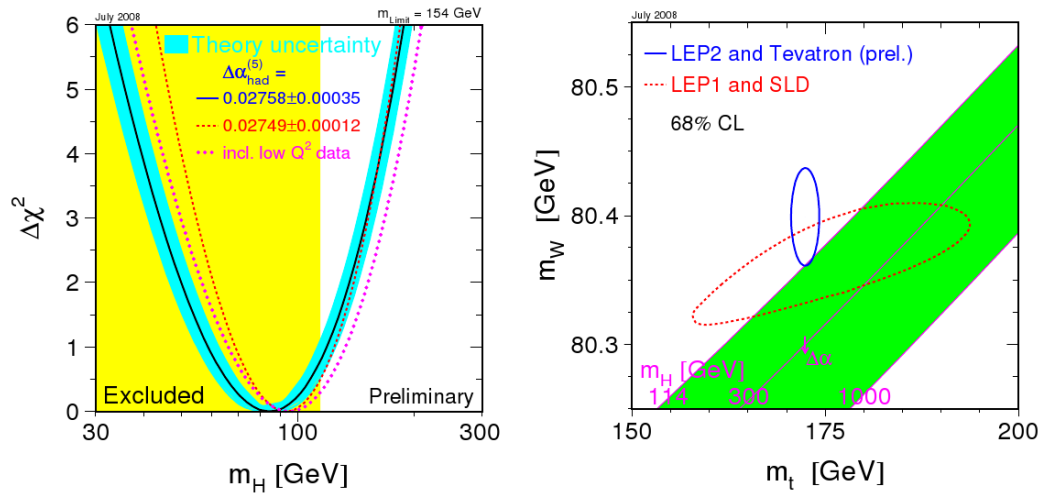


Figure 1.8: *Experimental limits on  $m_H$  coming from the  $\chi^2$  Electroweak fit (left) and  $W$ - $t$  precise mass measurements (right).*

of these parameters for a Higgs in a 114-1000  $GeV/c^2$  mass range. As can be seen indirect and direct measurements are in good agreement.

### 1.2.3 Standard Model Physics and Precision Measurements

The LHC will allow to improve the precision of many SM measurements due to the high statistics of interesting phenomena it will be able to collect. The high production rate of many SM phenomena ensures, in fact, that most measurements will have small statistical uncertainty. Furthermore it allows also to perform accurate studies on the detector response, resulting in a precise understanding of systematic uncertainties. A complete discussion of the various SM measurements achievable with the LHC is beyond the purpose of this section, instead a brief overview of W and Top related measurements, due to their relationship to aforementioned topics, follows (for a more exhaustive discussion look at [15, 16]):

#### Measurement of the W Mass

The W mass is a fundamental parameter of the SM and constitutes an important check of its consistency. Moreover its sensitivity to the  $H_{SM}$ , as well as to supersymmetric corrections, can give clues for the LHC discovery program. However, in order to put some constraints, the W mass parameter has to be known with high accuracy and precision.

At hadron colliders such a measurement is performed using the leptonic  $W \rightarrow e\nu$  and  $W \rightarrow \mu\nu$  channels, being the  $W \rightarrow \tau\nu$  poorly constrained due to the presence of other neutrino(es) in the  $\tau$  decay.

The invariant mass of the  $l\nu$  system cannot be directly reconstructed due to the fact that the longitudinal component of the neutrino momentum is unknown in  $p$ - $p$  colliders. Therefore the W mass is traditionally obtained by fitting the distribution of its transverse component taking advantage of Monte Carlo simulations.

This measurement is accomplished using the  $m_T^W = \sqrt{p_T^l p_T^\nu (1 - \cos\Delta\phi)}$  formula where  $p_T^l$  represent the transverse mass of the lepton,  $p_T^\nu$  is the transverse mass of the neutrino and  $\Delta\phi$  is the separation angle between the two particles in the transverse plane. The most relevant contributions to systematics in this method come from the lepton energy scale/resolution and

from physics uncertainties due to the parton density functions and limited knowledge of the  $W$   $p_T$  spectrum.

Consequently alternatives to this method have been considered ([17]). The most promising one is based on the prediction of experimental parameters sensitive to the  $W$  mass, such as the  $p_T^l$  or the  $m_T$  distributions, on the basis of the corresponding ones measured in  $Z \rightarrow \bar{l}l$  decays. The distribution of transverse mass in  $Z$  boson events is obtained considering one of the outgoing leptons as characterized by missing energy in the same way the  $\nu$  coming from  $W$  decay is. The theoretical distributions of  $m_T$  for  $Z$  and  $W$  are, if fact, very similar in a wide range of kinematics.

The advantage of this method is that most of the experimental and theoretical uncertainties are common to  $Z$  and  $W$ , thus they cancel in the comparison, reducing the effect due to systematics. The main drawback is due to the reduced  $Z \rightarrow \bar{l}l$  rate. In any case an overall precision of order of  $10 \text{ MeV}/c^2$  ( $30 \text{ MeV}/c^2$ ) for an integrated luminosity of  $10 \text{ fb}^{-1}$  ( $1 \text{ fb}^{-1}$ ) is expected.

### Precision Physics in the Top Sector

Top ( $t$ ) quark measurements performed at the Tevatron, are mostly limited by statistics. At the LHC  $t$  measurements will benefit from very large statistics due to the high  $t\bar{t}$  production cross section at  $\sqrt{s} = 14 \text{ TeV}$ . The high number of produced  $t$  quarks will thus allow to improve the precision of the measurements and to perform studies on the  $t$  special role in radiative corrections. Moreover  $t$  studies will be useful for detector commissioning and to understand backgrounds related to Higgs and new physics searches.

At low luminosity a production of around  $8 \cdot 10^6 \text{ } t\bar{t}/\text{year}$  is foreseen at LHC. The dominant production mechanism is gluon-gluon fusion (90%) but  $q\bar{q}$  annihilation (10%) will also play an important role.

Within the SM the  $t$  decay will occur mainly through the  $t\bar{t} \rightarrow WWb\bar{b}$  process and the most promising channel to perform mass measurements is the one that takes advantage from one leptonic ( $W \rightarrow l\nu$ ) and one hadronic ( $W \rightarrow \text{jet jet}$ ) decay of the  $W$  boson (semileptonic-decay). In this case the leptonic part can be used to select the event and the hadronic one is used to perform mass reconstruction.

As already said, statistical uncertainties are expected to be small, therefore the main source of uncertainties will come from the knowledge of the jet

energy scale, from the  $b$ -fragmentation mechanism and from the response of the detector to radiated gluons.

Measures of the  $t$  mass based on the use of fully-hadronic and fully-leptonic decays have also been investigated [15]. Moreover the fully-hadronic channel will provide a method to calibrate hadronic calorimeters.

A combined precision on the  $t$  mass measurement (obtained merging information from different channels) of less than  $1 \text{ GeV}/c^2$  is expected at the LHC. Together with the improvements expected in the  $W$  sector, this measurement will allow to further tighten the bounds on the logarithm of  $m_H$  by a factor 2 with respect to the current value. Thus providing a very stringent constraint on the SM in the case  $H_{SM}$  is not found in the expected mass range.

### 1.2.4 Beyond the Standard Model and Supersymmetry

As explained before, there are several reasons to think that the Standard Model is only a low-energy approximation of a more fundamental theory. In order to solve at least some of the already discussed problems many theoretical models have been elaborated. Among others, Supersymmetry [18] (SUSY) is widely considered a possible extension of the Standard model. SUSY introduces a new fundamental symmetry between bosonic and fermionic fields, predicting the existence of new ( $s$ -)particles with a spin number that differs by one half with respect to the one of their known partners. This allows to solve the hierarchy problem because the quadratic divergent terms related to Higgs mass renormalization cancel as a consequence of the boson-fermion symmetry. Moreover supersymmetric corrections to the running of the strong and electroweak couplings allow gauge-coupling unification at high energy.

The simplest supersymmetric extension of the Standard Model is the Minimal Supersymmetric Standard Model (MSSM). Apart from previously discussed advantages, the MSSM predicts the existence of a weakly interacting Lightest Stable Particle (LSP), the neutralino, which might be a good candidate for Dark Matter.

The mass generation mechanism of the MSSM foresees the existence of two Higgs doublets corresponding to three neutral ( $h, H, A$ ) and two charged ( $H^\pm$ ) particles. At the tree level all masses and couplings depend on two parameters, usually chosen as the mass of the  $A$  boson and the ratio of the

vacuum expectation of the two Higgs doublets.

Neutral MSSM Higgs bosons mainly decay to  $b\bar{b}$  and  $\tau^+\tau^-$ , being the vector bosons decay mode suppressed. Instead, the predominant decay mode for charge Higgs boson will produce  $\tau\nu$  pairs. However the large background coming from  $b$ -jets will not allow analysis performed on  $b\bar{b}$  decays, therefore many MSSM Higgs studies will rely on  $\tau$  decay identification. Anyhow all these particles have been also shown to decay into leptonic final states and, despite the smaller cross section, channels as  $gg \rightarrow Hb\bar{b} \rightarrow \mu^+\mu^-b\bar{b}$  can also be used as they provide good Higgs mass reconstruction.

As shown in Fig. 1.9, previously discussed precise W and t mass measurements seem to favour MSSM mass generation mechanism with respect to SM one [19, 20].

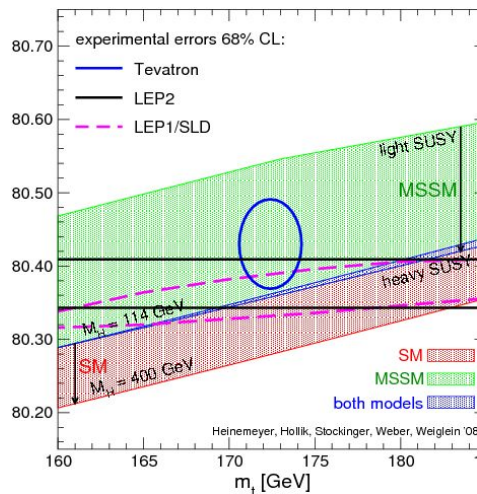


Figure 1.9: *Experimental limits on  $m_H$  coming from W-t precise mass measurements. Theoretical predictions including contribution from SM and MSSM Higgs loop corrections are shown.*

# Chapter 2

## The Compact Muon Solenoid

The Compact Muon Solenoid is one of the two general purpose experiments that will operate at the LHC. It is a detector designed to investigate the physics phenomenology coming from  $p$ - $p$  collisions, but it will operate also in heavy ions mode. The experiment is located 100  $m$  underground along the LHC tunnel near the french village of Cessy. The CMS design is driven by the requirements of good reconstruction of charged particles, high electromagnetic energy resolution, precise missing transverse energy and jet measurements and good muon identification and  $p_T$  reconstruction. To achieve these goals, and maintain the detector compactness at the same time, a high solenoidal magnetic field of 4 T has been chosen to provide large bending power.

### 2.1 Overall Design and Physical Requirements

The CMS detector [21, 22] (illustrated in Fig. 2.1) consists in a cylindrical barrel, built of five slices, and two disk-like endcaps. The overall detector length is 21.6  $m$ , its diameter is around 15  $m$  and it has a total weight of approximatively 12500 tons. Due to the challenging operational environment (described in 1.2), high-granularity detectors with good time resolution must be used in order to reduce occupancy. Moreover the high radiation flux expected at LHC design luminosity (1-2  $kGy/year$ ) implies the use of radiation-hard components, especially in the central tracking system.

In order to meet the goals of the LHC physics program, the detector must fulfill the following requirements:

## THE COMPACT MUON SOLENOID

---

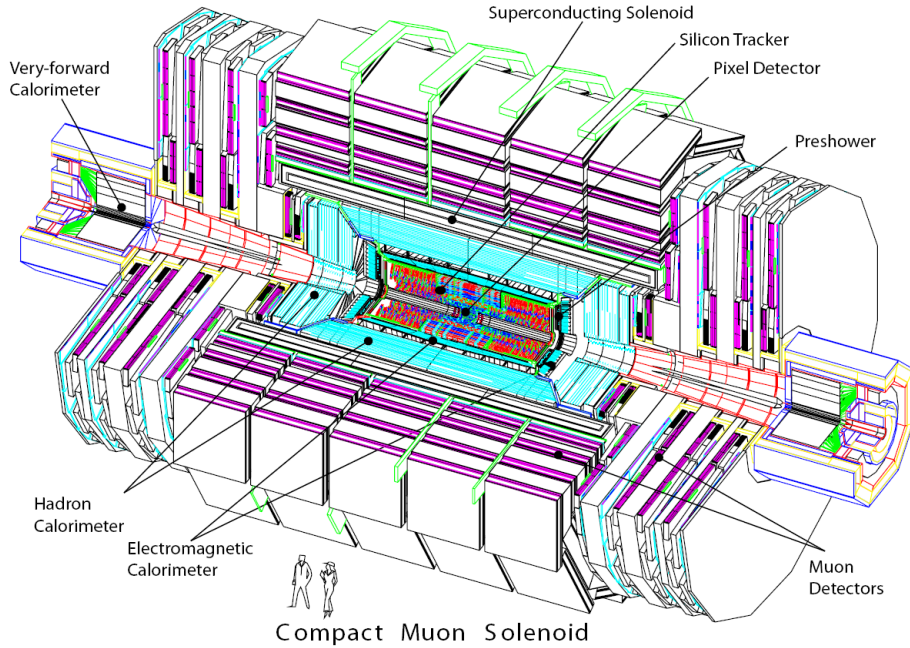


Figure 2.1: *Overview of the CMS detector.*

- Good ability to identify muons and measure their momentum with high resolution in a wide range of angles and momenta, to reconstruct the invariant mass of di-muon systems with high precision (1% resolution at 100 GeV), and determine unambiguously muon charge up to 1  $TeV/c$ .
- High reconstruction efficiency and good momentum resolution measurement for charged particles in the inner tracking system, with particular attention to triggering and offline tagging of  $\tau$  and  $b$  jets.
- High electromagnetic resolution and ability to reconstruct di-photons and di-electron invariant masses with good precision (1% resolution at 100 GeV). Wide geometrical coverage, efficient photon/lepton isolation at high luminosity and good  $\pi^0$  rejection ability.
- Large hermeticity, geometrical coverage and fine geometrical segmentation of hadron calorimeters, in order to ensure good missing  $E_T$  measurements and high resolution reconstruction of di-jet mass.

The compactness of the detector is ensured, using a high field superconducting solenoid, 16 *m* long and of 6 *m* inner diameter, able to generate a field up to 4 *T*. A silicon-based, inner tracking system, an homogeneous *PbWO*<sub>4</sub> scintillating electromagnetic calorimeter and a high hermeticity brass/scintillator sampling hadron calorimeter are accommodated in the solenoid bore. The magnetic field outside the solenoid is strong enough to saturate the iron return yoke where a complex muon spectrometer, based on four layers of Drift Tubes detectors and Cathode Strip Chambers, respectively positioned in barrel and endcaps, is placed. Resistive Plate Chamber complement the other muon subdetectors ensuring redundancy and improving trigger abilities. A longitudinal view of a quarter of the detector, together with transversal view of the barrel region, is given in Fig. 2.2.

In CMS a right handed coordinate system, centered at the nominal collision point is defined: the x-axis points radially inward to the center of the accelerator ring, the y-axis points upward and the z-axis is parallel to the beam pipe (pointing to the Jura mountains). The polar angle  $\theta$  is measured from the z-axis using a  $0 \leq \theta \leq \pi$  range, while the azimuthal angle  $\phi$  is measured in the x-y plane from the x-axis in a  $0 \leq \phi \leq 2\pi$  range. Usually the polar angle is replaced by the pseudorapidity ( $\eta$ ) defined as follows:

$$\eta = -\ln \left( \tan \frac{\theta}{2} \right). \quad (2.1)$$

This is due to the fact that particle production is loosely constant as a function of rapidity ( $y$ ) and  $\eta$  is the ultra-relativistic limit of  $y$ :

$$y = \frac{1}{2} \ln \left( \frac{E + p_z}{E - p_z} \right) \approx \eta = \frac{1}{2} \ln \left( \frac{|\vec{p}| + p_z}{|\vec{p}| - p_z} \right) = -\ln \left( \tan \frac{\theta}{2} \right). \quad (2.2)$$

In the above formulas  $E$ ,  $\vec{p}$  and  $p_z$  represent, respectively energy, 3-momentum and z-axis momentum component of a particle coming out from the interaction point. In the following sections a brief overview of every subdetector is given. Particular attention is also devoted to the description of the CMS trigger and data-acquisition systems. A more detailed analysis of the Drift Tube system and its related trigger electronics is given in chapter 3.

# THE COMPACT MUON SOLENOID

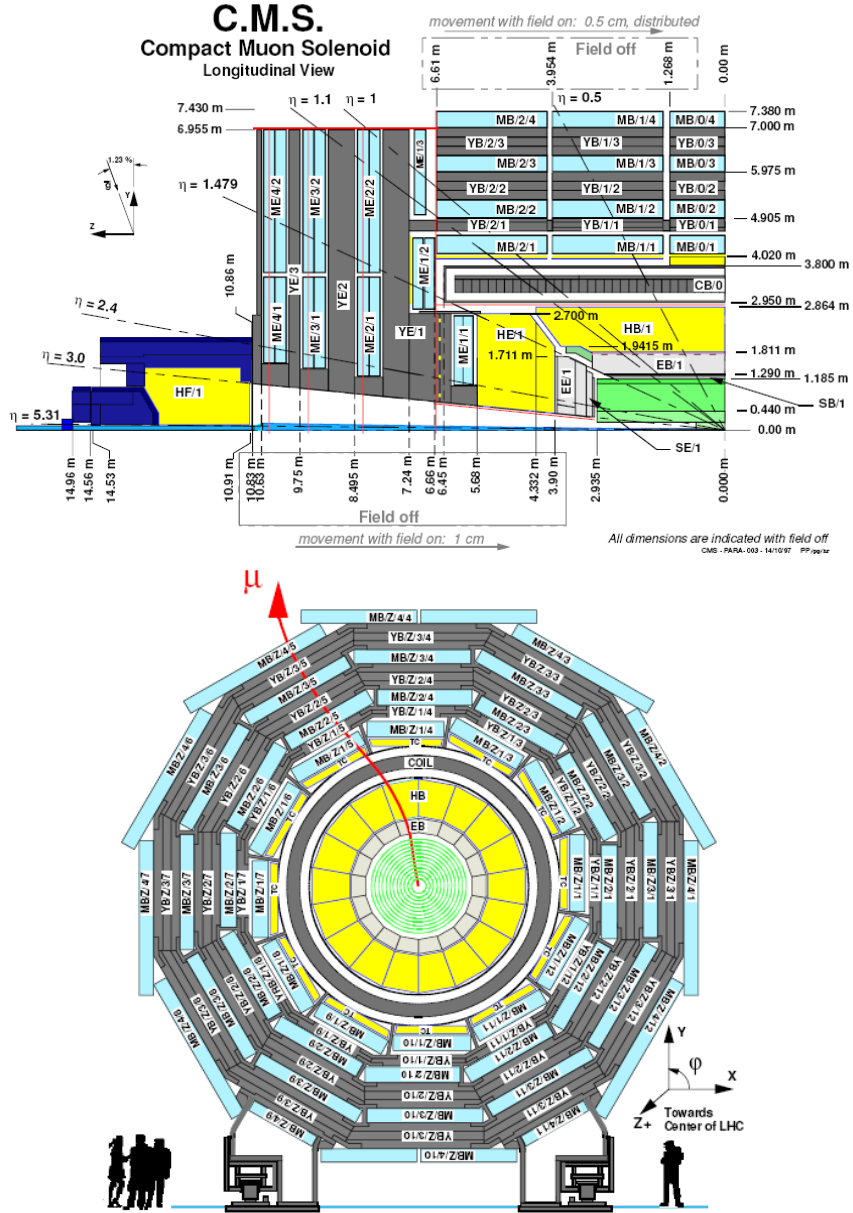


Figure 2.2: Longitudinal view of one quarter of the CMS detector (top); Transversal view of the barrel region of the apparatus (bottom).

## 2.2 The Tracking System

The tracker [23, 24] is the innermost subdetector of the CMS experiment and has a total length of 5.8  $m$  and a diameter of 2.5  $m$ . It is designed to efficiently detect and measure the trajectory of charged particles whose  $p_T$  is above 1  $GeV/c$ , furthermore it has to precisely reconstruct their secondary vertices in order to provide jet-flavour tagging. Together with the electromagnetic calorimeter and muon spectrometer it has a crucial role in the reconstruction of electron and muon tracks respectively. Moreover, due to these characteristics, the tracking system is heavily used in the high level trigger.

At LHC design luminosity around 1000 charged particles coming from  $p$ - $p$  interactions will be produced every 25  $ns$ , thus leading to the need to develop a high granularity and radiation hard system. In order to keep track occupancy low enough to perform efficient and precise measurements, and considering that particle flux quickly decreases with radius, three detection regions can be identified. The CMS tracker is therefore subdivided in a fine granularity *pixel detector* system in its innermost parts, and in *silicon strips* modules of different pitch in its central and external part. This design allows to keep occupancy around 1% everywhere during high luminosity  $p$ - $p$  collisions and still ensure reasonable occupancy levels during  $Pb$ - $Pb$  ones (1% in the pixels and around 20% in the silicon microstrip detector).

The high granularity of the system, however, implies elevated power consumption and, together with the low temperature needed to allow good functioning and prevent radiation damage (around  $-10$   $^{\circ}C$ ), this leads to the need of an efficient cooling infrastructure. In any case the total amount of material in the tracker has to be kept as low as possible in order to reduce multiple-scattering and other interactions, therefore a compromise in the tracker design had to be found.

The mean tracker reconstruction efficiency for charged hadrons varies from 85% for low energy particles ( $1$   $GeV/c < p_T < 10$   $GeV/c$ ) to 95% for high energy ones ( $p_T > 10$   $GeV/c$ ). Moreover it is estimated to be of the order of 90% for electrons and around 98% for muons. The expected transverse momentum resolution in  $r - \phi$  and  $r - z$  planes for 1, 10 and 100  $GeV/c$  particles is shown in Fig. 2.3. As outlined by the left plot the total  $\delta p/p$  estimation remains below 2% up to  $|\eta| < 1.6$ .

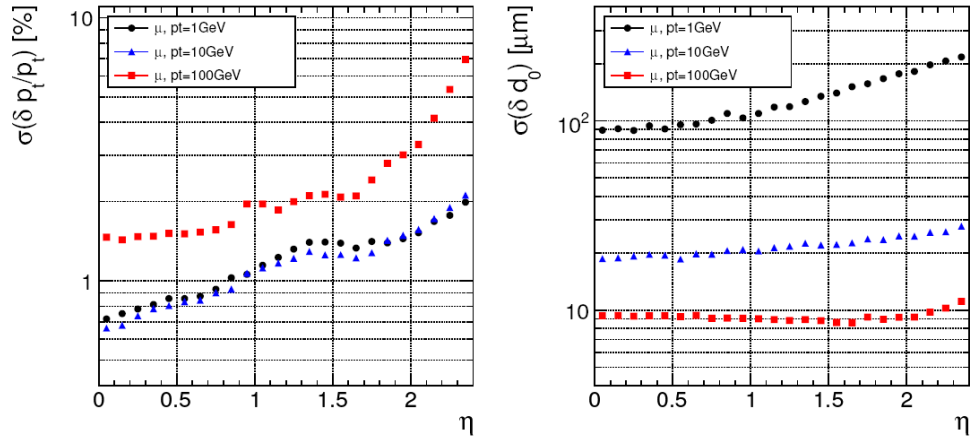


Figure 2.3: Tracker resolution for  $p_T$  (left) and transverse impact parameter (right) as a function of  $\eta$ , computed using single muon samples of transverse momentum 1, 10, 100 GeV/c.

### 2.2.1 The Pixel Detectors

The pixel detector system consists of finely segmented silicon pixels, whose cell size is of  $100 \times 150 \mu\text{m}^2$ , placed on a silicon substrate. It is built to ensure precise 3D vertex reconstruction to allow efficient  $\tau$  and  $b$  jets identification and it covers a pseudorapidity range up to  $|\eta| < 2.5$ . The small pixel size allows to keep single channel occupancy per bunch crossing around  $10^{-4}$  even in the expected high flux scenario ( $10^7$  particles/s at 10 cm).

The final layout of the pixels, shown in Fig. 2.4, consists of three barrel layers (located at a mean radius of 4.4, 73. and 10.2 cm) and two disks (located in a radial region extending from 6 to 15 cm) in the endcaps. During the low luminosity phase, however, only two barrel layers and one endcap disk will be placed.

An interpolated measurement, based on the analog readout of charge deposited in nearby pixels, will ensure a hit resolution of  $10 \mu\text{m}$  in the  $\phi$  plane and  $15 \mu\text{m}$  in the  $z$  one for the barrel layer. Correspondingly a  $15 \mu\text{m}$  and  $20 \mu\text{m}$  respectively in  $\phi$  and  $z$  is expected in the endcaps.

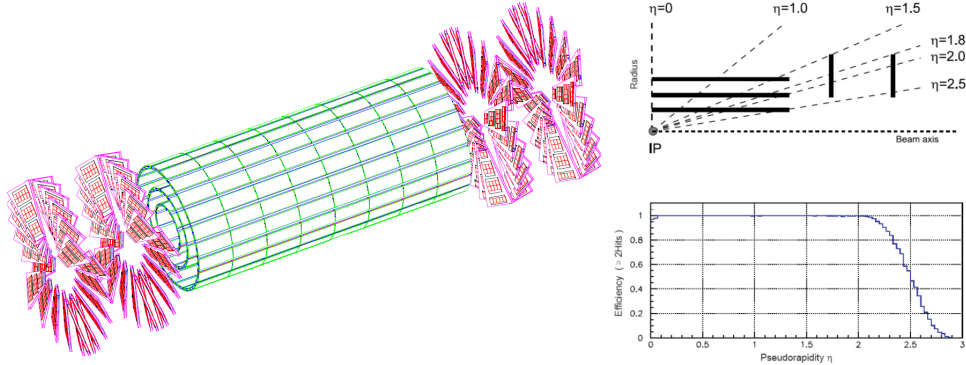


Figure 2.4: Overview of the pixel detector layout (left); longitudinal view of one quarter of the pixel detector and its hit coverage as a function of  $\eta$  (right).

## 2.2.2 The Silicon Microstrip Detectors

The two outermost regions of the tracking system are composed of several layers of silicon microstrip detectors, whose layout is shown in Fig. 2.5. The four innermost barrel layers of the system form the Tracker Inner Barrel (TIB) system, while the the six outer ones constitute the Tracker Outer Barrel (TOB). The Tracker Inner Disk (TID) is made of three layers of disks positioned on each side of the TIB. A group of 9 detector disks perpendicular to the beam axis placed after TOB and TID makes Tracker End-Cap (TEC). The total silicon microstrip detector angular coverage extends to  $|\eta| < 2.5$ , in line with the pixel's one; in the region  $|\eta| > 2.5$ , in fact, the high track density and radiation level forbids the usage of silicon detectors.

The reduced rate in the central (TIB/TID) regions allows to build strips with a minimum cell size of  $10 \text{ cm} \times 80 \mu\text{m}$ , resulting in an occupancy of about 2-3% per BX. The cell thickness in this region is  $320 \mu\text{m}$ . In the TIB the pitch size varies from 80 to  $120 \mu\text{m}$  resulting in a spatial resolution of 23-35  $\mu\text{m}$  respectively. The TID mean pitch size, instead, varies between 100 and 141  $\mu\text{m}$ .

In the outermost region of the tracker, the particle flux is low enough to allow even larger silicon microstrips (which minimal size is of  $25 \text{ cm} \times 180 \mu\text{m}$ ) keeping the occupancy around 1% per BX. The TOB is thus equipped with 500  $\mu\text{m}$  thick strips whose pitch varies between 183 to 122  $\mu\text{m}$  for a single point resolution of 35 and 53  $\mu\text{m}$  respectively. The TEC four innermost rings,

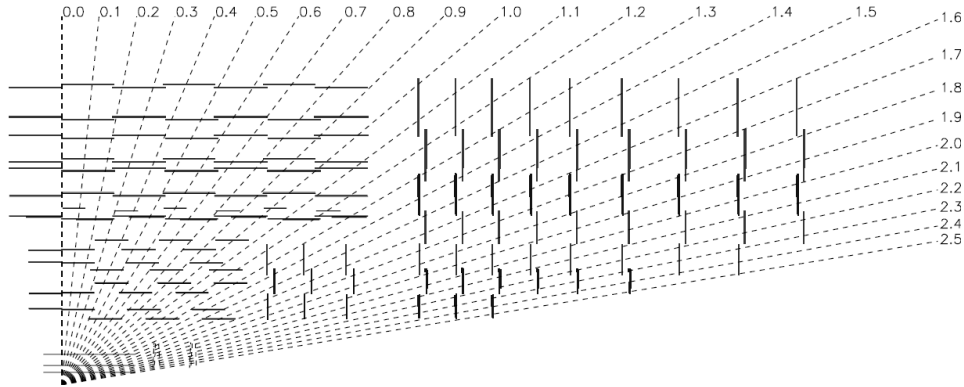


Figure 2.5: *Longitudinal view of one quarter of the silicon strips and pixel detectors.*

instead, have a strip thickness of  $320\ \mu\text{m}$ , whereas the five outermost ones are as thick as the TOB ones. In the TEC case the average pitch dimension varies from  $97$  to  $184\ \mu\text{m}$ .

## 2.3 The Electromagnetic Calorimeter

The Electromagnetic Calorimeter [25] (ECAL) is designed to accurately reconstruct electron and photon position and energy, as well as to perform, in conjunction with the Hadron Calorimeter, precise measurement of hadronic jets. The main driving criteria that lead to its design is the goal to reconstruct  $\gamma\gamma$  invariant mass with a resolution of 1% in order to investigate the  $H \rightarrow \gamma\gamma$  decay channel.

To match this requirement, a lead tungstenate ( $PbWO_4$ ) homogeneous, finely segmented, hermetic calorimeter has been developed.  $PbWO_4$  has been chosen because of its radiation-hardness, as well as for its small Molière radius ( $22\ \text{mm}$ ) and short radiation length  $X_0 = 8.9\ \text{mm}$ , whose ensure good shower containment and compactness. Moreover these crystals are characterized by a very short scintillation-decay time, that allows to collect about 80% of the light in the read out electronics within a  $25\ \text{ns}$  time period. On the other hand, the low ( $4.5\ \gamma/\text{MeV}$  at  $18\ ^\circ\text{C}$ ) emitted light output, forces to use photodetectors with high intrinsic gain that can operate in an high mag-

netic field. Therefore solutions based on Vacuum Photodiodes (VPT) and Avalanche Photodiodes (APD) are thus been adopted in endcaps and barrel respectively. As the latter has a response which is sensitive to temperature, thermal stability up to  $0.1\text{ }^{\circ}\text{C}$  is required to preserve energy resolution.

The crystals have a length of  $230\text{ mm}$  in the barrel and  $220\text{ mm}$  in the endcaps corresponding respectively to  $25.8$  and  $24.7 X_0$ . They are trapezoidal in shape with a square front size of  $22 \times 22\text{ mm}^2$  in the barrel and  $28.2 \times 28.6\text{ mm}^2$  in the endcaps. Figure 2.6 shows the total geometrical coverage of the system, which extends up to  $|\eta| < 3.0$ .

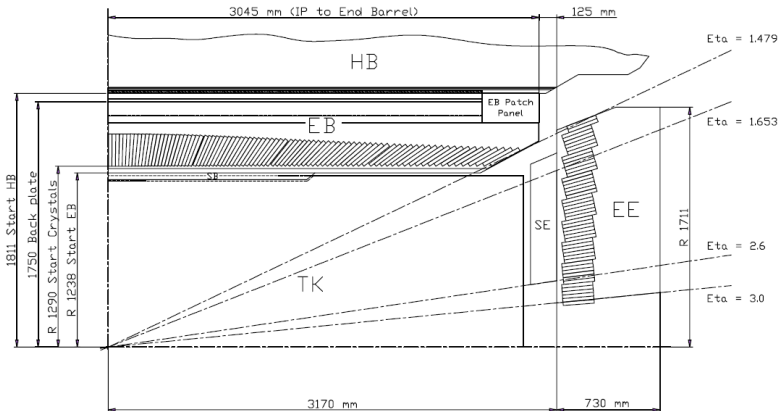


Figure 2.6: Longitudinal view of one quarter of the ECAL subsystem.

In order to allow  $\pi_0$  identification and improve photon and electron position measurements, a preshower detector is installed in front of both endcaps. It consists of a two-layer sampling calorimeter, where lead radiators are alternated to silicon strip detectors, for a total material thickness of about  $3 X_0$ .

For energies below an approximative value of  $500\text{ GeV}$ , where shower leakage starts to be significant, the ECAL energy resolution can be parameterized as follows:

$$\left(\frac{\sigma}{E}\right)^2 = \left(\frac{S}{\sqrt{E}}\right)^2 + \left(\frac{N}{E}\right)^2 + C^2 \quad (2.3)$$

where  $S$  refers to the *stochastic* term due to fluctuations in lateral shower containment, photostatistics and energy deposit in the preshower (where

present),  $N$  is the *noise* term related to electronics, digitization and pile-up, and  $C$  is a *constant* contribution due to ECAL calibration, non uniformity of longitudinal light collection and leakage from the back of the crystals. Studies performed during test beams allowed to estimate these parameters to be  $S = 2.8\%$ ,  $N = 0.12\%$  and  $C = 0.30\%$ .

## 2.4 The Hadron Calorimeter

The Hadron Calorimeter [26] (HCAL) is used, together with the ECAL, to perform measurements on direction and energy of hadronic jets and to estimate the amount of missing transverse energy (missing  $E_T$ ) of each event. Furthermore HCAL will be also used to improve identification of electrons, photons and muons. The request to perform precise missing  $E_T$  measurement implies the development of a very hermetic system, whose design is constrained by compactness requests and by the high magnetic field.

In order to fulfill these requirements a sampling calorimeter system based on brass absorber layers alternated to active plastic scintillators has been built. The signal coming from active scintillators is read out with embedded wavelength-shifting fibers (WLS) and conveyed via clear fiber wave-guides to hybrid photodiodes. The choice of brass as absorber material has been driven from its short interaction length  $\lambda_I$  and its non-magnetic nature.

A longitudinal view of the HCAL layout is shown in Fig. 2.7. The barrel calorimeter (HB) covers an  $\eta$  region up to 1.4 and its readout segmentation (of  $\Delta\eta \times \Delta\phi = 0.087 \times 0.087$ ) is tight enough to allow proper di-jet separation and mass resolution. The HB total depth increases as a function of  $\eta$ , raising from  $5.15 \lambda_I$  at  $\eta = 0$  to  $10.15 \lambda_I$  at  $\eta = 1.3$ . In order to improve hadron shower containment within the barrel an *outer calorimeter* (HO) is placed outside the magnet. It consists of scintillator tiles, whose segmentation matches the Drift Tubes one, and serves as a “*tail catcher*” increasing the effective thickness of HB over  $10 \lambda_I$  everywhere, thus improving missing  $E_T$  resolution.

An endcap calorimeter (HE) is also placed inside the magnet bore, covering the  $1.4 < |\eta| < 3.2$  region. Its segmentation overlaps with the HB one and its average depth is about  $10.5 \lambda_I$ . Outside the magnet a forward calorimeter (HF) covers the  $\eta$  region up to 5.2. Due to the harsh conditions at high  $\eta$ , radiation hard quartz fibers have been chosen as active medium.

The expected energy resolution of the system (for  $E$  expressed in GeV)

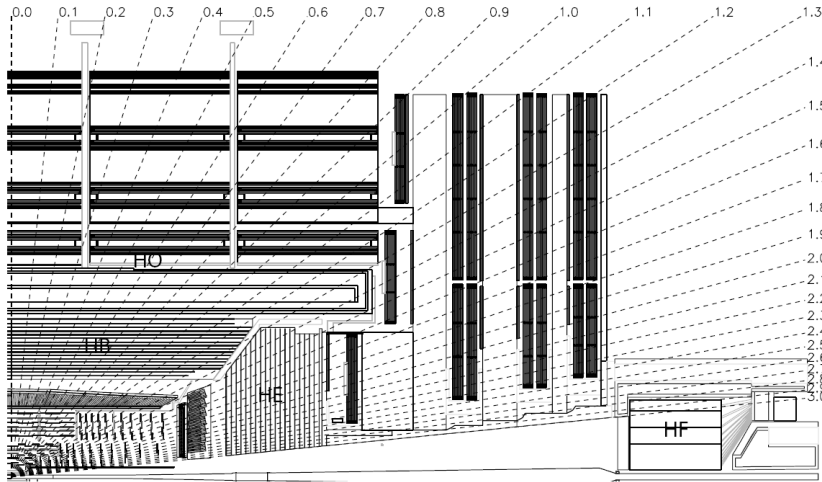


Figure 2.7: Longitudinal view of one quarter of the HCAL subsystem.

varies from  $\sigma/E \approx (65/\sqrt{E} \oplus 5)\%$  in the barrel, to  $\sigma/E \approx (83/\sqrt{E} \oplus 5)\%$  in HE, to  $\sigma/E \approx (100/\sqrt{E} \oplus 5)\%$  in HF.

## 2.5 The Magnet

The CMS magnet system [27] is designed taking into account the strict requirements of identification of the charge of high  $p_t$  muons and precise measurement of momentum of charged particles requested at the LHC. In fact, in order to correctly determine the muon charge up to  $1 \text{ TeV}/c$  a momentum resolution of  $\Delta p/p \lesssim 10\%$  is requested in the whole range of momenta. Moreover a 1% resolution on the reconstruction of charged particles at  $100 \text{ GeV}/c$  is needed.

To fulfill these requirements, and ensure compactness of the detector at the same time, an high field, modest sized, superconducting solenoid has been developed. The CMS magnet is  $12.9 \text{ m}$  long, with an inner diameter of  $5.9 \text{ m}$ , and it is able to generate a 4T magnetic field. The magnetic flux is returned using an iron yoke which also hosts the muon spectrometer. The 2 T residual field present inside the iron provides enough bending power to perform an efficient  $p_T$  based muon trigger selection in a  $|\eta| < 2.4$  pseudorapidity region. A brief list of the magnet parameters is given in table 2.1.

Parameter	Value
Field	4 T
Residual field in the yoke	2 T
Inner bore	5.9 m
Length	12.9 m
Number of turns	2168
Operation temperature	4.5 K
Nominal current	19.14 kA
Stored energy	2.6 GJ
Hoop stress	64 atm

Table 2.1: *Parameters of the CMS superconducting solenoid.*

## 2.6 The Muon System

Many of the interesting physical processes foreseen at the LHC will be characterized by final states which will involve the presence of high  $p_T$  muons (as described in 1.2). Hence a robust and redundant muon spectrometer is needed to provide precise muon identification, high resolution  $p_T$  measurements and effective trigger capabilities.

The muon system [28] is the outermost group of subdetectors of the CMS experiment, it covers an  $\eta$  region up to 2.4 and its layout is shown in Fig. 2.8. It consists of three different types of gaseous detectors, chosen in function of the large surface to be covered, and whose design is driven by the differences in the radiation environment and magnetic field at different values of  $\eta$ . Drift Tubes Chambers (DTs) are used in the barrel (up to  $|\eta| < 1.2$ ) where low track occupancy and residual magnetic field are expected. The endcaps ( $0.8 < |\eta| < 2.4$ ) are instead equipped with Cathode Strip Chambers (CSCs), chosen to cope with the high particle flux and non uniformity of the magnetic field at large  $\eta$ . In order to ensure redundancy and improve trigger capabilities, Resistive Plate Chambers (RPCs) complement DT and CSC based detectors, both in barrel and endcaps, covering an  $\eta$  region up to 2.1. RPCs allow only coarse spatial resolution measurements, however they are characterized by fast response and their excellent time resolution provides unambiguous BX identification to the muon trigger.

For muons up to  $p_T \approx 200 \text{ GeV}/c$  the system resolution is limited by

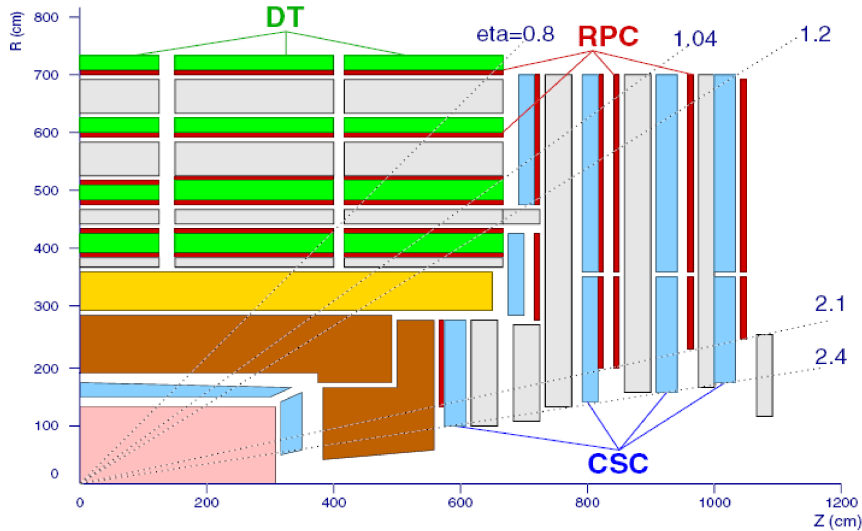


Figure 2.8: *Longitudinal view of one quarter of the muon spectrometer.*

the multiple scattering the particle is affected to before reaching the first spectrometer station, at higher  $p_T$  the precision of the chamber measurements dominates. Figure 2.9 shows the total  $p_T$  resolution as a function of  $\eta$ , as well as the one obtained using only information coming from the tracker or the muon system only. It can be seen that, at low transverse momentum, tracker precision dominates, while at higher  $p_T$  the combination of the two systems improves the overall resolution.

### 2.6.1 The Drift Tube Chambers

The barrel region of the muon system is characterized by low residual magnetic field and occupancy, therefore Drift Tubes technology can be used to ensure precise spatial measurements and large surface covering.

The DT system layout is shown in Fig. 2.10. It follows the yoke segmentation and consists of 5 iron wheels composed of 12 azimuthal sectors, covering an angular region of approximately  $30^\circ$  each. Every wheel consists of four concentric rings of chambers, called *stations* and named respectively MB1/2/3/4 (where MB stands for *Muon Barrel*). Each station is formed by 12 DT *chambers* with the exception of MB4 which consists of 14 of them.

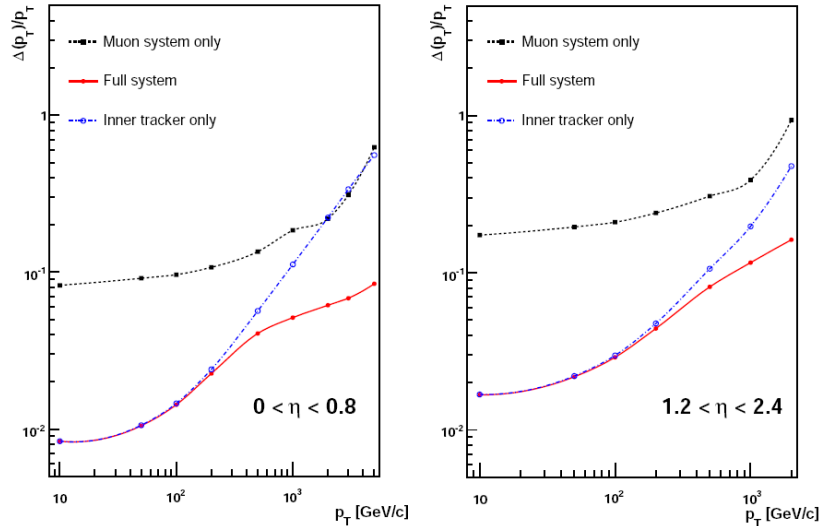


Figure 2.9: *Muon transverse momentum resolution as a function of  $p_T$  in the barrel (left) and endcap (right) region; results obtained using tracker only, muon system only, and combination of muon spectrometer and tracker information are shown.*

The basic detector element of the DT system is a rectangular drift tube *cell* with a transversal size of  $4.2\text{ cm} \times 1.3\text{ cm}$ , and whose length varies from 2 to 4 *m*. Cells are filled with a 85%/15%  $Ar/CO_2$  gas mixture and are grouped parallelly to form detection *layers*. Groups of four layers are assembled to form a *superlayer* and a block of two superlayers measuring the  $\phi$  coordinate plus one measuring the  $z$  one finally forms a DT chamber. The only exception to this rule applies to the MB4 stations where only the two  $\phi$  superlayer are present. A schematic layout of a single DT chamber is shown in Fig. 2.11

DT cells have an efficiency of 99.8% and a spatial resolution around  $200\ \mu\text{m}$ , leading to a radial resolution of  $100\ \mu\text{m}$  for and 8-point  $\phi$  reconstructed segment. A more exhaustive description of the DT system and of its overall performances, is given in chapter 3.

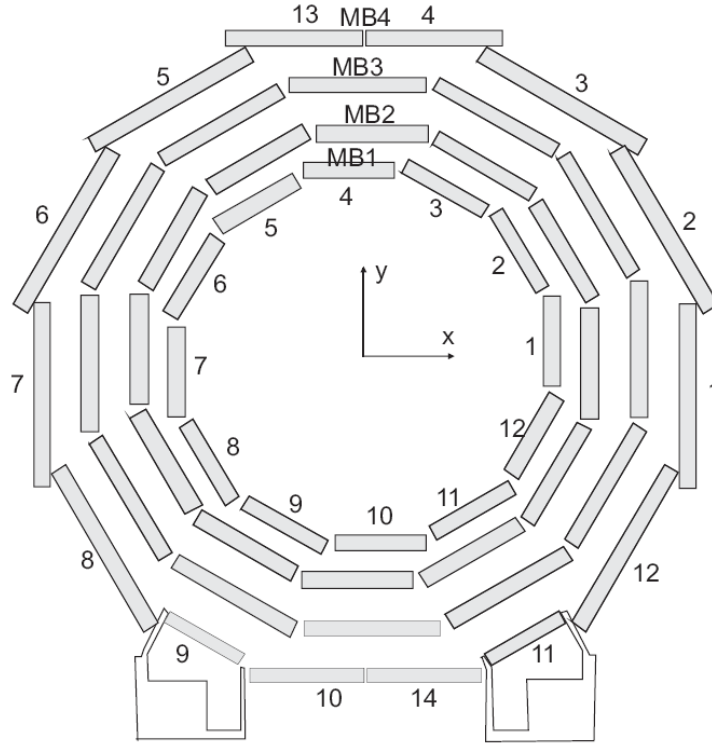


Figure 2.10: *Transversal view of the CMS DT system. Station and sector numbers are shown in the figure.*

## 2.6.2 The Cathode Strip Chambers

The high magnetic field and particle rate expected in the muon system end-caps does not allow to use drift tubes detectors to perform measurements at large  $\eta$  values. Therefore a solution based on Cathode Strip Chamber detector has been adopted. The CSC are gaseous ionization detector working in avalanche mode and characterized by a short drift length. Information about the position of the incoming particle is collected both in the anode wire and on a group of finely segmented cathode strips. The latter allows to perform center of gravity measurements ensuring high position resolution, while the former is characterized by a fast signal suitable for trigger purposes.

The CSC layout is shown in Fig. 2.12 (left). Trapezoidal detector cham-

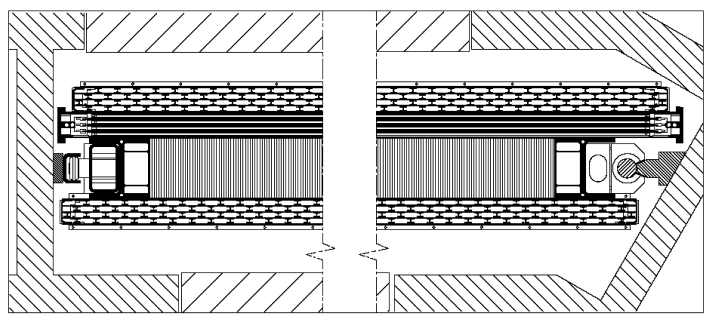


Figure 2.11: *Schematic view of a CMS drift tube chamber.*

bers are arranged to form four *disks* of concentric *rings* placed in between the endcap iron yokes. All rings but the third of the first endcap disk (ME1/3), are arranged staggered in  $\phi$  in order to avoid azimuthal dead regions. The innermost ring of each disk hosts 18 chambers, with the exception of the first one which hosts 36 chamber like the rest of the system.

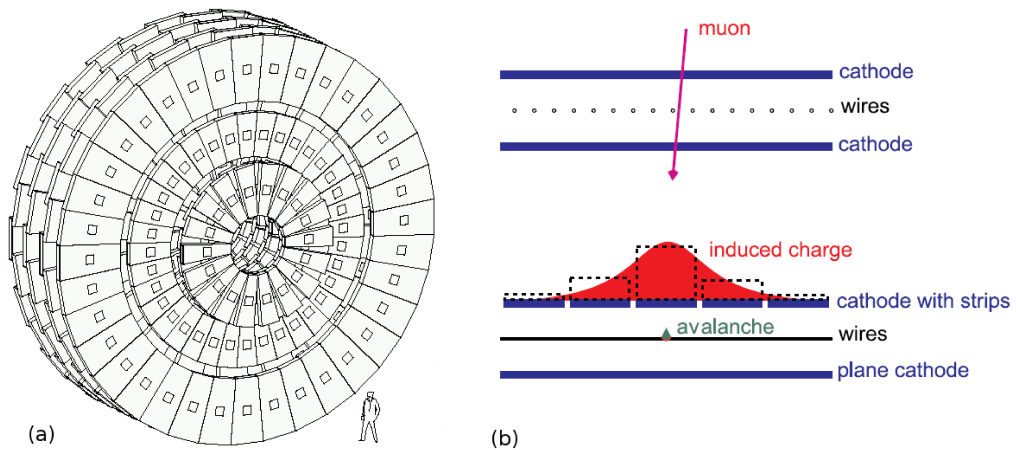


Figure 2.12: *Layout of the CSC subsystem (left). Schematic overview of a CSC chamber (right).*

One single chamber is composed of 6 layers of 9.5 mm thick arrays of

anode wires enclosed between two cathode planes, as shown in Fig. 2.12 (right). One of the cathodes is characterized by a fine strip segmentation which allows to perform precise radial measurements, while anode wires, placed perpendicular to the strips, are used to measure the  $r$  coordinate. Anode information is collected in groups whose size varies from 5 to 16 wires in order to reduce the number of readout channels. The chambers are filled with a 30%/50%/20%  $Ar/CO_2/CF_4$  gas mixture. The ME/1 disk operates in higher magnetic field conditions with respect to the rest of the system, so anode wires are tilted by  $20^\circ$  in order to compensate for the Lorentz drift effect. Moreover gap thickness is reduced to 6 mm and the number of strips is double in the  $|\eta| > 2.0$  region.

Strip measurements resolution varies from  $\sim 70 \mu m$  for the innermost stations to  $\sim 150 \mu m$  for the outermost ones, while  $r$  can be determined with a precision of  $\sim 0.5 cm$ .

### 2.6.3 The Resistive Plates Chambers

Resistive Plates Chambers are used both in barrel and endcaps, complementing DT and CSC systems, in order to ensure robustness and redundancy to the muon spectrometer. RPCs are gaseous detectors characterized by a coarse spatial resolution, but are able to perform precise time measurements, comparable with the ones provided by scintillators. This ensures precise BX identification to the muon trigger system.

CMS uses double-gap RPC chambers composed of 4 bakelite planes alternated to form two, 2 mm thick, gas gaps as shown in Fig. 2.13. The planes are coated by graphite to make electrodes that are set at 9.5 kV of potential difference. The central part of the chamber is equipped with insulated aluminum strips, used to collect the signal generated by crossing particles. The design choice of using double gap chambers is adopted to increase the signal induced on them.

In the barrel the strips are rectangularly segmented (12.1 to 41 cm wide and 80 to 120 cm long) and run along the beam axis, whereas the endcaps are equipped with trapezoidal shaped strips covering approximately the range  $\Delta\phi = 5\text{-}6^\circ$ ,  $\Delta\eta = 0.1$ . No measurement is possible in the  $\eta$  coordinate, apart from the constraint imposed by the strip length. The gas mixture used in the gap is a 90%/5% mixture of freon ( $C_2H_2F_4$ ) and isobutane ( $i - C_4H_{10}$ ). In order to sustain higher rates, the detector operates in *avalanche*

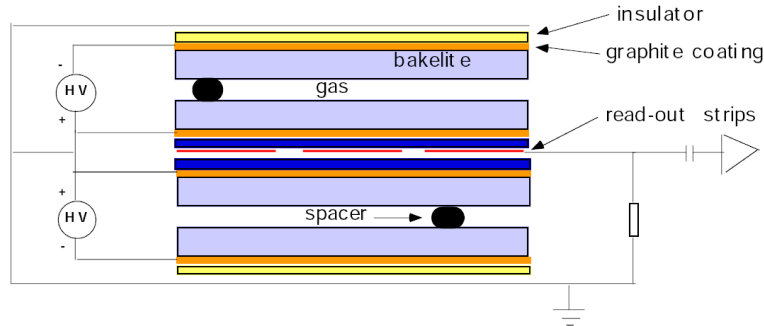


Figure 2.13: *Schematic view of a CMS double gap RPC.*

instead of using the most common *streamer* mode, but due to the reduced gas multiplication, improved electronic multiplication is requested.

In the barrel region the system layout follows the DT segmentation and two RPC stations are attached to each side of the two innermost DT chambers of a sector, whereas one single RPC is attached to the inner side of the third and fourth DT chambers. This solution ensures to extend the low  $p_T$  reach of the trigger system in the barrel, in fact this allows to detect even low  $p_T$  muons using 4 RPC layers before they stop in the iron yoke. This kind of solution is not needed in the endcaps since, at higher  $\eta$  same values of  $p_T$  correspond to higher total momentum.

## 2.7 Trigger and Data Acquisition

As previously outlined in 1.2.1, at the LHC design luminosity of  $10^{34} \text{ cm}^{-2} \text{ s}^{-1}$ , a total event rate of the order of  $10^9$  Hz is expected. Hence, considering the approximative amount of data collected per single BX, which is about 1 MB, it results that an effective trigger strategy, used to select interesting events among all physical interactions, had to be adopted. In order to cope with the 100 Hz limit imposed by the final storage system, a total reduction rate of the order of  $10^7$  has to be achieved.

Besides the high rejection factor required, trigger algorithms have also to be sensitive to the physical content of the various events. As shown in Fig. 2.14, processes as  $Z \rightarrow ll$  and  $Z \rightarrow l\nu$  have cross sections which are orders of magnitude higher than the ones characterizing many other interesting

## 2.7 — Trigger and Data Acquisition

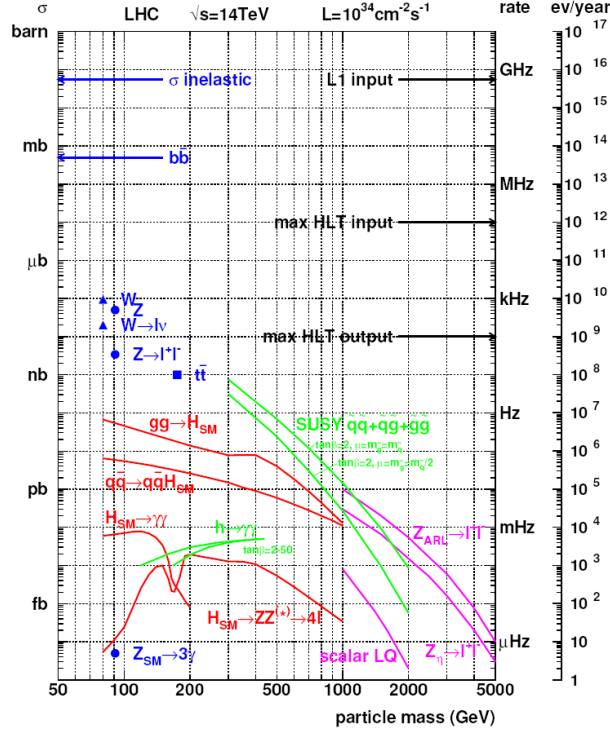


Figure 2.14: Cross sections and rates at  $10^{34} \text{ cm}^{-2} \text{ s}^{-1}$  as a function of the mass of the generated particle.

phenomena, thus they would tend to saturate selections based on simple high  $p_T$  lepton identification. All these constraints lead to the need to develop a trigger system whose sophistication is comparable to the one reached by the offline reconstruction algorithms.

Furthermore the BX frequency of 40 MHz requires the development of a system able to take a selection/rejection decision every 25 ns. Since this time is by far too short to collect all the information coming from all the subdetectors and process it in a single step, a trigger architecture based on different levels of increasing complexity, has been adopted. Within this scenario a Level 1 Trigger (L1T) system [29], built using dedicated hardware electronics, operates a first selection on the basis of coarsely segmented informations only coming from calorimeters and muon chambers, reducing significantly the

amount of data to be further processed. Later on an High Level Trigger (HLT) system [30] performs a more refined analysis, on the already reduced event sample, on the basis of the full information available from all the detectors. The HLT is a programmable software system running on a filter farm of about a thousand of commercial processors. The design input rate limit of the CMS Data Acquisition (DAQ) system is set to be  $100\text{ kHz}$  thus leading to a reduction of the order  $10^4$  to be performed by the L1T, followed by a further  $10^3$  rejection in the HLT to cope with storage system requirements.

### 2.7.1 The Level-1 Trigger System

The Level 1 trigger [29] is designed to take a fast accept/reject decision performing a rough reconstruction, on the basis of information from calorimeters and muon stations, every BX. To reach this goal it is implemented using custom developed programmable hardware. Due to flexibility requirements, Field Programmable Gate Arrays (FPGA) are used where possible but solutions based on Application Specific Integrated Circuits (ASICs) and programmable Lookup Tables (LUTs) are also taken into account when speed, density and radiation-hardness become important.

The system has to run in a dead time free mode, and take an accept/reject decision every  $25\text{ ns}$ , coping with the BX frequency. To fulfill this requirement a synchronous pipelined architecture, where every processing element takes less than  $25\text{ ns}$  to complete its operation, is used. During the L1T processing phase, the full detector information is stored in pipelined buffers, whose length is technically constrained to 128 BX. This implies that Level 1 decision has to be taken after a fixed maximum time of  $3.2\ \mu\text{s}$  after the interaction occurs. Considering the transmission time between the detector and the counting room (where some of the trigger components are located) and typical subsystem latencies (i.e. the  $400\text{ ns}$  drift time of the DTs), it results that the time actually left for computation is limited to  $1\ \mu\text{s}$ .

The DAQ design input rate of  $100\text{ kHz}$  implies that, at L1T level, a reduction factor of  $10^4$  is required. In practice a safety factor of three, which takes into account uncertainties in the basic simulation of the physics processes involved, is assumed, reducing boundary on the L1T expected output rate limit to  $30\text{ kHz}$ . Furthermore, during the low-luminosity phase, the DAQ rate will be reduced to  $50\text{ kHz}$  leading to an estimated rate of  $16\text{ kHz}$  for the L1T.

As outlined in Fig. 2.15, the L1T system can be further subdivided into three major subsystems: The Muon Trigger, The Calorimeter Trigger and the Global Trigger. The first two systems process information coming from muon spectrometer and calorimeters respectively, and do not have to perform the task of rejecting/accepting events by themselves. Instead they identify and perform sorting on various types of *trigger objects* (such as electron/photon, jets and muons) and then they forward the four best “*candidates*” of each kind of trigger object to the Global Trigger where the final decision is taken.

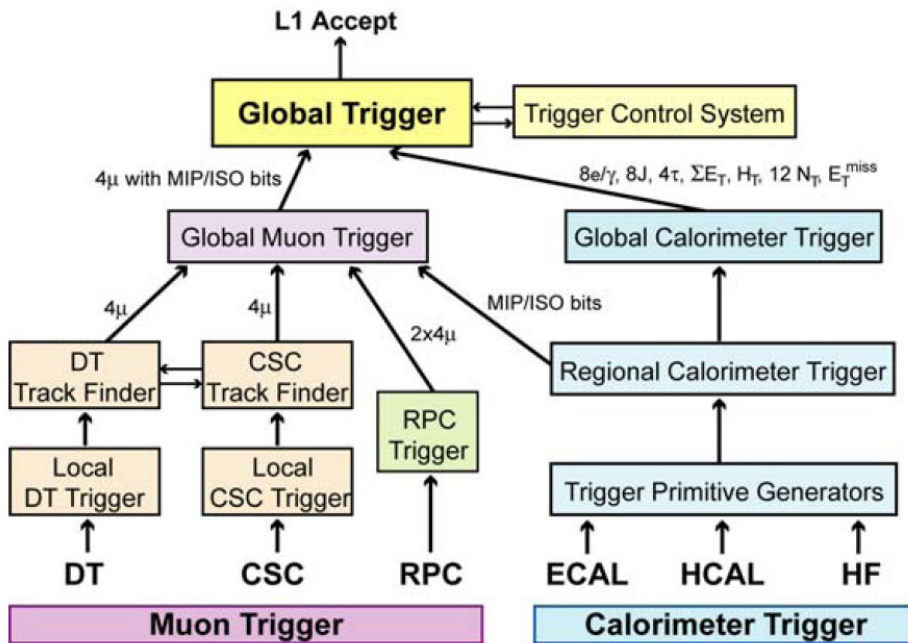


Figure 2.15: Architecture of the CMS Level-1 trigger system.

In order to perform the ranking, a multi level architecture which processes information taking into account increasingly larger portions of the various subsystems is mostly used. Trigger Primitives Generators (TPGs) (also referred as Local Triggers) perform a local reconstruction using a small fraction of the interested subdetector, to identify energy deposits in calorimeters or precise hit patterns in the muon chambers, producing basic objects, called *trigger primitives*, which are used in the following step. Regional Triggers

(RTs) (usually referred as Track Finders within the muon subsystem) are then called to identify high level trigger objects matching the informations coming from the different primitives, and deliver interesting quantities, such as  $p_T$  or  $E_T$ . After that, Global Calorimeter and Muon triggers combine the information coming from different RTs, and perform the final ranking on the basis of physical informations as well as quality bits assigned from the previous components of the trigger chain. Finally the GT selects the events on the basis of programmable trigger conditions. These can be requirements on the presence of different objects whose energy or momenta corresponds to predefined thresholds defined in advance, or topological constraints and correlations between the trigger objects themselves.

In the following sections a brief description of the various L1T subsystems is carried out.

### L1 Calorimeter Trigger

The Level 1 Calorimeter Trigger is designed to identify single trigger objects such as *isolated/non-isolated electrons/muons*, *central/forward jets* as well as global quantities like *total/missing  $E_T$* ,  $H_T$  (the scalar transverse energy sum of all jets above a programmable threshold) and *jet multiplicities*. In addition it performs BX identification and provides to the Global Muon Trigger informations concerning muon energy deposits in the calorimeters.

The Level 1 Calorimeter Trigger logic is implemented in a multi level architecture, consisting in a TPG subsystem, which operates on ECAL/HCAL energy deposits, followed by Regional Calorimeter (RCT) and Global Calorimeter (GCT) Triggers which perform further refinement on the basis of trigger *primitives/objects*.

The calorimeter TPGs operate on geometrical partitioned regions of the full ECAL/HCAL subdetectors and they perform BX identification as well as transverse energy measurement. They also provide to the trigger primitive a fine grain bit, used for background rejection or identification of the passage of a minimum ionizing particle. The basic geometrical unit where TPGs computations are performed is called *trigger tower*. In the azimuthal region up to  $|\eta| < 2$  the towers have a size of  $\Delta\phi \times \Delta\eta = 0.087 \times 0.087$ ; while at larger  $\eta$  the  $\Delta\eta$  window size is variable and increases up to 0.35. Groups of  $5 \times 5$  ECAL towers form a single trigger tower in the barrel, while in the endcaps, a variable number of crystals is clustered together in order to form

ECAL trigger towers that match HCAL ones. In the HCAL a trigger tower is made of a single HCAL tower up to  $|\eta| < 1.74$  while at larger  $\eta$  one physical HCAL tower has twice the  $\phi$  dimension of a trigger tower. The very forward region is equipped with towers that have a size of  $\Delta\phi \times \Delta\eta = 0.348 \times 0.5$ .

TPGs informations are then transmitted through high speed serial links to the regional Calorimeter Trigger (RCT) which elaborates them in order to obtain high level trigger objects such as isolated/non-isolated electron/photons, central/forward jets and total/missing  $E_T$ . Quiet bits and minimum ionizing particle (MIP) bits are computed as well, since they can be used to help muon trigger selection. The basic unit used by RCT is the *trigger region*, which consists of groups of  $4 \times 4$  trigger towers, both in barrel and endcaps, with a size of around  $\Delta\phi \times \Delta\eta = 0.35 \times 0.35$ . Instead very forward calorimeter towers represent a region by themselves due to their size.

Then the Global Calorimeter Trigger (GCT) determines the total energy deposit, missing  $E_T$  magnitude and direction, twelve jet counts (computed using different  $E_T$  thresholds) and  $H_T$ . Furthermore it performs the final sorting of trigger candidates received from the RCT and send the quiet and MIP bits to the Global Muon Trigger. Finally it forwards these informations to the GT.

## L1 Muon Trigger

The Level 1 Muon Trigger is devoted to the reconstruction of muon position and  $p_T$  as well as the assignment of the particle origin in terms of BX. All the three subsystems described in 2.6 take part to the trigger process, providing robustness and redundancy to the system. CSC and DT based triggers ensure, in fact, good spatial resolution, whereas excellent time resolution is obtained using RPCs. These complementing detector technologies are also sensitive to different types of backgrounds, thus leading to good noise rejection capabilities.

CSC and DT triggers operate using a two-level logic, based on TPGs and RTs, similar to the one used by calorimeters. On a first processing phase the information coming from every single DT/CSC chamber is elaborated by on-board DT/CSC-TPGs, which operate reconstruction algorithms on the detector signals. They are in charge for BX assignment, trigger segment position/direction estimation, and computation of a system dependent quality bit.

Information coming from different stations are then passed to the DT and CSC Track Finders (DTTF - CSCTF) whose build full muon tracks on the basis of local reconstructed primitives, assign them charge sign and estimates their transverse momentum value. They also deliver quality bits related to the number of stations used for reconstruction. In the  $\eta$  region, where muons coming from the interaction point cross both DT and CSC subsystem (the so called *overlap region*), exchange of informations between DTTF and CSCTF is performed in order improve regional track reconstruction.

The RPC trigger system, instead, does not perform a two step (local-regional) reconstruction. After synchronization and cluster reduction, in fact, hits from all the stations are collected by a Pattern Comparator Trigger (PACT) that looks for space-time correlations in order to perform matching and  $p_T$  assignment. Pattern identification is carried out in case at least three of the four stations are involved in the reconstruction process. In the case of the barrel, where six RPC layers are present, *low- $p_T$*  and *high- $p_T$*  muon identification is performed independently, using both the RPC layers attached to the two innermost DT stations, or the innermost RPC layer attached to the four DT stations respectively. The four highest  $p_T$  muons coming from both DT and RPC in the barrel, and both DT and CSC in the endcaps, are then forwarded to the Global Muon Trigger (GMT) for final processing.

The GMT attempt to match information from the different subsystems and combine their parameters in an optimal way. High background rejection can be achieved accepting candidates that are detected in at least two of the subdetectors, on the other side high efficiency can be achieved asking that a candidate is found in at least one trigger subsystem. Good balance between the two can be ensured by accepting matched candidates independently from their quality word, and perform unmatched candidates selection on the basis of their quality. Furthermore Quiet and MIP bit can be used to associate muon triggers with calorimeter information and optionally confirm the muon candidate or require that it is isolated. The resulting list of trigger objects is then forwarded to the GT system for final processing. More in depth description of the CSC and RPC trigger systems can be found in [29], while more exhaustive analysis of the DT-TPG and DTTF subsystem is given in chapter 3

## L1 Global Trigger

The GT is in charge to take the level 1 accept/reject decision on the basis of the information provided by the GCT and the GMT and send the Level 1 Accept signal (L1A) to the DAQ system. This information consists of sorted candidates as electrons, photons, muons and central and forward hadronic jets as well as global quantities like total and missing  $E_T$ , the sum of transverse energies over a programmable threshold ( $H_T$ ) and twelve, threshold dependent, jet multiplicities.

GT trigger algorithm calculations are performed in the Global Trigger Logic (GTL) unit, then the output of the GTL is sent to the Final Decision Logic (FDL) in the form of one single bit per algorithm. Finally the information is collected by the Global Trigger Front-End (GTFE) which appends the GPS event time received from the machine and sends it to the DAQ system for the readout.

Up to 128 algorithms can be executed in parallel, the most basic ones consisting of simple  $p_T$  or  $E_T$  thresholds cutoff on single trigger objects (or pairs of objects), or requirements on the various jet multiplicities values. However more complex computations based on the presence of different kind of objects having precise topological conditions or correlations can be applied. In any case, “inclusive” criteria should be used whenever possible, to avoid biasing of the selected event sample.

The choice of L1T thresholds is related to the DAQ bandwidth availability previously mentioned in 2.7. The maximum L1T available rate can be further subdivided among different streams corresponding to the selection of any of the trigger objects previously described, or combination of them. The resulting map of thresholds, and corresponding rates is conventionally referred as *trigger table* [30]. The present L1T trigger tables for the low and high luminosity scenario are shown, respectively, in table 2.2 and 2.3. 1 kHz of the expected L1T bandwidth is allocated to select minimum bias events that will be used for calibration and monitoring purposes.

### 2.7.2 The High Level Trigger and DAQ

The CMS High Level Trigger [30] has the task to further reduce the (up to) 100 kHz event rate delivered from the L1T to the DAQ system to match the 100 Hz limit required from the storage system. Thus a rejection factor of about  $10^3$  has to be achieved. To fulfill this requirement, the HLT performs

THE COMPACT MUON SOLENOID

<b>Trigger</b>	<b>Threshold (GeV)</b>	<b>Rate (kHz)</b>	<b>Cumulative Rate (kHz)</b>
Inclusive isolated electron/photon	29	3.3	3.3
Di-electrons/di-photons	17	1.3	4.3
Inclusive muon	14	1.7	7.0
Di-muons	3	0.9	7.9
Single tau-jet	86	2.2	10.1
Two tau-jets	59	1.0	10.9
1-jet / 3-jets / 4-jets	177/86/70	3.0	12.5
Jet·miss $E_T$	88 · 36	2.3	14.3
Electron·Jet	21 · 45	0.8	15.1
Minimum-bias		0.9	16.0

Table 2.2: *Level 1 trigger Table at low luminosity.*

<b>Trigger</b>	<b>Threshold (GeV)</b>	<b>Rate (kHz)</b>	<b>Cumulative Rate (kHz)</b>
Inclusive isolated electron/photon	34	6.5	6.5
Di-electrons/di-photons	19	3.3	9.4
Inclusive muon	20	6.2	15.6
Di-muons	5	1.7	17.3
Single tau-jet	10	5.3	22.6
Two tau-jets	67	3.6	25.0
1-jet / 3-jets / 4-jets	250/110/95	3.0	26.7
Jet·miss $E_T$	113 · 70	4.5	30.4
Electron·Jet	25 · 52	1.3	31.7
Muon·Jet	15 · 40	0.8	32.5
Minimum-bias		1.0	33.5

Table 2.3: *Level 1 trigger Table at high luminosity.*

an analysis whose complexity is similar to the one used during off-line reconstruction, and it has to have access the full information content available in the event.

This computational complexity, together with the request to achieve max-

imum flexibility, brought to the decision to perform HLT reconstruction on a farm of commercial processors running the same software framework used for offline analysis. This will also allow to easily migrate offline algorithm refinement to the online realm, simplifying the procedure of improving the HLT system with time and experience.

The HLT is only a part of the whole CMS DAQ system, whose architecture is schematically shown in Fig. 2.16. Data coming from the detector is initially stored inside 40 MHz pipelined buffers by the Front End System (FES). Upon arrival of an L1A signal from the L1T, data is moved by the Front End Drivers (FEDs) to the Front End Readout Links (FRLs) which are able to store informations coming from up to two FEDs. A total number of 626 FEDs and 458 FRLs is used to manage data coming from the different subdetectors and their trigger subsystems.

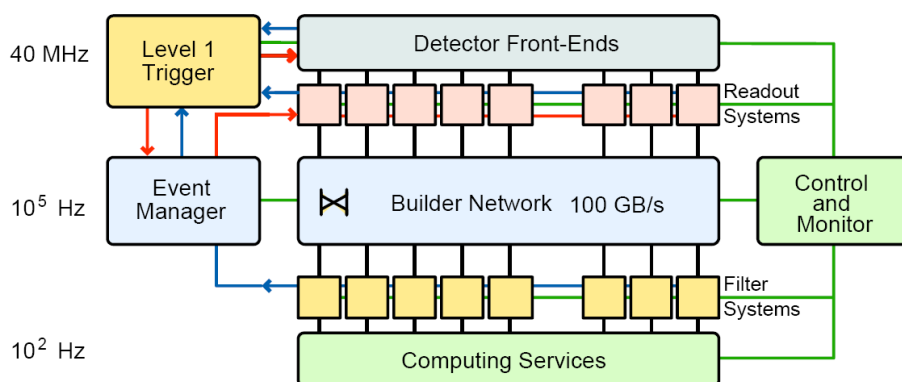


Figure 2.16: *Schematic architecture of CMS DAQ system.*

Event fragments coming from different FRLs are then sent to the *Event Builder* system in charge to build up the full event. The latter is implemented in two different stages, referred as FED-builder and RU-builder. The first one is burden to transport data from underground to the CMS surface buildings, where the rest of the farm is located, and perform a first assembly phase. The FED-builder output consists of 72 super-fragments that are then stored in large Readout Units (RU) buffers waiting for the final building phase to be performed by the RU-builders. This two level architecture allows to deploy the system in up to 8 separated *DAQ slices*, each of them nearly independent

from the others and able to handle a  $12.5\text{ kHz}$  event rate.

After the assembly phase is completed, the event is sent to the *Event Filter* where HLT algorithms, together with some Data Quality Monitoring operations, are performed. Here the Filter Unit Resource Broker (FU-RB) takes care of sending the data coming from the Event Builder to the Filter Unit Event Processor (FU-EP) in charge to perform the HLT processing. As already mentioned, the FU-EP uses the CMS reconstruction software framework for HLT and Data Quality Monitoring purposes. Filtered data are then separated into several online streams, whose content depend on trigger configuration, and are sent to a local storage system before being migrated to the CERN mass storage infrastructure.

During the LHC low luminosity phase, where a data acquisition rate of  $50\text{ kHz}$  is foreseen to be sufficient, only 4 DAQ slices will be installed. Complete deployment will be operated before the high luminosity phase taking advantage from development of commercial computing components.

## Chapter 3

# The Drift Tubes System and Trigger Electronics

Many interesting physical processes foreseen at the LHC will be characterized by final states containing high  $p_T$  muons. Therefore a muon spectrometer able to perform precise measurements is needed, in order to operate effective standalone track reconstruction. Moreover, due to the high interaction rate, an high-performance level-1 muon trigger system, able to operate fast identification of the interesting events, is required. In the CMS outer barrel region, where residual magnetic field and particle flux are low, a *drift tubes* based system is used to accomplish high resolution positional measurement and provide efficient trigger capabilities.

### 3.1 The Drift Tubes System

A *Drift Tubes* (DT) based detection system is installed in the barrel region of the CMS muon spectrometer [28, 31, 22]. The use of DTs allows to achieve good spatial resolution and cover large surfaces in a  $\eta$  region where both residual magnetic field and neutron-induced background, are small.

As shown in Fig. 2.10, the DT layout consists of four concentric cylinders of *stations* positioned almost symmetrically around the beam line, segmented in 12 *sectors* covering an azimuthal region of  $\sim 30^\circ$  each. This arrangement is replicated along the 5 *wheels* that compose the whole barrel.

The iron supports positioned between the chambers of the three inner stations generate unavoidable dead zones in the  $\phi$ -view. Therefore detecting

planes are staggered in that view to increase the system coverage. For the same reason MB4 *stations* are disposed in a slightly asymmetrical layout: chambers of different size are used and top and bottom sectors are equipped with two detecting chambers (usually called “*double stations*”). They are taken into account separately during local track reconstruction but they are, instead, grouped together by the Local Trigger Sector Collector (3.2.4) and considered as a single station by the Track Finder Regional Trigger subsystem (3.3.1). Sometimes another logical subdivision of the DT chamber is used, it is called *wedge* and consist of the group of sectors, belonging to all the 5 wheels, located in the same  $\phi$ -region. Every *wedge* is composed of 20 chambers, with the exception of top-most and bottom-most ones whose consist of 25 chambers each, for a total amount of 250 DT chambers in the whole CMS detector.

### 3.1.1 The Drift Chamber

The basic unit where local reconstruction and Local Trigger algorithms are performed within the DT system is the *chamber*.

DT chambers are variable in size, their dimensions being dictated by constraints coming from wheel and sector segmentation. One single chamber is composed by multiple layers of drift *cells* of  $4.2 \times 1.3 \text{ cm}^2$  transversal section, arranged to measure position in the  $\phi$ -view and along the  $z$  axis. The single cell size is small enough to guarantee negligible occupancy and avoid the use of multi hit electronics systems, and, on the opposite, it is large enough to limit the total number of active channels to an affordable value.

A schematic layout of a muon chamber is shown in Fig. 2.11. Cells are replicated in parallel rows called *layers*. Groups of four staggered layers form a single detection *superlayer* (SL). As explained in (3.1.2) three separate layers are enough to allow segment identification within a SL, however a fourth layer guarantees redundancy and robustness to reconstruction algorithms an to the local trigger system.

Muon chambers of the MB1/2/3 stations are composed of three SLs, two of them devoted to the measurement of position in the  $(\phi-r)$  plane, the other being used to measure the  $z$  coordinate. Redundant detection of the  $\phi$ -view position is needed to efficiently measure curved track trajectory in the azimuthal plane, in order to operate precise  $p_T$  reconstruction. The trajectory in the  $\eta$ -view, instead, is supposed to be a straight line (apart

from multiple scattering), therefore a single layer of detection is enough to achieve the requested precision along  $z$ . Moreover for economical reasons MB4 stations are not equipped with a  $\eta$ -view SL and consist only of the two  $\phi$  SLs.

In order to fully exploit the precision of single cell measurements, the position of the wires within a chamber must be known with good accuracy. Therefore a rigid mechanical structure is needed to avoid significant chamber deformations. Rigidity is provided by the outer chamber planes and by an aluminium honeycomb plate that separates the outer SLs from the inner one. This structure provides a light support to the SLs and allow to increase the level-arm between the two  $\phi$  detection planes, improving angular resolution within a station. Some technical parameter describing the structure of the various types of DT chambers are shown in table 3.1.

The goal of the mechanical construction of a chamber is to achieve a local reconstruction resolution of  $100\ \mu\text{m}$  in the  $(r-\phi)$  plane measurement, making the precision of MB1 chambers comparable with the uncertainties coming from multiple scattering at a muon  $p_T$  of  $200\ \text{GeV}/c$ . This requirement is fulfilled in the case of a 8-point reconstructed track for a single cell resolution of  $250\ \mu\text{m}$  (see 3.1.2).

### 3.1.2 The Drift Cell

The DT *cell* detects the ionization electrons produced by the passage of particle crossing an  $\text{Ar}/\text{CO}_2$  gas mixture. Their drift time in the electric field is measured to get the distance of the ionizing particle from the wire.

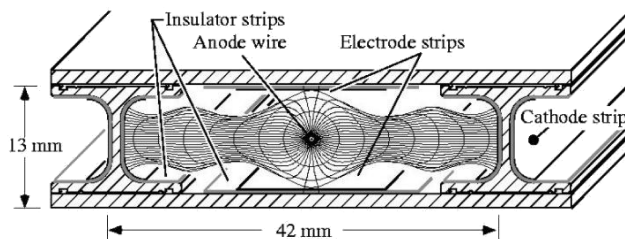


Figure 3.1: Schematic view of a drift tube cell.

THE DRIFT TUBES SYSTEM AND TRIGGER ELECTRONICS

Chamber type	N of ch	N. of $SL\phi$	N. of $SL\theta$	N. of ch $SL\phi$	N. of ch $SL\theta$	Wire Length $\phi$ (mm)	Wire Length $\theta$ (mm)	Sum of ch
MB/W/1/S	58	2	1	196	228	2379	2038	35960
MB/1/1/4	1	2	1	196	190	1989	2038	582
MB/-1/1/3	1	2	1	196	190	1989	2038	582
MB/W/2/S	58	2	1	238	228	2379	2051	40832
MB/1/2/4	1	2	1	238	190	1989	2051	666
MB/-1/2/3	1	2	1	238	190	1989	2051	666
MB/W/3/S	58	2	1	286	228	2379	3021	46400
MB/1/3/4	1	2	1	286	190	1989	3021	762
MB/-1/3/3	1	2	1	286	190	1989	3021	762
MB/W/4/S	29	2	0	382	0	2379	0	22156
MB/-1/4/3	1	2	0	382	0	1989	0	764
MB/W/4/4	8	2	0	286	0	2379	0	4576
MB/1/4/4	2	2	0	286	0	1989	0	1144
MB/W/4/8,12	10	2	0	372	0	2379	0	7440
MB/W/4/9,11	10	2	0	190	0	2379	0	3800
MB/W/4/10	10	2	0	238	0	2379	0	4760
Total	250							171852

Table 3.1: *Characteristic of the DT system chambers. W stands for all wheels and S for all sectors (with exception of the explicitly mentioned ones).  $SL\phi/\theta$  measures position in the  $(r - \phi)$  and  $(r - z)$  planes respectively.*

A schematic layout of a single drift cell is given in Fig. 3.1. The cell has a size of  $4.2 \times 1.3 \text{ cm}^2$  and a  $50\text{-}\mu\text{m}$  diameter, gold-plated, stainless-steel wire is located at its center. A field electrode, made of a  $16 \text{ mm}$  wide aluminium tape, is insulated from the aluminium top and bottom plates by a  $23 \text{ mm}$  wide mylar strip. Cathodes, made of  $11.5 \text{ mm}$  wide aluminium tape, are placed on both sides of the I-beams used to separate different cells within the same layer; their insulation is achieved with the same technique used for field electrodes. Both the top/bottom plates and the I-beams are grounded while wires, electrodes and cathodes are kept at operational voltages around  $+3600 \text{ V}$ ,  $+1800 \text{ V}$  and  $-1200 \text{ V}$  respectively. The gas is a  $85\%/15\% \text{ Ar}/\text{CO}_2$

mixture and provides good quenching properties as well as a saturated drift velocity of about  $55 \mu\text{m}/\text{ns}$ . The maximum drift time is therefore about  $380 \text{ ns}$  (corresponding to 15 BX). The I-beam and planes thickness is enough to guarantee decoupling of the signal from different cells with respect to noise coming from low-energy electrons. This ensures that the system multi-layered redundant structure is able to perform reliable background suppression as noise detected in different cells is almost uncorrelated.

### Cell Working Principle

A minimum ionizing particle crossing a cell generates, on average, about 30 ionization electrons per cm. Once they have been produced, the electric field generated by wire, electrodes (kept at a positive potential), and cathodes (kept at negative potential) induces their drift in the direction of the anode wire. Here the ionization electrons are collected, and the electric field (increasing as  $1/r$  in the region) is strong enough to induce secondary ionization, hence, avalanche discharge. A gain factor of about  $10^5$ - $10^6$  is thus achieved. The  $\text{CO}_2$  in the gas mixture acts as a quencher, absorbing most of the photons produced during the discharge, keeping the avalanche region limited. The produced signal is then collected by the wire, it is amplified and discriminated against a configurable threshold, and it is sent to the read-out system for TDC measurement.

The distance  $x$  of the track from the anode wire can be obtained by the:

$$x = \int_{t_p}^{t_w} v_d \cdot dt \quad (3.1)$$

where  $t_p$  and  $t_w$  are, respectively the particle time of passage and the time when the signal is collected from the wire. Actually the local trigger algorithm, as well as some reconstruction models, are based on methods that require a constant drift velocity ( $v_d$ ) within the cell. In these conditions the aforementioned relation becomes:

$$x = (t_w - t_p) \cdot v_d. \quad (3.2)$$

It is therefore important to ensure the stability of  $v_d$  along the cell, thus the use of electrode strips in top and bottom plates to guarantee the presence of a field that allow linear space-time relationship. A computation of the field's equipotential lines is shown in Fig. 3.2 (right).

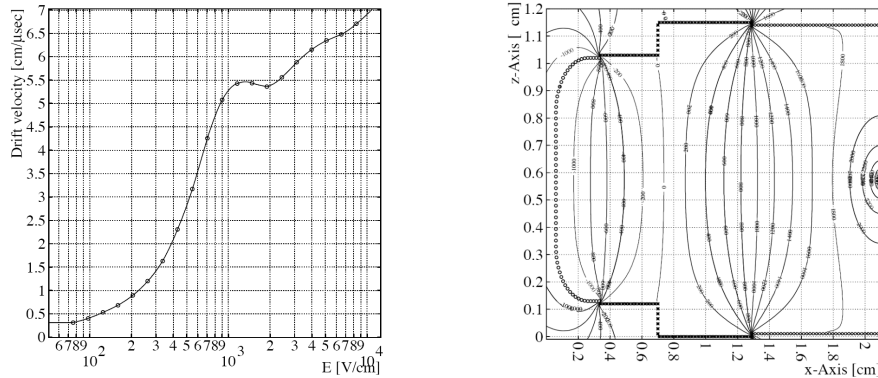


Figure 3.2: *GARFIELD* [33] calculated values of  $v_d$  as a function of the electric field at atmospheric pressure (left). Equipotential lines computation for half of a drift cell; anode is on the right side (right).

One of the major factors that can influence  $v_d$  is the ratio between the electric field and the atmospheric pressure  $E/p$ . To limit fluctuations due to these factors the DT working point is chosen in order ensure saturated drift velocity. As shown in Fig. 3.2 (left), at atmospheric pressure  $v_d$  saturates at about  $E = 1.9 \text{ kV/cm}$ , therefore the cell is designed to avoid regions where the field is lower than this value, reducing the sensitivity to local fluctuations.

Gas composition and temperature may also affect the drift behavior, thus they are continuously monitored. As an example the oxygen concentration has to be always kept below 500 ppm.

Furthermore track inclination with respect to the direction orthogonal to the chamber affects the time-distance relation. This happens because electrons having the shortest drift time are not the ones produced in the mid plane of the cell, and causes the apparent drift velocity to result higher.

Finally the presence of an external magnetic field can affect the drift path of charged particles. In fact the Lorentz force applied to moving electrons modifies the particle's trajectory to a curved line, reducing the effective value of  $v_d$ . An homogeneous magnetic field parallel to the wire direction has the effect to rotate the effective drifting field, as shown in Fig. 3.3. Moreover inhomogeneities in the magnetic field and the presence of a radial field component, shown in Fig. 3.4, further complicate the situation especially in the  $\phi$  detecting view.

### 3.1 — The Drift Tubes System

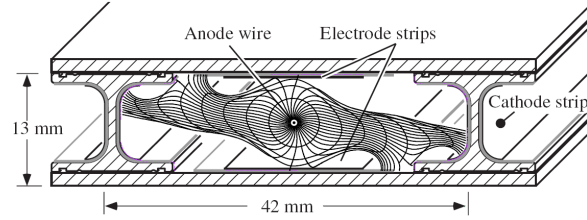


Figure 3.3: *Simulation of the distortion produced in the drift lines by a 0.5 T magnetic field parallel to the wire.*

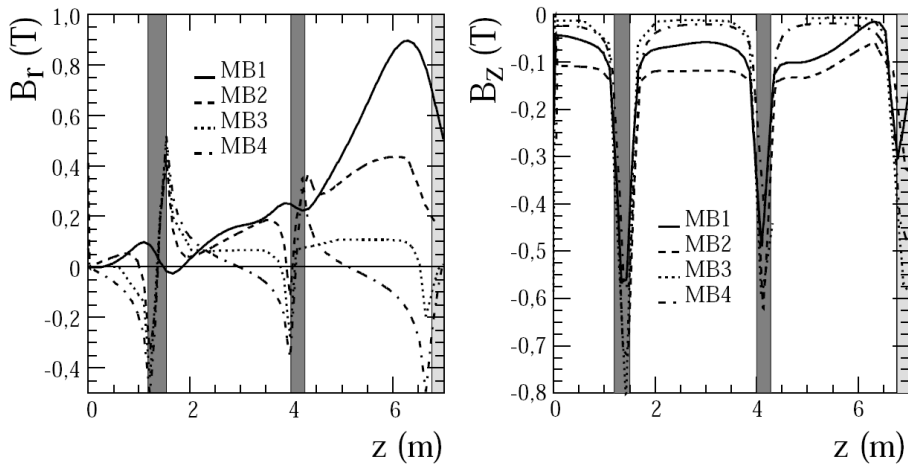


Figure 3.4: *Radial (left) and longitudinal (right) components of the magnetic field in the regions where DT stations are placed as a function of  $z$ . Vertical bars indicates the separation between wheels.*

The single DT cell is characterized by a detection efficiency higher than 98% and a spatial resolution around  $180 \mu m$ . More in-depth results coming from test-beam analysis and from chamber commissioning are presented in the next sections after a brief description of the mean-timer technique.

### The Mean-Timer Technique

The generalized *mean-timer* technique used within the CMS DT system allows to identify particle tracks giving signal in at least 3 of the 4 layers of a single SL and it is used both for triggering [34] and analysis purposes (see 3.1.2 3.2.1). The technique relies on the fact that, under precise conditions, the maximum allowed drift time (i.e. the time needed to drift across half of the cell) is a constant that put a precise constraint on the sum of the single drift times found within the interested cells. More in detail it is independent from both the impact position ( $d$ ) and direction ( $\Psi$ ).

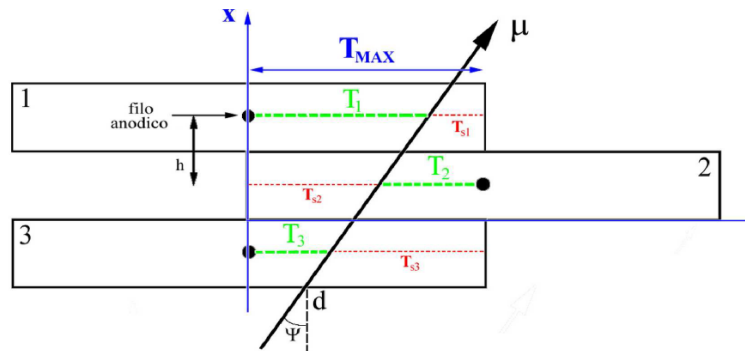


Figure 3.5: Graphical scheme of the mean-timer computation.

A graphical scheme describing the key elements involved in the mean-timer computations is shown in Fig. 3.5. Requiring the assumptions of:

- Straight trajectory of the particle within the detecting SL;
- Constant distance among the wire planes:
- Constant  $v_d$  of the electrons within the cells

one can show that the following relations hold:

$$\begin{cases} T_d(1) = d + \frac{5}{2}h\tan\Psi \\ T_d(2) = T_{MAX} - d - \frac{3}{2}h\tan\Psi \\ T_d(3) = d + \frac{1}{2}h\tan\Psi \end{cases} \quad (3.3)$$

where  $h$  is the spacing between wires,  $T_d(i)$  is the drift time of the  $i$ -th cell and  $T_{MAX}$  is the maximum drift time allowed within the cell. Solving equation (3.3) one obtains:

$$T_{MAX} = \frac{(T_d(1) + T_d(3))}{2} + T_d(2) \quad (3.4)$$

therefore  $T_{MAX}$  computation is independent from  $d$  and  $\Psi$  and it is constrained by the cell geometry and the constant  $v_d$  assumption. As we will see in the next sections this allow, among other things, to estimate single cell resolution 3.1.2 and develop a fast trigger algorithm able to perform position and direction measurement, as well as BX identification 3.2.1.

## Performances

Several dedicated tests [22, 37] have been carried out to study the single cell/chamber performances under different conditions.

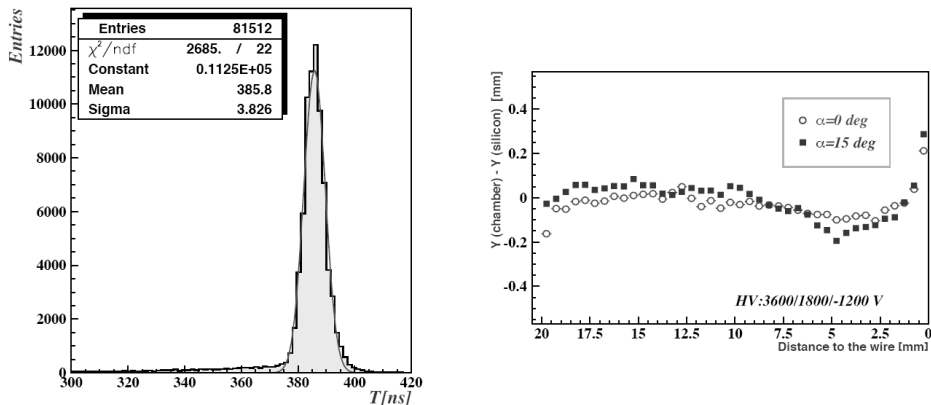


Figure 3.6: *The mean-timer distribution allows to estimate position resolution (left). Deviation from linearity as a function of the distance from the wire at different angles of incidence (right).*

The spatial resolution can be measured using the  $T_{MAX}$  computation (3.4), as shown in Fig. 3.6 (left). Under linear drift assumption the time resolution  $\sigma_t$  is related to the RMS of this distribution by  $\sigma_t = \sqrt{2/3} \cdot \sigma_{T_{MAX}}$ , thus leading to a spatial resolution of  $170 \mu\text{m}$ . Saturation and stability of  $v_d$

can be gathered by the smoothness of the drift time distribution in the cell (usually referred as *time-box* for its peculiar shape) shown in Fig. 3.7 (left).

More thorough analysis on deviation from linearity have been performed using a Silicon Beam Telescope that allows to compute the differences between the reconstructed position and the one extrapolated from the drift cell measurement. Results for tracks coming at different impact angles are shown in Fig. 3.6. Deviations of the order of  $100 \mu m$  are expected (corresponding to a trigger jitter smaller than  $5 ns$ ).

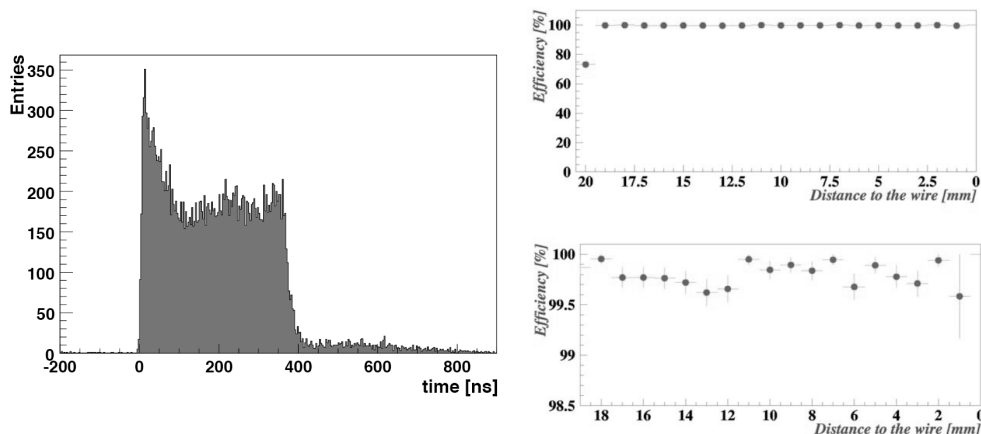


Figure 3.7: *Drift time distribution of a DT cell, usually referred as time-box (left). Efficiency as a function of the distance from the wire for tracks orthogonal to the chamber (right-top). Same plot with expanded scale (right-bottom).*

The same technique has also been applied to compute cell efficiency as a function of the distance from the wire. As shown in Fig. 3.7 (right), geometrical inefficiency coming from the I-beam is clearly visible, however the remaining part of the cell is characterized by efficiency values higher than 99.5%.

Finally effects coming from the presence of a magnetic field parallel to the wires have been investigated. Results are shown in Fig. 3.8 and a variation of  $v_d$  around 3% is expected going from a  $B = 0$  to 0.5 T. The spatial resolution is also deteriorated by low magnetic fields but it remains better than  $300 \mu m$  at 0.3 T, still allowing precise track segment reconstruction.

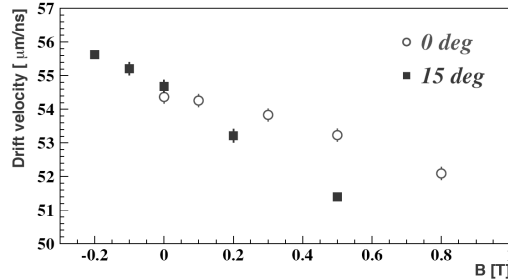


Figure 3.8:  $v_d$  as a function of the magnetic field for perpendicular ( $0^\circ$ ) and inclined ( $15^\circ$ ) tracks.

## 3.2 DT Local Trigger

The *DT Local Trigger* system [28, 29] (or *DT Trigger Primitive Generator* DT-TPG) goal is the detection of charged particles crossing the muon barrel chambers. Its working principle is based on the *mean-timer* technique previously described in (3.1.2) and it has to measure position and trajectory of the crossing particles, as well as to identify their origin in terms of BX. It also associates to the reconstructed segments a quality word based on the numbers of layers involved in the measurement and, finally, it sends the *trigger primitive* quantities to the DT Regional Trigger for further processing.

The DT Local Trigger is implemented using dedicated electronics located both on the single chambers and off-board, on the balconies surrounding the detector. The block scheme of the on-board system is outlined in Fig. 3.9. The signal coming from single wires is initially processed by *Bunch and Track identifiers (BTIs)* that operate rough track fitting within a single SL and perform BX assignment. In a second step the *Track Correlators (TRACOs)* are devoted to match the information coming from the two  $\phi$ -SLs and improve the parameter measurements. Then the *Trigger Server (TS)* performs a quality based selection on the segments coming from different TRACOs. Finally information from chambers of a single sector is forwarded, on the balconies surrounding the detector, to the *Sector Collector (SC)* that has to further refine the sorting, perform synchronization on data coming with different latencies, and send the signal to the DT Regional Trigger.

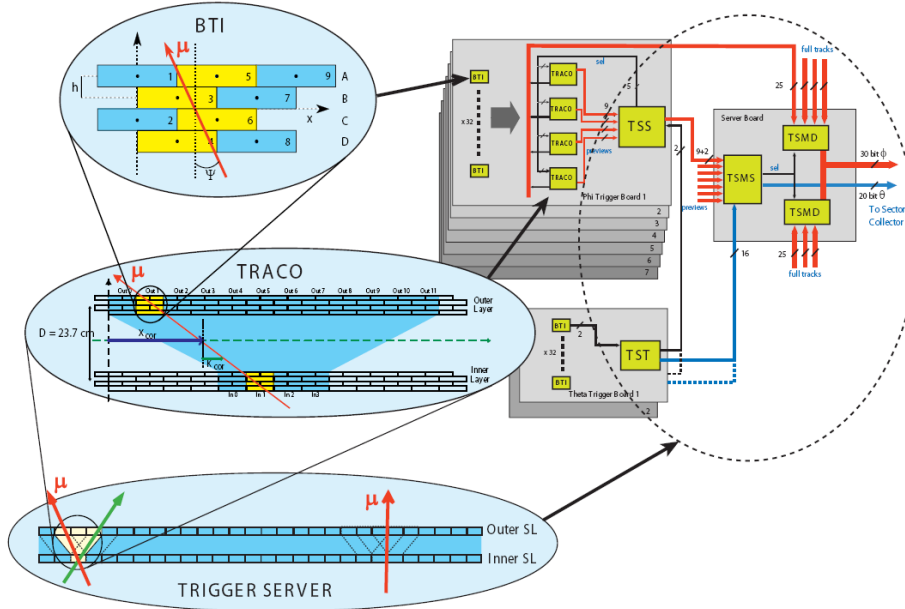


Figure 3.9: Schematic view of the on-board part of the DT Local Trigger system.

### 3.2.1 The Bunch and Track Identifier

The *Bunch and Track Identifier* [29] (BTI) is the DT trigger front-end device and has the task to associate a *track segment* to a charged particle crossing a SL, such segment contains information about the trajectory of the particle and its BX of origin. The track segment identification is performed by fitting the detected hits with a straight line, using the *mean-timer* method previously described in 3.1.2. A quality bit used to discriminate *Low* and *High* quality segments is also computed on the basis of the number of layers involved in the track identification. BTI computations are carried out in parallel using dedicated electronics located on the DT chamber board.

The geometric layout of a single BTI is shown in Fig. 3.10 (top). Each BTI is connected to 9 cells of a single SL and adjacent BTIs partially overlap (having 5 cells in common) in order to avoid geometrical inefficiencies. BTIs are identical in both the  $\phi$ -view and  $\theta$ -view SLs and the number of BTIs per SL only depends on the chamber size.

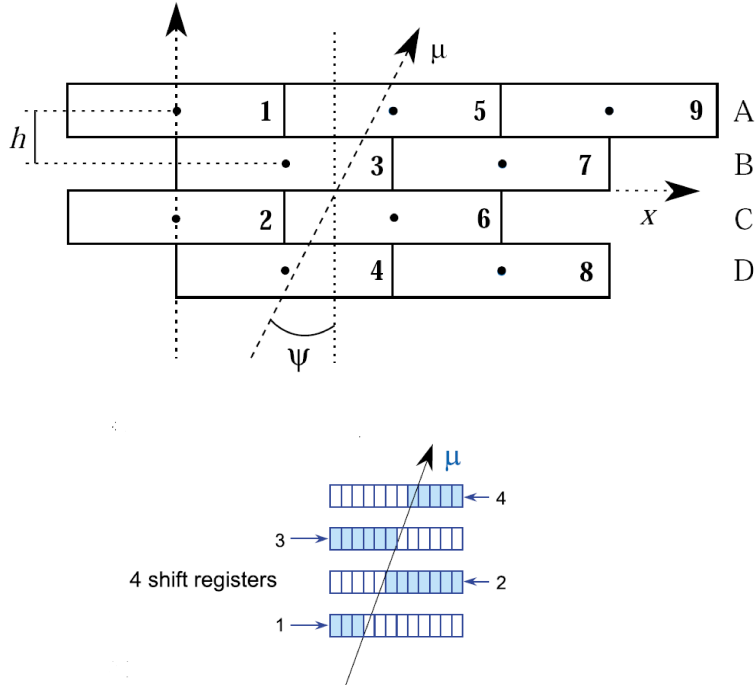


Figure 3.10: *Layout of a single BTI (top). Schematic view of the BTI shifting registers (bottom).*

### The BTI Algorithm

The BTI working principle is based on the mean-timer technique previously described in 3.1.2. For a particle crossing straight a group of cells characterized by constant  $v_d$ , it is in fact possible to compute the track segment position and direction using the measured hits arrival time.

After the particle's passage a signal is induced on the detecting wire  $i$  at a time  $T_d(i)$  that depends on both  $v_d$  and the distance between the particle trajectory and the wire (as in Fig. 3.5). The signal is sent to the BTI connected to the wire that inserts it into a register that counts the time  $T_S(i)$  elapsed after the hit in the  $i$ -th cell was produced at a 80 MHz frequency (twice the design bunch crossing frequency), as shown in Fig. 3.10 (bottom). On every BTI clock count, the apparent  $T_d(i) = T_{MAX} - T_S(i)$  is computed, and a straight line reconstruction is performed using signals coming from

different pairs of layers (AB, AC, AC, BC, BD, CD of Fig. 3.5). Apparent track position and apparent  $k = h \tan(\Psi)$  parameter, related to track direction, are then evaluated for every pair. Indeed apparent values correspond to real ones only at a fixed latency  $T_{MAX}$  after the particle passage. In this case the  $k$  parameters coming from computations performed on different pairs of layers match and allow to perform track identification. Moreover since  $T_{MAX}$  is independent from both position and direction of the crossing particle, it is possible to perform precise parent BX assignment.

Three aligned points are sufficient to reconstruct a track segment but the presence of a fourth layer improve the system redundancy and robustness. In fact it allows the algorithm to work even in case a hit is missing (due to detection inefficiency) or is wrong (e.g. in case of noise generated by the emission of a  $\delta$ -ray). Furthermore on the basis of this redundancy is also possible to perform quality classification on the BTI's track segments. An *High quality trigger* (H-trigger) is thus obtained if four aligned hits have been matched in as many layers, instead a *Low quality trigger* (L-trigger) is found if the matching was possible only among three of the four layers.

Such quality conditions limit the maximal angular acceptance of the BTI to  $\pm 45.7^\circ$  for H-triggers and  $\pm 56^\circ$  for L-trigger ensuring good BTI performances in an angular region up to  $45^\circ$  (enough to guarantee good reconstruction of muons in a wide  $p_T$  range at LHC conditions). In the  $\theta$  view, where track are not bent by the magnetic field, the BTI acceptance window is manually configured to point to the center of the detector<sup>1</sup>.

The minimal request of alignment of any three hits to obtain a L-trigger yields to a significant rate of false trigger segments. In fact the alignment of four hits at one clock-step may produce three hits alignment at the step before or after an H-trigger signal, generating a so called *ghost trigger*. In order to achieve noise reduction, a *Low Trigger Suppression* algorithm (LTS) is applied within the BTI logic. Cancellation of L-triggers in a  $[-1,+8]$  BX range around an H-trigger has been found to be an effective solution to the problem [29].

The position and direction resolutions obtained at BTI level depend on the drift velocity and (in absence of magnetic field and for the nominal gas mixture composition) are expected to be respectively  $1.25 \text{ mm}$  and  $60 \text{ mrad}$ . The time needed by the BTI for its computation is 4 BX. Taking into account

---

<sup>1</sup> During the detector commissioning phase, however,  $\theta$  BTI acceptance was set to its maximum value to allow proper cosmic rays detection.

the approximate value of  $T_{MAX}$  ( $\simeq 400 \text{ ns} = 16 \text{ BX}$ ) and signal propagation through the front end links (2 BX), it results that the total BTI latency is of 22 BX (550 ns) at nominal conditions.

### 3.2.2 The Track Correlator

The *Track Correlator* [40] (TRACO) is the second element of the DT Local Trigger chain and it is devoted to the association, within a muon chamber, of the track segments delivered by predefined groups of BTIs belonging to the two  $\phi$ -superlayers. It attempts correlation between BTI segments coming from inner and outer SLs and links the information between the two, improving track parameters determination. Each TRACO can then send up to two *candidates* to the Trigger Server for further processing. As in the BTI case TRACO operations are carried out using custom made on-board electronics.

The schematic layout of a TRACO is shown in Fig. 3.11. Each TRACO is connected to 4 BTIs in the inner SL and 12 BTI in the outer SL and adjacent TRACOs overlaps only in the outer SL. The number of BTIs connected to a single TRACO is determined by the acceptance requirements to match the H-triggers BTI angular coverage 3.2.1. Within a single TRACO, correlation is attempted only on outer track segments pointing to the inner BTIs.

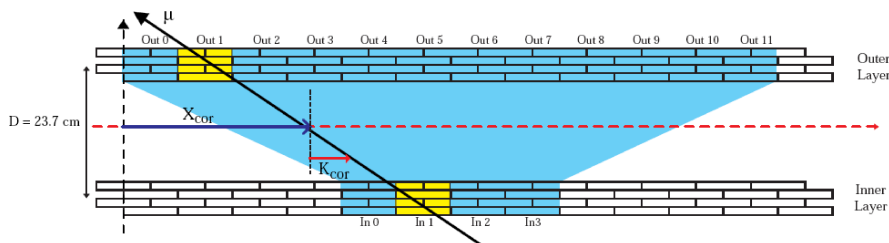


Figure 3.11: *Schematic view of the TRACO layout.*

The total number of TRACOs per chamber depends on the size of the station (from 12 to 24 TRACOs per chamber are needed). In the  $\theta$ -view there is just one single detecting SL per station, thus no TRACO operation is performed on  $\theta$  BTIs (their information is forwarded directly to the Trigger Server).

### The TRACO Algorithm

A block diagram showing the TRACO algorithm and segmentation in term of BXs is shown in Fig. 3.12. A brief discussion of the key point of each single step is carried out in the following.

**1st BX** The output of the 16 BTIs connected to a single TRACO is received by an *Input Register*. Such data contains information on the quality of the track segment as well as its position and direction in BTI units. A module named *Angle Converter* translates the BTIs  $k$  parameters to local radial TRACO coordinates, taking into account the geographical position of the interested correlator, and send its output to further processing units as well as to the Trigger Server preview bus.

**2nd BX** Each BTI position is converted to a TRACO position by the *Position Converter*. Simultaneously a *Track Sorter* module performs a ranking, on the track segments coming from inner and outer SLs separately, on the basis of their quality and direction. Segments whose direction is close to the local radial direction are favored because they refer to high  $p_T$  particles. Sorting priorities are programmable, the highest priority being given to the track quality in the default configuration. This allows to select tracks with good quality and high  $p_T$ .

**3rd BX** A module named *Calculator and Comparator* computes TRACO position and direction for the correlated candidate using the:

$$\begin{cases} k_{corr} = D \tan \phi = x_{inner} - x_{outer} \\ x_{corr} = (x_{inner} + x_{outer})/2 \end{cases} \quad (3.5)$$

where  $D$  is the distance between the two SLs, whereas  $x_{corr}$  and  $k_{corr}$  represent the correlated track parameters as indicated in Fig. 3.11. The correlated direction  $k_{corr}$  is then compared with the direction information coming from single BTIs (previously converted at the processing step labelled as *1st BX*). Matching is then performed if compatibility, within a programmable tolerance, is found. Then a *Priority Selector* module chooses how to propagate track information among three possible cases: *i*) correlation is found and updated track parameters are forwarded; *ii*) no correlation is found between two BTI segments, then a single *uncorrelated* track is forwarded on the basis of a programmable

3.2 — DT Local Trigger

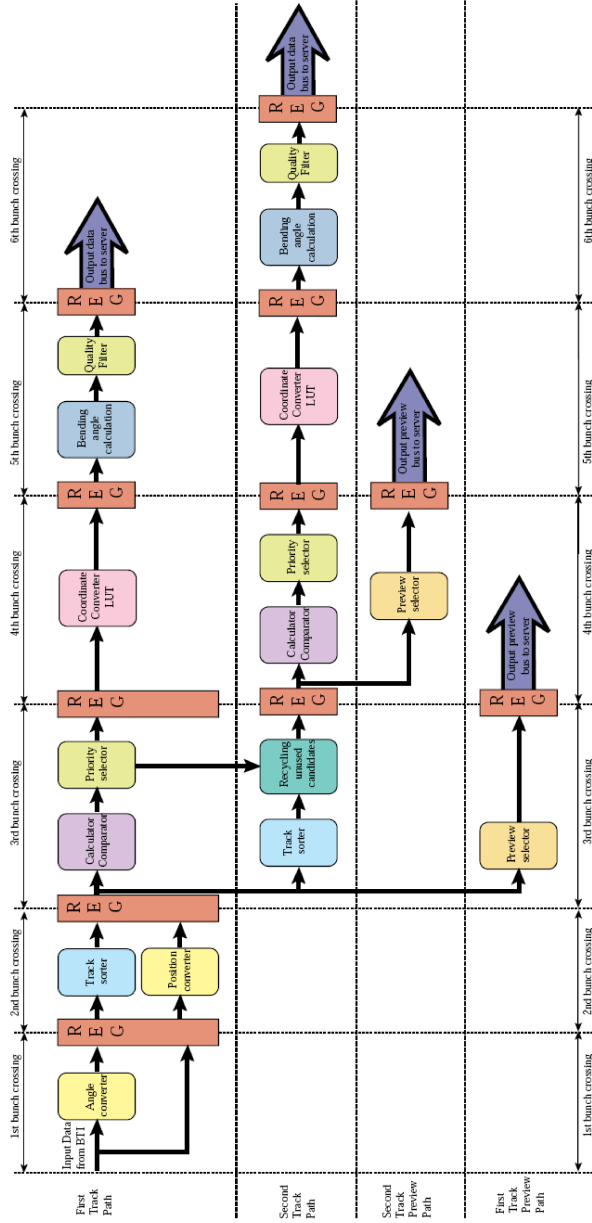


Figure 3.12: Schematic view of the TRACO algorithm.

selection which takes into account the segment qualities (H/L) and the parent SL position (inner/outer); *iii*) no correlation is found because only a segment coming from one SL is present, then an uncorrelated trigger is forwarded. Uncorrelated triggers may be suppressed (on the basis of a programmable parameter) if they are not confirmed by the presence of an independent BTI segment in the  $\theta$  SL depending on the noise and data taking conditions. The output candidate is finally propagated and its quality word is computed according to table 3.2.

**4th BX** A *Coordinate Converter* module performs the conversion between the TRACO inner coordinates to deliver chamber radial angle  $\Phi$  and total angle  $\Psi$  information as defined as in Fig. 3.13 on the basis of programmable LookUp-Tables (LUTs).

**5th BX** A *Bending Angle Calculator* module compute the bending angle  $\Phi_b = \Psi - \Phi$  and a *Quality Filter* module eventually operates uncorrelated L Trigger suppression on the basis of programmable parameters.

**6th BX** The output data bus delivers the track information to the Trigger Server.

TRACO code	Quality label	meaning
6	HH	Correlated H+H trigger
5	HL	Correlated H+L or L+H trigger
5	LL	Correlated L+L trigger
4	HO	Uncorrelated H Trigger (outer SL)
3	HI	Uncorrelated H Trigger (inner SL)
2	LO	Uncorrelated L Trigger (outer SL)
1	LI	Uncorrelated L Trigger (inner SL)
7	/	Null track

Table 3.2: *Conventional coding for the TRACO quality word.*

Actually the TRACO algorithm is more complicated than the one just described. In fact, in order to allow identification of two muons traversing the chamber with close trajectories, a *second track* selection is performed on the basis of the candidates that were not used to compute the so-called *first track*.

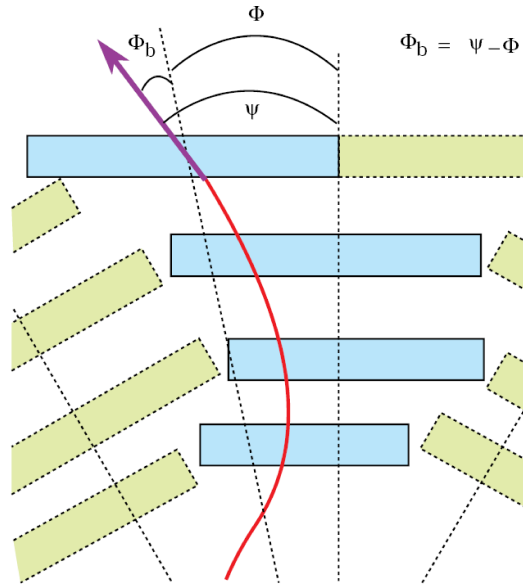


Figure 3.13: *Trigger primitives angular parameters definition.*

The second track is delivered one BX later with respect to the first one and it can be suppressed when *pile-up* triggers are present (i.e. when two triggers are delivered by the same BTI in consecutive BXs). Moreover independent flows generating *track previews*, used to help Trigger Server selection are delivered in advance with respect to the full TRACO information reducing the total trigger latency. Thus the TRACO has actually to manage 4 parallel data flows, 2 related track calculation and two related preview transmission.

The TRACO position resolution is unchanged with respect to the one obtained by BTIs ( $\simeq 1\text{ mm}$ ), whereas the long level arm between the two SLs allows to enhance angular resolution for correlated tracks to about  $\Delta\Phi_b \simeq 10\text{ mrad}$ . Uncorrelated track segments are characterized by the BTI angular resolution ( $\simeq 60\text{ mrad}$ ).

The total TRACO latency is of 5 clock cycles for the first track and 6 cycles for the second track. As explained later (3.2.3), however, the total latency of the TRACO-Trigger Server chain is strongly reduced taking advantage of the preview mechanism.

### 3.2.3 The Trigger Server

The *Trigger Server* (TS) is the last on-board component of the DT Local Trigger logic and has to select the two best trigger candidates (in terms of quality and  $p_T$ ) among the track segments selected by all the TRACOs of a muon chamber. It also performs ghost track reduction on the fake tracks generated by adjacent TRACOs on the basis of configurable rejection algorithms.

Each muon station is equipped with only one TS, therefore the subsystem design is driven by requests of high robustness and redundancy. Moreover TSs have to be deployed on chambers of different dimensions but have to operate at fixed latency. In order to fulfill these requirements (keeping at the same time the number of logic cells as low as possible) the TS part operating the  $\phi$ -view ( $TS\phi$ ) is implemented in a two level structure, as outlined in Fig. 3.14.  $TS\phi$  main component are the *Track Sorter Slave* [41] (TSS) and the *Track Sorter Master* (TSM). Each TSS processes up to 4 data word per BX coming from as many TRACOs; then the informations coming from up to 7 TSS are sent to the TSM for final processing. The  $\theta$ -view of the TS ( $TS\theta$ ) is equipped with two identical units (TSTs). These have the task to group together data coming from up to 8 BTIs, performing a logical OR operation on the information received, to prepare  $\theta$ -view trigger data for regional processing. The  $TS\theta$  has also to forward theta BTI information to the TRACOs, as such quantities are needed to perform the programmable uncorrelated trigger suppression previously described in (3.2.2).

The TS system takes 6 clock cycles to perform its sorting operations (on both first and second tracks) but taking advantage of the preview mechanism the total TRACO-TS latency is reduced to 7 BXs.

The on-board trigger system is physically partitioned in several *Trigger Boards* (different in  $\phi$  and  $\theta$  views) and a *Server Board* located on the chambers minicrate electronics. The  $\phi$ -view trigger boards are equipped with 32 BTI chips, 4 TRACO chips and one single TSS chip; up to 7 of them can be present in a single chamber. The  $\theta$ -view trigger boards does not contain any TRACO chips and the two TST devices are mounted on separate boards. Finally the server board hosts the chamber TSM.

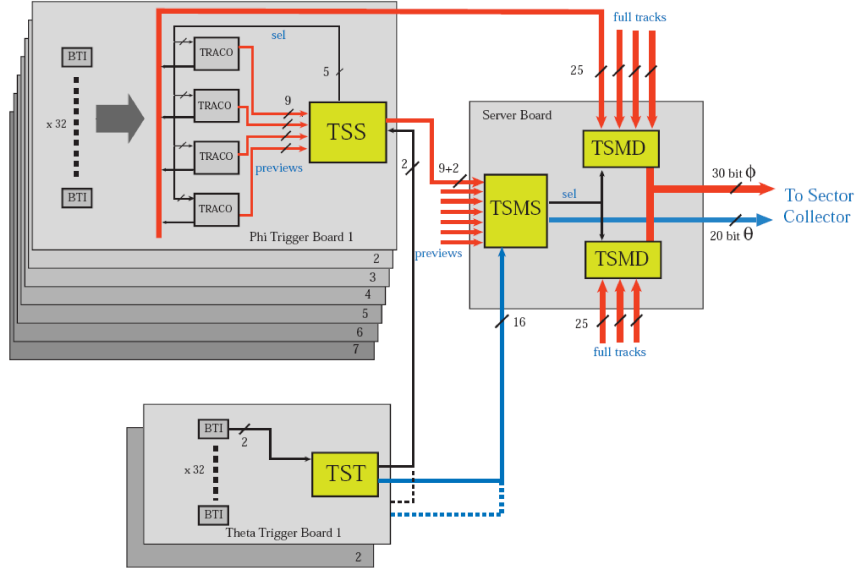


Figure 3.14: Schematic layout of the Trigger Server architecture.

### The $TS_\phi$ Algorithm

Similar sorting operations are performed in the TSS and TSM components of the  $TS_\phi$ . Let's define *bunch1* and *bunch2* respectively as the first and second BX where track candidates from a TRACO are delivered. The  $TS_\phi$  ranking logic operates a sorting on the data coming from different TRACOs at bunch1 selecting the first best track and a second best track (named *carry*). A second sorting is then performed taking into account the carry and data coming from bunch2. This allows to properly handle the passage of multiple muons in the station since the second track sorting is, in practice, carried out on the basis of information coming from both bunch1 and bunch2, ensuring a correct selection of the second best track. In case of *pile-up* triggers the  $TS_\phi$  can still provide the first best track; moreover a second best track coming from a different TRACO can still be delivered through the use of the carry.

### The Track Sorter Slave (TSS)

Each TSS is connected to 4 TRACOs and its main task is to operate the sorting of the preview data coming from them and, if possible, perform ghost track suppression. The preview track in input to the TSS is essentially a 9-bits word where 4 bits are used to describe the quality (*1st/2nd track, H/L/-trigger, Correlation bit, Inner/Outer SL*) and the remaining 5 are used for the bending angle (the bit sign being excluded). The TSS performs minimum and next-to-minimum searches on the preview words using 2-by-2 fast 9 bit comparators, on the basis of programmable priorities of the quality bits. It is also called to perform ghost suppression where possible, taking into account potential duplication of uncorrelated track segment coming from the inner and outer SLs of one single TRACO, or from the outer SL of two adjacent ones. Different noise reduction algorithms can be applied changing programmable configuration parameters. Data is then send to the TSM for further processing.

### The Track Sorter Master (TSM)

Every DT muon chamber is equipped with one single TSM that receives information from up to 7 TSS. It performs sorting operations similar to the one carried out in the TSS but its processing begins two BXs later and it doesn't have to operate ghost suppression on data coming from the same TRACO. The communication scheme between TRACO and TSM allows to store up to 12 tracks in a TSM unit. The signal coming from the sorting and corresponding to the first and second best tracks are used to enable full track candidate transmission to the Sector Collector in consecutive processing cycles.

In order to match robustness requirements, the system is segmented in different blocks with partly redundant functionality. As can be seen from Fig. 3.14, one *TSM Sorter* (TSMS) and two *TSM Data* (TSMD) block are present in each TSM. The TSMS takes care of the ranking of preview tracks coming from the various TSS, while the two TSMD are data multiplexing units that receive full TRACO information and forward them for further processing on the basis of the TSMS decision.

The design decision to use two TSMD blocks has been taken in order to ensure system robustness. In fact each of them takes care of a single half of a chamber, therefore in case of failures, partial information from half of

the station is still available. Moreover to cope with possible TSMS failures a *back-up* processing mode is foreseen. In this case each TSMD act as a sorter for the part of the system it is connected to, and is asked to deliver one single track output from its half of chamber every BX. This allows to guarantee full efficiency for single muon selection as well as for open di-muons crossing different halves of a DT chamber.

### 3.2.4 The Sector Collector

The *Sector Collector* [44] (SC) task is to collect track segments coming from one DT sector and forward them to the Regional Trigger system. It has to properly handle data coming from TSs configured in backup mode and performs further sorting on data coming from MB4 “double” (S4/13, S10/14) chambers.

It receives in input 80 bits words coming from MB1 and MB2 type stations: Each word include full  $\phi$ -segment information (*position, direction, quality and 1st/2nd track flag*),  $\theta$ -trigger position and quality and technical information such as BX count bits and parity bits among others. In order to handle synchronous transmission of two track segments coming TS $\phi$ s working in backup mode, the number of bits related to  $\phi$  view segment is actually doubled. A complete scheme showing the bit subdivision of the data transmitted by each station is shown in table 3.3.

In case of MB3 and MB4 chambers the amount of data transmitted to the SC is slightly different. In fact no  $\phi_b$  information is forwarded by MB3 stations because (due to the geometrical configuration of the B field) the track bending at this distance from the interaction point is almost constant in a wide range of  $p_{TS}$ , thus this information is not useful for Regional Trigger processing. Moreover the MB4 stations lacks of  $\theta$  SLs, therefore this kind of data is not included in this case; instead the presence of “double” detecting chambers should be handled.

The SC trigger electronics is located on the balconies around the detector. Therefore it has to compensate for the different transmission times of the on-board system signal due to differences in cable length and for the particles times of flight across the DT stations. Furthermore, due to the neutron flux expected in the experimental hall, the SC has been developed using radiation-hard components as in the case of the on-board trigger system.

data	Width (bits)	Type & comments
$\phi_r$ up $\phi$ track	12	signed,1-compl.
$\phi_b$ up $\phi$ track	10	signed,1-compl.
quality up $\phi$ track	3	see table 3.2
1 <sup>st</sup> /2 <sup>nd</sup> bit up track	1	
$\phi_r$ down $\phi$ track	12	signed,1-compl.
$\phi_b$ down $\phi$ track	10	signed,1-compl.
quality down $\phi$ track	3	see table 3.2
1 <sup>st</sup> /2 <sup>nd</sup> bit down track	1	
$\theta$ position	8	
$\theta$ quality	8	H/L for each position bit
Bunch Crossing 0	3	from up,down and $\theta$
Bunch Crossing count	2	2 LS bits of the bunch counter
$\phi$ parity bits	2	up and down
CCB info	4	Control Board status
Trigger output	1	chamber autotrigger

Table 3.3: *Data transmitted by each chamber to the SC. Up and down refers to the data coming from the two TSMD in backup mode.*

### 3.3 DT Regional Trigger

The DT Regional Trigger performs correlation between the track segment received by the SC boards in order to build full muon tracks. Figure 3.15 shows a block scheme of the system's architecture. Track segments are processed independently by the  $\phi$  and  $\eta$  components of the *DT Track Finder* (DTTF) system, named respectively *Phi Track Finder* (PHTF) and a *Eta Track Finder* (ETTF). Each PHTF process data coming from neighboring sectors, while the ETTF operates on data collected in a full wedge. Afterwards, best track candidates are selected by the *Muon Sorter* system that operates its ranking using a two level architecture. A first unit called *Wedge Sorter* performs the sorting on data coming from single wedges, then a *Barrel Sorter* module operates the final selection and send (up to) four candidates per BX to the Global Muon Trigger.

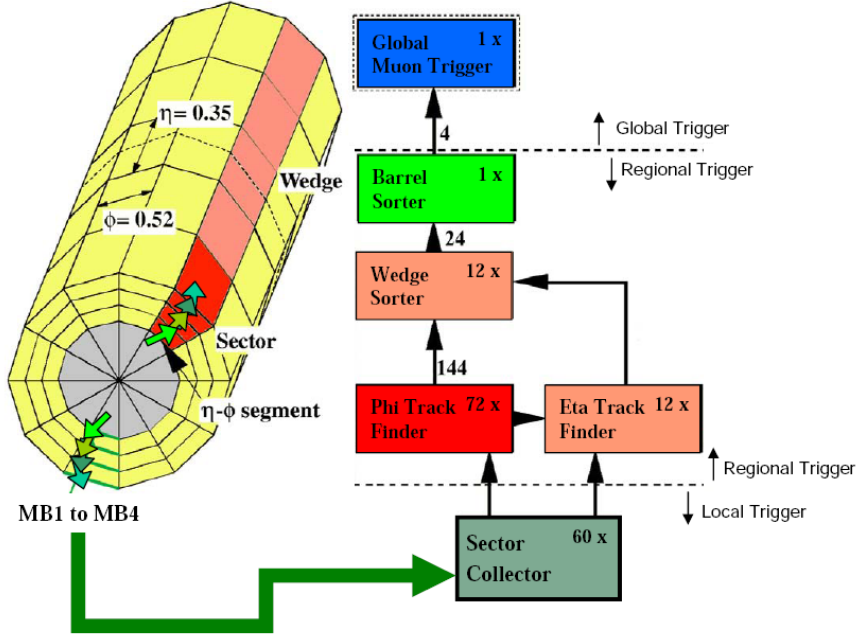


Figure 3.15: Schematic overview of the DT regional Trigger system.

### 3.3.1 The Phi Track Finder

The *Phi Track Finder* (PHTF) has the task to perform full muon track reconstruction in the CMS barrel region, on the basis of data coming from the SC units. It also uses the curved trajectory of the particles in the magnetic field to provide  $p_T$  estimation. The PHTF segmentation follows the one of the DT sectors therefore there are 12 PHTF units in each DT wheel. The only exception to this rule applies to the central wheel which is equipped with independent PHTF units looking to  $\eta > 0$  and  $\eta < 0$  respectively. Therefore there are in total 72 PHTF modules in the DT barrel system. The PHTF positioned in the outermost wheels perform track reconstruction taking advantage of the information coming also from the CSC Track Finder in order to avoid efficiency losses in the overlap region.

### The DTFF Algorithm

The PHTF algorithm is based on three different logic steps, as outlined in Fig. 3.16. Initially an *Extrapolation Unit* (EU) looks for segments that can be matched on the basis of an extrapolation algorithm which takes into account local track position and direction. Tracks are propagated outwards, with the exception of tracks in the MB4 station that are propagated inwards to MB3 stations due to the low sensitivity of the particle bending to  $p_T$  in this region. Extrapolation is considered successful if spatial position of real and propagated segments match inside a 99% efficiency window. In a second step a *Track Assembling* (TA) unit assembles segments selected by the EU to form a full track and assign it a quality word related to the number and type of stations involved in the reconstruction (quality encoding is shown in table 3.4). A matching between at least two segments is needed to generate a track.

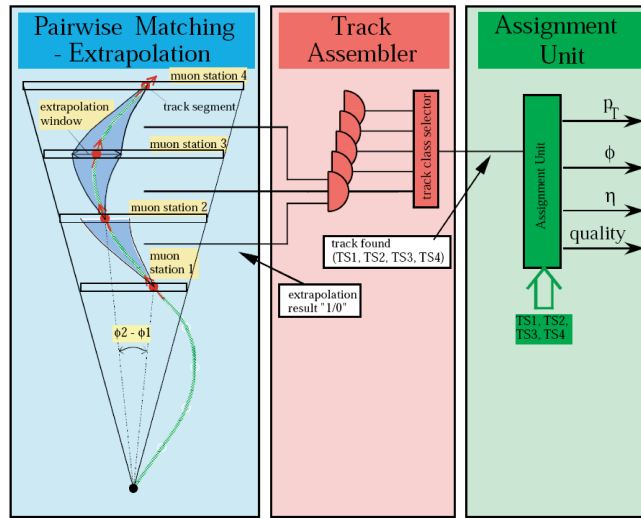


Figure 3.16: Overview of the PHTF algorithm.

Finally an *Assignment Unit* assigns muon physical parameters to the (up to) two reconstructed tracks with best quality codes. The  $p_T$  information value is computed using the  $\Delta\phi$  information coming from the two innermost stations involved in the matching, on the basis of pre-calculated LUTs.

Quality Value	7	6	5	4	3	2	1	0
Track Category	T1234	T123 T124	T134	T234	T12 T13 T14	T23 T24	T34	Null track

Table 3.4: *PHTF track quality encoding. Numbers in track category refers to the stations involved in the matching.*

During the extrapolation and assembling processes track segments coming from neighbouring sectors are taken into account, in order to properly match tracks crossing the boundaries between wheels and wedges. In principle this could generate copies of reconstructed tracks, therefore a ghost suppression mechanism has to be operated in the next steps of the Regional Trigger sorting (3.3.3). Furthermore muons coming at large eta ( $0.8 < |\eta| < 1.2$ ) cross both barrel end endcap regions and, therefore, to ensure redundancy to the Muon Trigger system, data exchange between the DT and CSC trigger system is foreseen. The track fitting task in this region is thus handled cooperatively by DTTF and CSCTF, whose exchange the trigger primitives coming from MB2/2 and ME1/3 chambers.

### 3.3.2 The Eta Track Finder

Quantities coming from the  $\theta$ -view of the DT Local Trigger system are sent, through the SCs, to the *Eta Track Finder* (ETTF) units. Informations coming from a single wedge are grouped together, and the ETTF performs its computations as schematically outlined in Fig. 3.17. A *Pattern Finder* Unit looks for matching of the informations coming from the different groups of BTIs to reconstruct a straight line, on the basis of a predefined set of patterns. Then cancellation of sub pattern replicas is performed, followed by assignment of a  $\eta$  value whose resolution is around 3%.

### 3.3.3 The Muon Sorter

The *Muon Sorter* receives information from the various DTTF boards and performs the final ranking on the trigger candidates delivering up to four

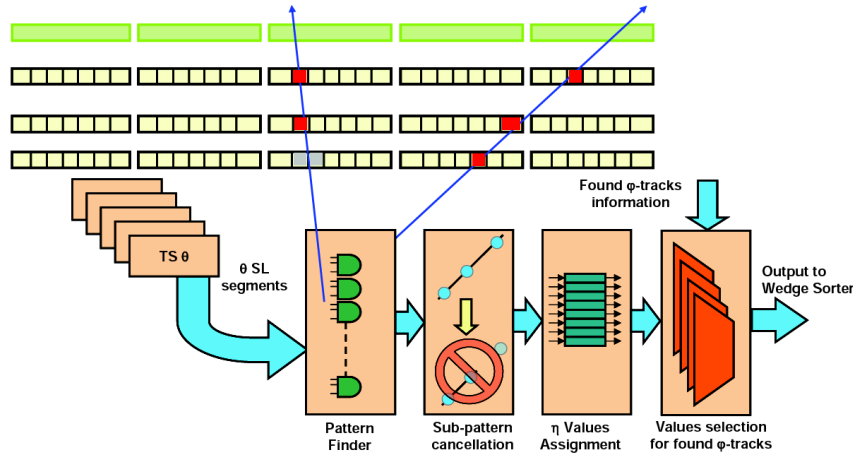


Figure 3.17: Overview of the ETTF algorithm.

tracks to the Global Muon Trigger. It is divided in two processing layers named *Wedge Sorter* (WS) and *Barrel Sorter* (BS). The first is in charge to perform a selection based on the candidates coming from a single wedge. Each WS receives in input up to 12 tracks (144 in the whole barrel) and forwards (up to) two muon candidates per wedge to the BS. The latter is in charge to further reduce the total amount of (at most) 24 muon tracks to the final limit of 4 candidates requested for GMT processing. Ghost trigger suppression has also to be performed in order to cancel possible replicas coming from adjacent sectors. The full system consist of 12 WS boards and one BS board located in the CMS counting room.

### Muon Sorter Logic

The Muons Sorter receives information coming from DTTF and does not perform manipulations on the physical content of the muon track; a scheme on the data in input to the WS is given in table 3.5. The sorting process is based on comparison of 8-bit words composed by reconstruction quality and  $p_T$  information.

PHTFs belonging to adjacent sectors (both in  $\eta$ -view and  $\phi$ -view) can reconstruct copies of the same muon track since they operate, almost independently, on similar informations. Therefore, in order to be able to efficiently

Data	Width (bits)	Type & comments
Quality	3	DTTF quality as in table3.4
$p_T$	5	
$\phi$	8	signed, 1-compl
$\eta$	6	non linear scale
$\eta$ quality	1	coarse/fine meas.
Charge	1	
Track address	7	Encoded info on segment position

Table 3.5: *Data content of the track candidate delivered by the DTTF to the muon Sorter*

trigger on di-muons of closed trajectories, a background suppression mechanism that reduce the number of fake trigger below the expected di-muon rate (of the order of 1% of single muons one) is needed.

To fulfill this requirement the Muon Sorter looks for tracks coming from adjacent sectors whose are built with common segments and discard the one(s) reconstructed with worse quality. Simulations performed using single muons generated in a  $5 \text{ GeV}/c \leq p_T \leq 100 \text{ GeV}/c$  range, uniformly distributed in the barrel region, showed that the fake track rate can be reduced down to 0.3% at the BS output. The Latency of the Muon Sorter system is

Component	Latency (BX)
DTTF to WS link	1
WS sorting	2
WS to BS link	2
BS sorting and ghost suppression	3
TOTAL	8

Table 3.6: *Muon sorter total latency and single components contribution.*

summarized in table 3.6 and it is of 8 BX in total. It has to be noticed that the WS ghost suppression mechanism receives track addresses and qualities one BX in advance, thus fake reduction is performed before the sorting and does not add latency to the system.

The study of the performances of the DT Trigger System is part of this work, therefore results coming from dedicated analysis, performed on recently collected data, is shown in 5.3.

## Chapter 4

# DT Local Trigger Emulation and Monitoring

Many software utilities complement the DT Local Trigger hardware electronics. Among others a complete, bit-wise, emulation of the trigger logic and a suite of programs devoted to the online monitoring of the trigger functioning have been developed as a part of the CMS Software Framework (CMSSW). The first can be used to perform realistic simulations of the system response as well as statistical validation of the trigger electronics output. The second is a fundamental instrument to ensure correct operation of the trigger during data taking and allows to promptly react in case of problems.

### 4.1 DT Local Trigger Emulation

A logical description of the DT Local Trigger sorting algorithms is implemented in the CMS Software Framework (CMSSW) [45] and is part of the emulator code used to reproduce the response of the whole L1T system. Every component of the DT Local Trigger hardware is described using an object oriented software structure where each trigger board (in some cases each single chip) is represented by a C++ class. Sorting algorithms are simulated using bit-wise arithmetic. The behaviour of every emulated chip can be programmed using dedicated configuration classes populated with the same kind of parameters used to perform hardware configuration.

The code implementation is mainly included under the CMSSW `L1Trigger` and `L1TriggerConfig` directories; the first contains the description of the

sorting algorithms and the second houses the configuration related classes. The emulator code has been an important instrument during the hardware development phase and is presently a fundamental part of the detector simulation process. Among other things it can be used to perform hardware validation studies and spot possible problems occurring to the “real” trigger system (these kind of studies are described in more detail in 5.5).

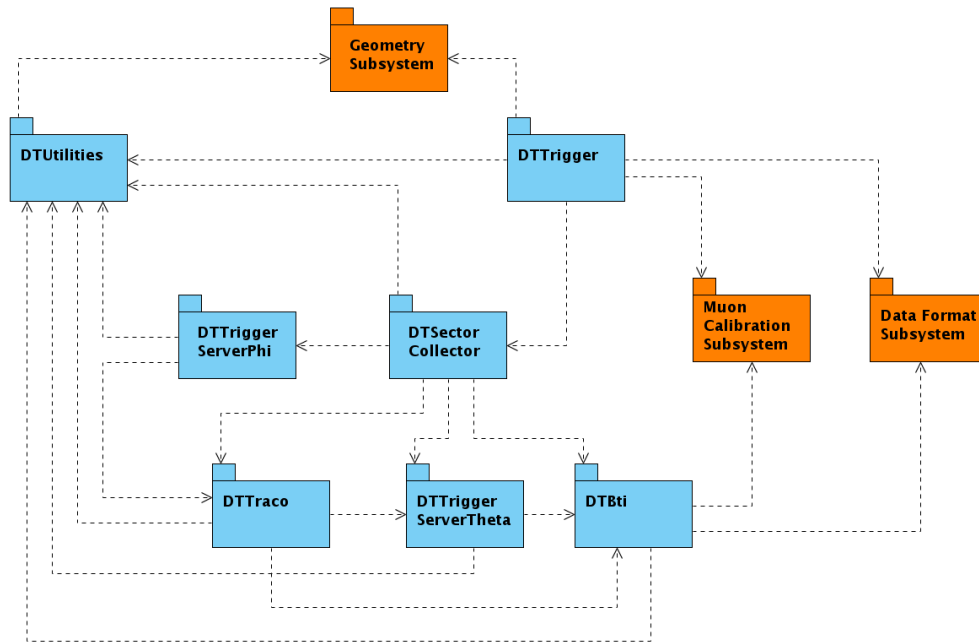


Figure 4.1: *Schematic view of the DT Local Trigger emulator packages included under the L1Trigger directory. Orange boxes refer to external dependencies.*

A schematic view of the DT emulator packages included in the L1Trigger directory is shown in Fig. 4.1. Each of them is devoted to a specific task:

**DTTrigger** : Interface package responsible for the instantiation of all objects. It also provides modules to include the DT Local Trigger emulation in the CMSSW processing and perform test studies;

**DTUtilities** : Contains classes related to geometrical description of the trigger components as well as the base implementation of transient objects

used to store intermediate trigger data;

**DTBti** : Simulation of the BTI (see Section 3.2.1);

**DTTraco** : Simulation of the TRACO (see Section 3.2.2);

**DTTriggerServerTheta** : Simulation of the  $TS\theta$  (see Section 3.2.3);

**DTTriggerServerPhi** : Simulation of the  $TS\phi$  (see Section 3.2.3);

**DTSectorCollector** : Simulation of the Sector Collector (see Section 3.2.4).

### Code Processing

The DT Local trigger emulation can be operated in CMSSW adding the `DTTrigProd` module to any of the *paths* used to define the software processing flow (see [47] for more details). The `DTTrigProd` is a so called **EDproducer** module - i.e. a module that generates trigger segments in the *official* data format used by the framework - and is used to produce emulated primitives that can be passed to other modules for further processing and/or be stored in files that can be re-accessed by CMSSW modules later on.

When the CMSSW processing starts, and a `DTTrigProd` module is included in the path, a `DTTrig` object is created. This is in charge for the management of the whole emulation process. Initially it generates a map `DTSectColl` and `DTTrigUnit` class instances. These objects are devoted respectively to the description of Sector Collectors and of the various components of the on-board trigger electronics (BTIs, TRACOs,  $TS\phi$ s,  $TS\theta$ s). In a second step the `DTTrig` assigns the `DTTrigUnit` instances of the same sector to the belonging `DTSectColl`. Each `DTTrigUnit` is linked to the associated muon chamber, from which it derives geometrical properties, and is populated with the various objects describing each part of the on-board trigger system (`DTBtiCard`, `DTTracoCard`, `DTTSPhi`, `DTTSTheta`). Each of these objects inherits from the `DTCache` class that provides general description of the containers used to store transient trigger candidate information (the same applies also to `DTSectColls`). A class diagram of the objects instantiated at by the `DTTrig` class is shown in Fig. 4.2.

As the event processing begins, the `DTTrigProd` module looks for the presence of digitized information from the DT detector (DT *digis*) and passes them to the `DTTrig` class, in charge to start the emulation process. The

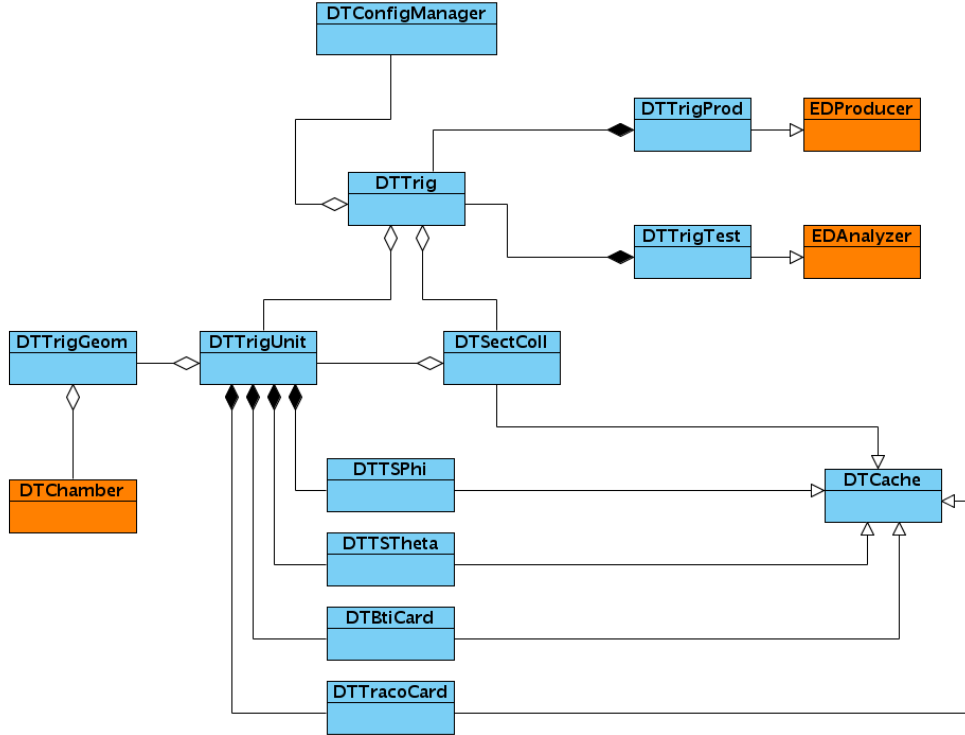


Figure 4.2: Class diagram of the objects instantiated at the beginning of the L1 DT Local Trigger emulation process.

DT digis are the outcome of the TDC units used by the detector readout system. They are the sum of the electrons drift time within a cell plus a time pedestal parameter mainly due to trigger latency. These pedestals are commonly called *tTrigs* and they need to be subtracted to the total digi time to properly operate the trigger emulator logic. They are computed with SL granularity and second order correction parameters (named  $t_0s$ ) are also generated to take into account differences coming from cell to cell. A `DTTrigSync` class instance performs pedestal subtraction and data is then sent to BTI objects for reconstruction.

It is important to point out that the digitized information seen by the emulator slightly differs from the discriminated analog signal measured by the hardware BTI. Moreover, uncertainties on the *tTrig* and  $t_0$  computation do

not allow to perform pedestal subtraction with infinite precision. For these reasons perfect matching between emulation and hardware trigger output is not possible in principle, however very good statistical correspondence, around 98-99%, is achieved. This allows to perform hardware validation using the emulator code (see 5.5).

About 40000 BTIs equip the real CMS detector, but, on average, only  $30 \div 40$  of them have non null data for each event. Therefore the static generation of the full set of BTI chips during the `DTTrigUnit` creation would lead to a huge, unnecessary, memory waste. Actually when digis are found in a certain cell, the `DTBtiCard` object checks for the existence of the `DTBtiChip` linked to that cell and, if it is not present, it dynamically creates it. The latter corresponds single hardware BTI chip and it the class devoted to perform track segment reconstruction. The `DTBtiChip` processing is then operated and the output is stored in the `DTBtiCard`, ready to be delivered. When the next event is taken into account, existing instances of the `DTBtiChip` classes are deleted before the digis are read-out, in order to free the memory used during previous event processing.

The same software architecture is used in the implementation of TRACOs. Approximately 4000 TRACO chips are present in the detector and the use of `DTTracoCard` classes able to instantiate single `DTTracoChip` objects still drives to considerable memory savings. In this case a single `DTTracoChip` is generated if non null information is found in the BTIs it is connected to.

On the opposite, single `DTTSPhi` and `DTTSTheta` classes are statically generated during single `DTTrigUnit` construction and are deleted only at the end of the processing. In this case only one instance per class type is present for every station. This leads to an amount of 250 `DTTSPhis` and `DTTSThetas` in total. A dynamical generation of class instances would not lead to substantial memory savings. On the other hand the reduced number of `malloc` and `free` calls during processing leads to some performance improvements. An identical solution is adopted also in case of the `DTSectColl` classes.

To reduce processing times, single `DTBtiCard` operations are executed only in the chambers where DT digis have been found, and every subsequent step of the trigger reconstruction chain is carried out only if at least one segment candidate is found in the output buffer of the object connected to the one to be processed. As an example only the `DTTSPhi` instances referring to stations where `DTTracoCard` output buffer is non empty are run. This leads to a considerable savings in term of CPU cycles.

Apart from the `DTTrigProd` EDproducer, a further CMSSW module, called `DTTrigTest` exists. It is a so called `EDAnalyzer` [45] and it operates trigger emulation in a way identical to the one previously described. The only difference is that, in this case, an output file written in an unofficial data format is generated. This file includes information coming from intermediate steps of data processing (such as the output coming from `DTBtiCard` or `DTTracoCard` buffers) and allows to perform detailed system debugging and performance studies.

### Emulator Configuration

As already mentioned, the DT Local Trigger sorting logic is highly flexible and a large fraction of the possible hardware configuration parameters is replicated at the emulator level. This ensures proper matching between hardware and software configuration conditions during validation and allows to perform reliable simulations of the detector performance in a realistic scenario. A complex set of mask bits is also used to prevent the emulation of those chips that are broken or do not work properly.

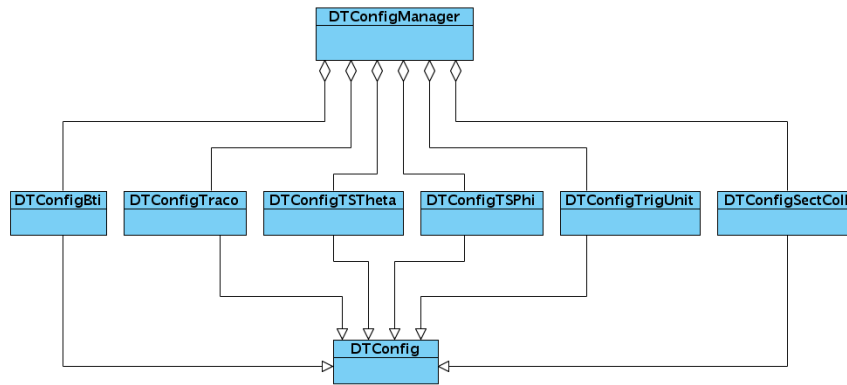


Figure 4.3: *Class diagram of the objects used to perform DT Local Trigger emulator configuration.*

This high level of flexibility requires a complex software configuration infrastructure. Each single emulator chip (or board) class has its own kind

of configuration class and a different instances of these objects are generated for every emulated chip. All configuration classes are located inside the `DTPGConfig` package included under the `L1TriggerConfig` directory. A class diagram showing the relationship among the C++ objects included in the package is shown in 4.3.

The interface class used to manage the various configuration objects is called `DTPGConfigManager`. It supplies methods to access to single configuration objects or collection of them. `DConfigTSPhi`, `DConfigTSTheta` and `DConfigTrigUnit` class objects are replicated with chamber granularity and a `DConfigSectColl` instance exists for every sector. Each of them can be queried using dedicated `DConfigManager` get methods. `DConfigBti` and `DConfigTraco` instances can be accessed respectively with BTI and TRACO granularity, but dedicated getters can be used to retrieve the full list of `DConfigBti` and `DConfigTraco` objects within a chamber. This allows to deliver to the `DTBtiCard` and `DTTracoCard` a reduced list of configuration objects they can use to dynamically generate `DTBtiChip` and `DTTracoChip`, optimizing the access to the configuration classes.

When the CMSSW flow starts, before the first event is processed, an `ESRecord` [46] - i.e. a record object containing configuration information - holding a `DConfigManager` class instance is produced. This is later retrieved by the `DTTrig` object and is used to configure each board chip. A pointer to the correct configuration class instance is passed to the various emulated `TS $\phi$ s`, `TH $\theta$ s` and `SCs` at the moment of their creation. The `DTTracoCard` and `DTBtiCard` instead receive containers holding pointers to all the BTI and TRACO configuration objects present in the chamber. When a single `DTBtiChip` or `DTTracoChip` is created during event processing a pointer to the correct configuration object is retrieved from the container.

Since the CMSSW flow can span over different data-taking runs, the system configuration can change during the program flow. In this case the existing `DConfigManager` instance is destroyed and a new one is created. The single board (or chip) configuration objects are deleted as well, and newly created ones have thus to be propagated to the various trigger objects. In order to perform this operation the `DTTrig` keeps track of the `DConfigManager` instance that it is presently using and triggers the update only when it actually changes.

The various configuration objects are transient and they are dynamically created and destroyed at different phases of the CMSSW processing. In

order to be generated, they need to be built using configuration information that is, somehow, permanently stored. This information can be actually read by configuration file or accessed from database<sup>1</sup>. The CMS DT database stores the exact list of hardware configuration parameters of each trigger chip under the form of string of bits. If a database driven configuration of the emulator is required, a record dependent `ESProducer` module, named `DTConfigDBProducer`, looks for the presence of an `ESRecord` containing the configuration parameters coming from the database, packed as string of bits, and creates the various configuration object instances unpacking these strings. It then populates the `DTConfigManager` object and creates the related `ESRecord`. When data in the DT database `ESRecord` changes (i.e. at the beginning of a new run) the `DTConfigDBProducer` is operated again and it generates a new `DTConfigManager` instance.

For simulation purposes, the emulator configuration classes are presently generated reading configuration information from file. In this case an ideal description of the system, that does not include dead channel masking or single chip configuration tweaks, is created. The `DTConfigManager` generation mechanism is similar to the one described in the previous scenario. This time an `ESProducer` module, named `DTConfigProducer` creates identical copies of the various configuration objects on the basis of the parameters wrote in the configuration file.

Both the `DTConfigDBProducer` and the `DTConfigProducer` modules are included in the `DTTPGConfigProducers` package under the `L1TriggerConfig` directory. The choice to operate one module or the other is only driven by the kind of scenario that is intended to emulate. In both cases the emulator code can run smoothly accessing transparently data generated by any of the two `ESProducers` without the need to tweak a single `DTTrigProd` set up parameter.

## 4.2 Data Quality Monitoring in CMS

To monitor the data quality released by the the CMS detector during the various run phases, dedicated analysis must be performed on the collected data to validate them and eventually spot system misbehaviours. The CMS

---

<sup>1</sup> The description of the CMS database infrastructure is beyond the scope of this discussion, however more information can be found at [48]

Data Quality Monitoring (DQM) infrastructure, is developed to perform a fast, preliminary, analysis of the performances of the various subdetectors.

DQM related studies are operated both in online, on a fraction of events collected during data taking, and offline, on the full available statistics. Real time DQM analysis are devoted to the prompt detection of misbehaviours in the data acquisition process, therefore they rely on the production of high granularity observables able to spot problems occurring on small portions of a single subdetector (such as a single DT chamber or a fraction of it). Offline DQM studies, on the other hand, are mainly devoted to the validation of the overall subsystem performance and to the monitoring of high level object reconstruction, they generate low granularity observables and they are involved in the data certification process.

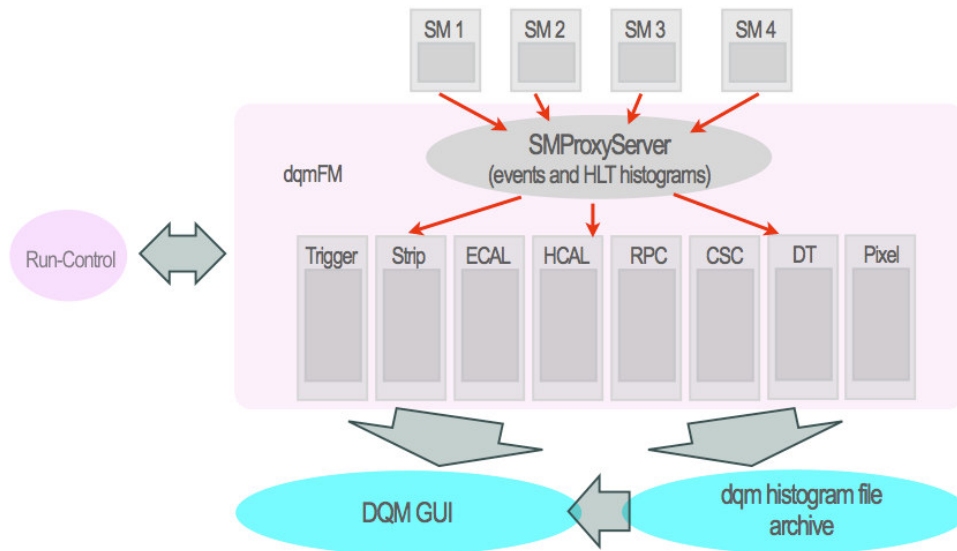


Figure 4.4: *Schematic view of the CMS DQM architecture.*

A schematic view of the CMS Online DQM infrastructure is shown in Fig. 4.4. Almost all subsystem applications receive data from a **Storage Manager Proxy Server** able to deliver events at a configurable rate up to 25 Hz. The data stream coming from this source can be filtered on the basis of the trigger information bits set by the HLT. This allows to perform different DQM analysis selecting the most appropriate data sample to be used for every

kind of study. However, in some cases, DQM monitoring operations have to be performed on the full information accessible at the L1T level. To satisfy this need a few selected DQM modules are operated directly on the HLT Filter Units (see section 2.7.2). In particular this applies to the monitoring processes supervising the behaviour of the front end readout system which are devoted to the detection of data corruption problems. However only a reduced number of observables can be produced by these modules in order to avoid to saturate HLT bandwidth with monitoring information flow.

Single subsystem DQM analysis are performed by independent CMSSW processes, running in dedicated machines located in the CMS surface filter-farm room. In this scenario different **EDAnalyzers**, devoted to perform various kind of studies, are executed. These modules can be further subdivided in two categories depending on the type of operation they perform. **DQMSources** look at the data event-by-event and produce basic (often high granularity) observables. These are called **Monitor Elements** (MEs) and are a generalization of the common monitorable quantities (such integer and floats as well as histograms). As an example, single ME could be an histogram describing cell occupancy within a DT chamber, as well as a float number used to indicate which fraction of a certain subdetector is properly functioning. Apart from observables information the MEs can register the outcome of tests performed on their data content. This is done by **DQMClients** that look at the MEs produced by the **DQMSource** modules to create summary observables (still in ME format) and execute dedicated **Quality Tests** (QTs). The outcome of these tests can be used to evaluate the overall performance of a single subsystem and easily spot misbehaviours. Specific problems may then be investigated in more detail looking at the full list of MEs produced by the **DQMSources**. The management of the various MEs generated by a single CMSSW DQM process is performed by a **DQMStore** object. **DQMClients** can thus query the **DQMStore** to retrieve ME objects generated by the **DQMSources** and undertake their own operations. Additionally the **DQMStore** can send the various MEs generated by a single subsystem process to a **DQMCollector** program. This picks up (in real-time) analysis results coming from the various sub-detector processes and sends them to the **DQM Graphical User Interface** (DQM GUI). The GUI allows thus to perform browsing of the outcome of DQM analysis in real-time during data taking. The **DQMStore** is also accessed by a **DQMSaver** module devoted to periodically save DQM analysis results into file. These files are centrally archived and can be accessed by the

DQM GUI for offline browsing.

In the case of offline DQM, analyses are operated during central data reprocessing and they profit of full statistics and most recent calibration constants. Reconstruction of low and high level objects is monitored, together with detector performance, and the outcomes of these studies are used to finalize the data certification process on which subsequent physics analysis will rely on. Results are saved by the `DQMSaver` module at the end of the run reprocessing, and can be browsed using a dedicated version of the DQM GUI.

### 4.2.1 DT and DT Local Trigger Online Monitoring

The DT and DT Local Trigger related monitoring is performed online as a part of the whole central DQM processing. However a dedicated DQM infrastructure (DT-DQM), based on components similar to the ones used by the central DQM, has been deployed. It can be used both during global data-taking and during private DT runs, being an independent tool to monitor the DT system functioning in case the central DQM is not operated. Moreover it can accomplish, if needed, slightly different analysis with respect to ones carried out by the central DQM and bug fixes or updates can be steadily performed, as the full system deployment is simpler than in the central DQM case. This is especially important in the first phases of data taking and allows to promptly react to unexpected problems.

In any case the main observables produced both by private and official DQM are similar. Histograms displaying cell occupancies, time boxes distribution and local segment reconstruction performances are generated with chamber (or SL) granularity. Data corruption errors and the status of the read out system are also monitored. Most of the DT-DQM related computations are operated on physical triggered events but dedicated studies are also carried out selecting calibration streams. Quality tests are performed on these *high granularity* plots and their outcomes are summarized in histograms showing the status of a single wheel or of the whole barrel.

In case of monitoring of the trigger performances, high granularity plots are generated by a dedicated `DTLocalTriggerTask DQMSource` module. It operates checking the quality of the primitive, its time origin in terms of BX and the 1st/2nd track bit used to distinguish the (up to) two trigger segments delivered by a chamber for each processed BX. This information

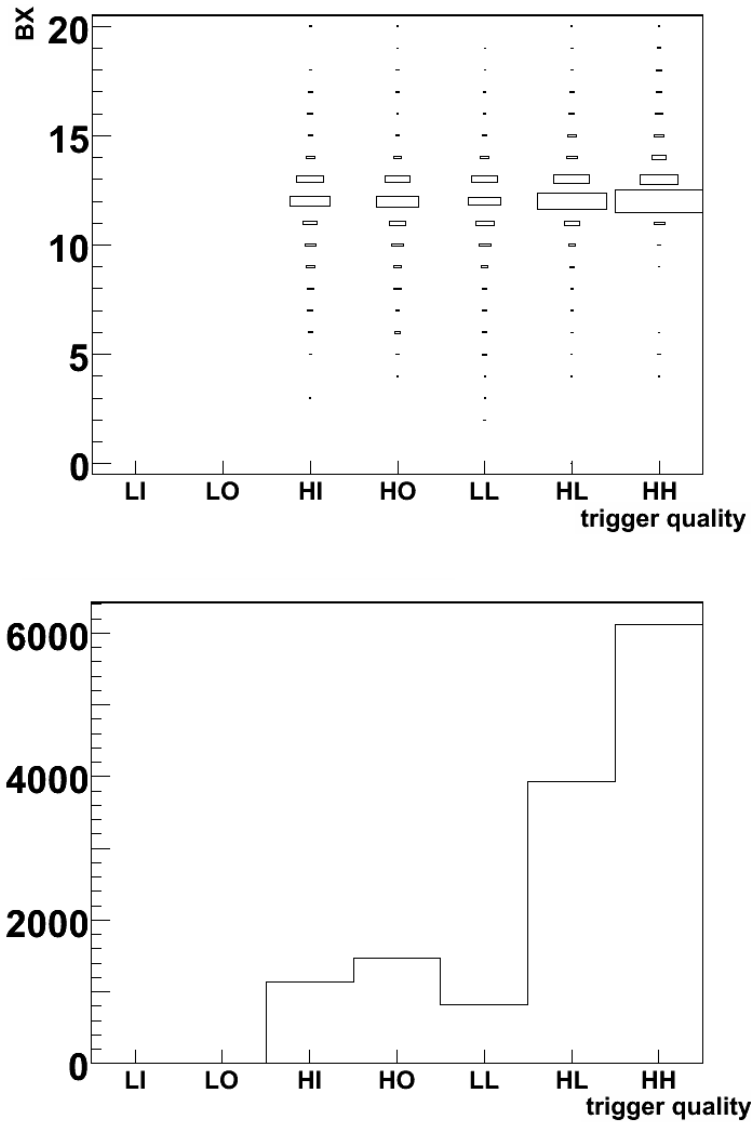


Figure 4.5: *DT Local Trigger DQM high granularity plots showing BX distribution as a function of the primitive quality (top) and quality of the best trigger segment found in each event (bottom).*

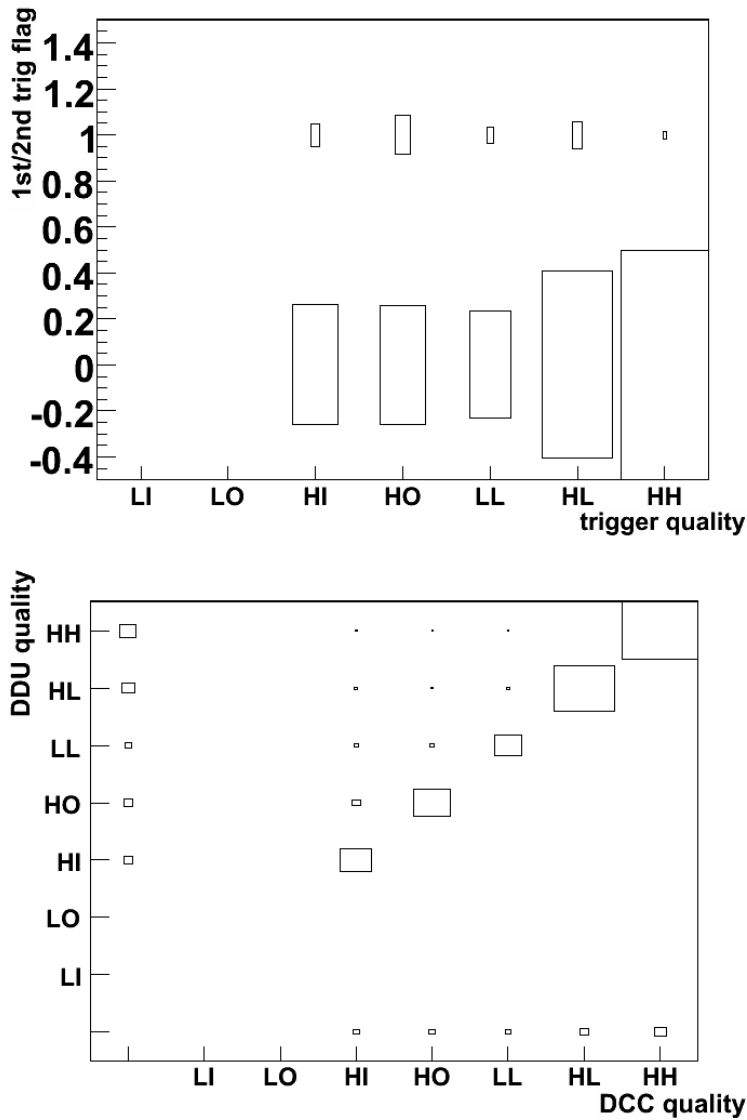


Figure 4.6: *DT Local Trigger DQM high granularity plots showing quality distribution for first and second trigger tracks (top) and matching of the quality word coming from two different read out system (bottom)*

can be read out both at the output of the Sector Collector and at the input of the DT Track Finder, depending on the data taking conditions. Therefore similar plots can be produced using both kinds of information and a check of the matching between the two can also be operated. This helps to validate the consistency of the data transmitted along the trigger chain.

Figs. 4.5 and 4.6 show some of the chamber granularity plots generated by the `DTLocalTriggerTask` module. The top histogram of Fig. 4.5 shows the BX assigned to each trigger primitive as a function of its quality. This kind of information is useful to check both reliability of the trigger reconstruction and system synchronization. The bottom plot of the same figure shows the quality distribution of the best trigger (i.e. the highest quality one) found in a single chamber at each event. This observable can be used to check the reliability of the trigger reconstruction as well. However in this case the computed information is insensitive to synchronization issues and to the generation of *out of time* ghost triggers. The latter have in general a lower quality with respect to the “good” trigger candidate thus their presence is suppressed in this plot. This kind of histogram can thus be used to generate low granularity summaries. Fig. 4.6 (top) shows the quality distribution of first and second track segments. Tests to validate the reliability of the trigger ghost suppression algorithm can be performed on the basis of the content of this histogram. Finally a correlation plot, used to validate the matching of information coming from the two possible readout systems, is depicted in Fig. 4.6 (bottom). In the histogram the quality of the best trigger, found by each of them at every event, is compared. Small discrepancies are due to differences in the range of BXs the two read out systems are configured to look at. All the observables presently described are computed using information coming from the  $\phi$ -view of the trigger system, similar histograms are generated also for the  $\theta$ -trigger.

Quality tests are computed by a dedicated `DQMClient` module, named `DTLocalTriggerClient`, on the basis of information coming from the bottom plot of Fig. 4.5 and on the top histogram of Fig. 4.6. The first is used to compute the fraction of correlated (HH+HL+LL) triggers and an alarm is issued if this observable is found to be below a certain threshold. This measured quantity allows to estimate the performances of the trigger algorithm but is insensitive to possible problems due to the presence of dead cells or layers<sup>2</sup>. In the second case the ratio between the number of second

---

<sup>2</sup> From time to time High Voltage distribution problems can force half a detection layer

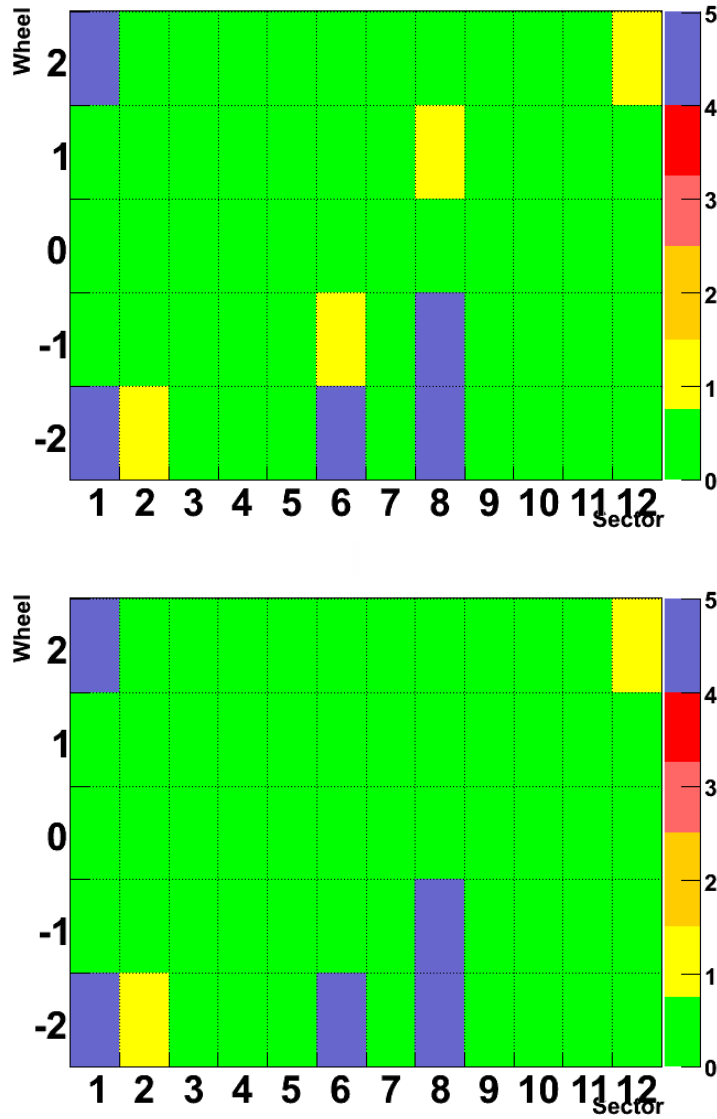


Figure 4.7: *DT Local Trigger DQM summary plots showing the outcome of quality tests performed on the fraction of correlated triggers (top) and on the second track ratio (bottom) observables.*

of a chamber to switch off, an estimator based on the fraction of HH triggers only would be sensitive to such a misbehaviour.

and first track segments (called second track ratio), delivered by a station, is evaluated. This time an error message is generated if this observable is above a given value. The outcome of this ratio is a function of the flux of double muons within a chamber and, if a single station delivers too many second tracks, problems with its ghost suppression mechanism or with fake trigger segment generation (due to noise) may be present.

At the top level the outcomes of both kind of tests are presented using coloured two dimensional plots with granularity of the full muon barrel. These plots are shown in Fig. 4.7, the topmost one being related to the fraction of correlated triggers computation and the bottom one referring to the second tracks ratio. Each histogram bin refers to a single sector and a color code is used to report how many chambers failed the test. Green means that everything is working as expected while colours from yellow to red report that one to four chambers are not behaving properly. Blue filled bins refers to sectors that were not included in the readout during the run. No automated action is taken on the basis of quality tests results, and is up to the shifter to promptly react in case of general malfunctioning of the system.

The `DTLocalTriggerClient` module generates also wheel granularity plots used to check the trigger system synchronization. The BX distribution measured by the top plot of Fig. 4.5 is exploited to produce these histograms. The most populated BX, found summing up information coming from HH and HL trigger segments, is measured and is taken as the one where a station is supposed to deliver correctly reconstructed primitives. All the muon barrel sectors should, in principle, deliver trigger segments at the same BX and, if one of them is found to deliver them earlier or later than the others, its latency should be adjusted at the SC level. This timing alignment is called *coarse synchronization*. The coarse synchronization status can be monitored at DQM level using the plot shown in Fig. 4.8 (top). In the histogram the most populated BX of each chamber is shown with wheel granularity.

In case a single station (or sector) is found to be shifted in latency with respect to the others an estimation of the magnitude of this shift should be given, in order to perform corrections. During cosmic ray data taking, the difference between the mean and the mode of the HH+HL BX distribution previously computed has been proved to give a reasonable estimation of the latency shift of a single chamber. By multiplying the outcome of this difference by the time interval between 2 consecutive BXs (25 ns) it is possible

to measure the extent of the latency correction that must be performed<sup>3</sup>. Results of such computations, for a single wheel, are shown in the summary plot depicted in Fig. 4.8 (bottom). The problem of the synchronization of the trigger system within the  $ns$  precision (*fine synchronization*) is actually more complicated and it can not be solved at the online DQM level. Studies about the development of a method to perform fine synchronization for the DT Local Trigger System (on the basis of cosmic rays collected during commissioning) are described in more detail in 5.4.

---

<sup>3</sup> The precision achievable with this estimation is of the order of a few  $ns$

<b>MB4</b>	0	1	0	0	0	0	0	0	0	1	0	0
<b>MB3</b>	0	1	0	0	0	0	0	0	0	1	0	0
<b>MB2</b>	-1	1	0	0	0	1	0	0	0	0	0	0
<b>MB1</b>	-1	1	0	0	0	1	0	0	0	1	0	0
	<b>1</b>	<b>2</b>	<b>3</b>	<b>4</b>	<b>5</b>	<b>6</b>	<b>7</b>	<b>8</b>	<b>9</b>	<b>10</b>	<b>11</b>	<b>12</b>

<b>MB4</b>	7	-12	5	0	3	10	8	9	3	-12	4	5
<b>MB3</b>	8	-12	4	6	4	11	3	7	3	-14	3	3
<b>MB2</b>	23	-9	4	4	3	-12	0	8	3	11	4	7
<b>MB1</b>	22	-5	2	4	4	-7	0	9	2	-12	2	3
	<b>1</b>	<b>2</b>	<b>3</b>	<b>4</b>	<b>5</b>	<b>6</b>	<b>7</b>	<b>8</b>	<b>9</b>	<b>10</b>	<b>11</b>	<b>12</b>

Figure 4.8: *DT Local Trigger DQM summary plots used to test coarse system synchronization. The top histogram shows the BX where most of the high quality (HH/HL) triggers are delivered by the station. The bottom one shows the difference between the mean and the mode of the high quality (HH/HL) trigger BX distribution expressed in ns.*

# Chapter 5

## DT Local Trigger Commissioning with Cosmic Rays

The CMS experiment has been installed in a dedicated cavern located below the Point 5 site along the LHC tunnel, near the french village of Cessy. A commissioning phase devoted to the testing and integration of the various components of the detector, and its software infrastructure, already began when the experiment was being assembled in the surface hall, and is presently ongoing. *Private* subsystems runs and *global* datataking exercises, where different subsystems are operated at the same time, have been carried out taking advantage of cosmic muons traversing the experimental site.

The DT barrel system, and in particular its L1T electronics, have played an important role in data acquisition since the early days of commissioning. Therefore DT trigger performances with cosmic rays have been thoroughly investigated.

### 5.1 CMS Commissioning with Cosmic Rays

The commissioning of the CMS detector already started in the Point 5 surface assembly hall where single subsystems tests, as well as globally coordinated exercises were performed. During the Aug-Nov 2006 period, a phase named *Magnet Test and Cosmic Challenge* (MTCC) was carried out with the purpose of testing the CMS superconducting solenoid and study the per-

performances of the various subdetectors under the magnetic field. A vertical slice of many subsystems, including a pilot silicon tracking system, ECAL, HCAL and both, barrel and endcap, muon detectors, was operated to collect data with and without field. About 200 millions cosmic muons were collected using the Global Trigger and DAQ systems. After that the central detectors were removed and the magnetic field was mapped with a precision of  $10^{-4}$ . The various information collected were used to test the calibration and alignment procedures as well to compare single subsystems performances with respect to the simulations. The first CMS physical measurement, the measure of the cosmic-muon charge ratio, was also performed [49].

Subsequently the lowering of the detector's heavy elements started in November 2006, when the forward calorimeters were moved, and finished in January 2008, when the last CMS endcap disk reached the cavern floor.

Single subsystem testing continued underground and, as soon as the the internal wheels of the experiment were lowered, a series of centrally coordinated data taking efforts named *Global Runs* (GRs) started. Different GRs were performed at intervals of 1-2 months and had a duration of a few days. Their main targets were:

- the integration of increasing fractions of the detector, together with the testing of the trigger and DAQ infrastructure;
- the analysis of single subsystems and combined performances;
- the development of a reliable prompt reconstruction, monitoring and alignment/calibration infrastructure;
- the testing of the global shifting procedure to earn experience in running the experiment.

Fig. 5.1 shows the participation of the various subsystems per GR period, expressed as a fraction of the whole detector read out.

Starting from May 2008, most of the components had been integrated and the GR character changed. Profiting of the improved data taking stability, four Cosmic Runs at Zero Tesla exercises (CRUZETs) were performed. Every CRUZET had the duration of about one week and the high data taking efficiency ( $\sim 50\%$ ) allowed to collect about 300 M cosmic events in total. Prompt offline reconstruction and Data Quality Monitoring were fully integrated in the data acquisition procedure and the August CRUZET phase

## 5.1 — CMS Commissioning with Cosmic Rays

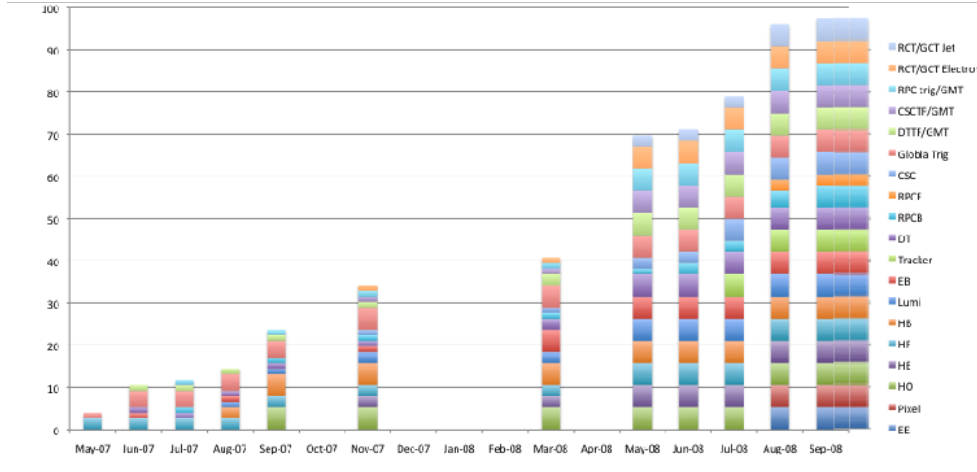


Figure 5.1: *Subsystems participation to the various global exercises as a function of the GR period.*

involved also the inner tracking system leading to a detector participation greater than 90%.

At the end of August 2008 the CMS magnet yoke was closed and the underground magnet commissioning phase started. A 3 T field strength was reached before the program was suspended to allow LHC beam commissioning. During October and November 2008 the most recent phase of global CMS commissioning took place. It was named *Cosmic Run at Four Tesla (CRAFT)* and consisted of a full month of continuous cosmic run with the superconducting solenoid set at its nominal working conditions.

An average data taking efficiency of 60% was achieved and periods of uninterrupted data acquisition exceeding 15 hours were reached (as shown in Fig 5.2). About 360 millions cosmic events were collected in total and 19 run days with a  $B = 3.8 T$  field allowed to accumulate  $\sim 300$  millions events with stable magnetic field conditions including Strip Tracker and DT in the readout (190 millions of them where collected including all the CMS components). This sample, together with the ones collected during CRUZETs are enough to perform many alignment/calibration studies as well as to operate many preliminary analyses. Fig. 5.3 shows a fully reconstructed track coming from a cosmic muon detected during CRAFT.

The analysis of the performances of the DT Local Trigger System de-

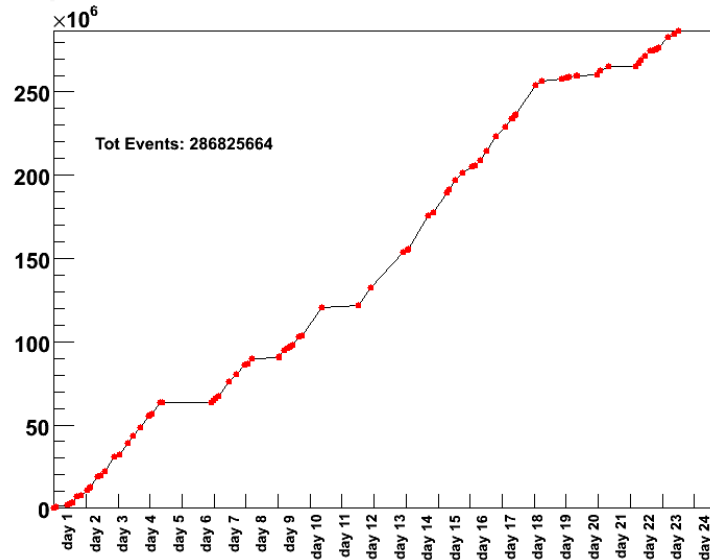


Figure 5.2: *Data Collected as a function of time during the CRAFT challenge. Points mark different runs starting times.*

scribed in the following sections is performed using data collected during the CRAFT run period, taking advantage of the maximal DT subsystem stability and participation.

### 5.1.1 DT Subsystem Commissioning with Cosmic Rays

Besides the global commissioning activity the DT system testing program foresees a detailed analysis of the subdetector performance that already started when CMS was being assembled in the surface hall and is still ongoing in the cavern. After the insertion of the DT chambers in their final position, and their correct cabling for powering and data transfer, initial tests were performed on single stations to check their functioning and schedule interventions if needed.

As soon as the integration progressed, a second phase called *Sector Commissioning* was operated in order to read out data coming within a DT sector, allowing the tracking of cosmic muons between different stations. Later on *Wheel Commissioning* exercises were performed. In that case most of the

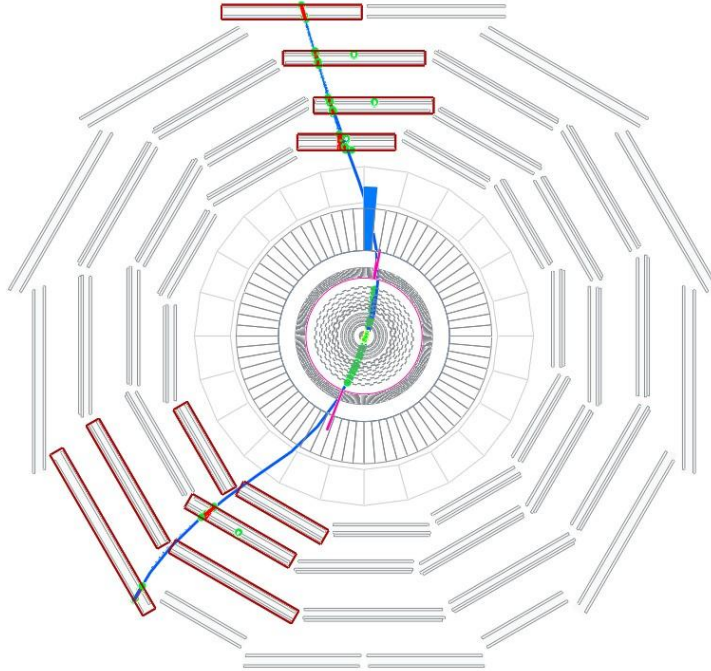


Figure 5.3: *Event display showing a global reconstructed track from a cosmic ray signal detected during CRAFT.*

chambers of a wheel were read out together allowing subsystems and trigger synchronization.

Online and offline performance studies were carried out during all the local commissioning phases to determine a complete mapping of the cell and trigger efficiencies as well as to identify dead and noisy channels, in order to include them in the configuration database. Typical cell efficiencies for cosmic rays have been proved to vary within a 90 – 100% range and the overall rate of dead cells has been found to be as low as the 0.2% of the total.

In Summer-Autumn 2006 DT sectors 10 of wheel +1 and +2 and sector 11 of wheel +2 participated to the MTCC exercise. Dedicated reconstruction algorithms applied on the data collected during the challenge, allowed to discriminate the charge sign of cosmic muons traversing the stations in presence of the magnetic field. A charge ratio measurement was performed

[49] and results are in good agreement with those of previous experiments, as seen in Fig 5.4.

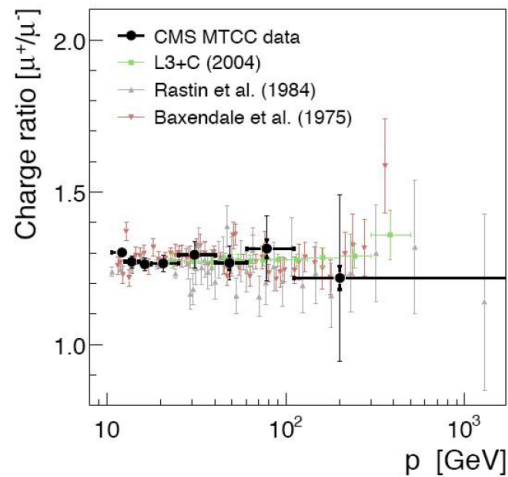


Figure 5.4: *Measurement of the cosmic muon charge ratio as a function of particle momentum. Results from CMS MTCC exercise are compared with ones coming from other experiments.*

The DT subsystem also participated to the various GRs performed in the CMS cavern, providing also muon trigger to the DAQ system. During the latest tests, the DT participation to data-taking was higher than 95%. The quality tracks reconstructed within the DT spectrometer allowed to perform precise extrapolation of the trajectory of cosmic muons to the earth surface above the CMS cavern.

Results from data taken during May-June 2008 are shown in Fig. 5.5. In the left plot the occupancy of extrapolated muons is shown as a function of the CMS  $z$  and  $x$  coordinates. The highest density of events in a roughly circular surface located above the negative endcap of the CMS apparatus is easily recognizable as the image of the shaft of the cavern. In this scenario the absence of magnetic field forbade the determination of the momentum of the incoming muons. However it is reasonable to assume that particles of larger momentum are more likely to cross the whole apparatus (from top to bottom) with respect to lower momentum ones. These, in fact, have a larger probability to stop somewhere in the detector material. The right plot

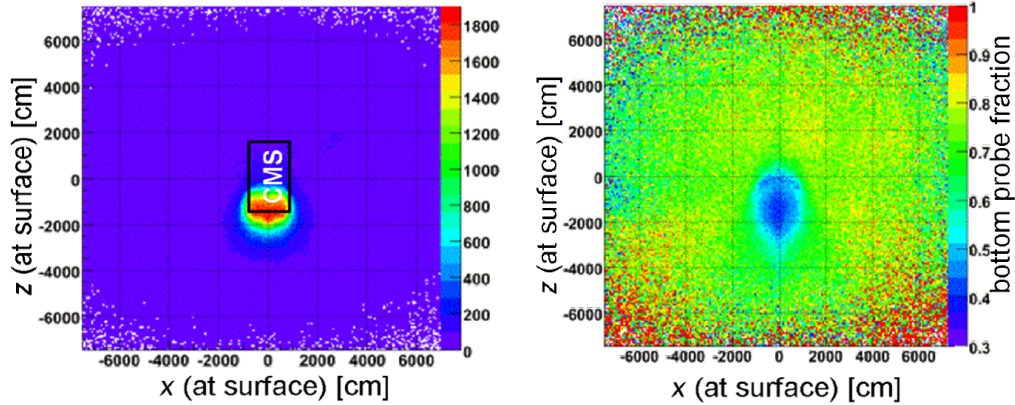


Figure 5.5: *Occupancy of DT reconstructed tracks extrapolated to the earth surface above the CMS detector (left) and fraction extrapolated track reconstructed in both upper and lower sectors of the DT system (right). Both distribution are expressed as a function of the CMS  $z$  and  $x$  coordinates.*

of Fig. 5.5 shows the fraction of muons reconstructed both in the top and bottom part of the detector with respect to the ones reconstructed at least in the top. It allows to confirm the previous guess, demonstrating that the muon coming from the shaft are relatively less energetic with respect to the ones that cross a  $\sim 100$  m thick ground bed before reaching the detector.

## 5.2 DT Trigger Configuration during Commissioning

Since CMS commissioning is being performed using cosmic muons, the natural way to operate data acquisition in this phase involves the use of the level-1 muon trigger. At the GT level a global trigger rate for cosmic muons around 360 Hz was obtained during CRAFT.

For the geometrical position of the chambers, and for the nature of the trigger algorithm, the DT level-1 trigger results especially suitable for cosmic data acquisition. As previously told, in fact, this system has been used since the early phases of global data taking and it provided a 240 Hz cosmic muon

detection rate to the GMT during the CRAFT exercise. However due to the differences between cosmic rays and muon coming from  $p$ - $p$  (bunched) collisions some technical adjustments have been performed to properly configure the trigger system to face this data taking scenario.

First of all cosmic muons do not come from the interaction point, instead they traverse the detector in a range of positions and directions not foreseen during collision data taking. The PHTF extrapolation mechanism described in 3.3.1 has therefore to be relaxed in order to maximize acceptance. During cosmic data taking the PHTF has thus been configured in *open* LUT mode, where a regional candidate is generated if a muon traversing a sector (or neighbouring sectors) produces at least a pair of trigger primitives at the same BX in the interested stations, independently from the position and direction of the reconstructed segments. Moreover the angular acceptance of the BTIs composing the  $\theta$ -view of the DT Local Trigger system has been set at its maximum range (instead of being computed to point to the interaction vertex).

A second correction has been made to cope with the fact that cosmic crosses the detector from top to bottom and are not generated at its center. The DT trigger system has therefore to be configured to face the different time of flight with respect to the one expected from muons coming from collisions. A particle travelling at the speed of light needs, in fact, about two BXs to cover a distance equal to the detector diameter, thus the trigger latency has been adjusted correspondingly.

Finally, unlike muons from bunched interaction, cosmic rays come uniformly distributed in time. This causes a worsening of the trigger performances and an increment of out of time uncorrelated trigger segments. In the DTTF open LUT configuration this generates a non negligible fraction of DTTF ghosts. To cope with these problems (and to reject fake triggers generated by synchronous noise within single chambers) the TRACO suppression mechanism (see 3.2.2) has been configured to accept uncorrelated triggers only if they are of H quality and they come together with a trigger in the  $\theta$ -view.

However the final configuration of the system has been also tested, taking dedicated runs using a closed DT-Local-Trigger/DTTF configuration with LHC timing.

### 5.2.1 Data Selection for Performance Studies

As previously pointed out, during the CRUZET exercise (but also in the previous phases of global data taking) the DT Trigger System played an important role in the data acquisition process. Therefore, to operate DT Local Trigger performance studies, precise data selection criteria must be applied to avoid overestimations coming from the fact that triggered data are present simply because the acquisition process was driven by the DT trigger system itself. On the other hand, as will be shown in section (5.3), the DT Trigger response is not uniform as a function of arrival time of the muon with respect to the hardware clock cycle. When a particle crosses the DT station near BX boundaries, in fact, the fraction of high quality reconstructed segments is reduced because single hits may be assigned to the neighbouring BTI sampling cycles (see 3.2.1). This causes a reduction of the fraction of high quality triggers. In such a case an underestimation of the system performances would be operated if the selected event sample is mostly populated in a clock phase where the system is not working properly.

If biases due to system synchronization effects want to be avoided, data selection can be performed choosing events triggered by the DT system within a single sector. To study the trigger performances of a certain chamber, the presence of a DT local trigger elsewhere in the same sector is thus asked. This comes from the fact that trigger data from different chambers of the same sector are delivered together by a single Sector Collector, and therefore no differences due to synchronization fluctuation are expected in this case. In addition, to exclude biases coming from the DTTF trigger selection criteria, the coincidence in time of two trigger segments, others than the one under investigation, is required.

Moreover, to measure trigger efficiency, the presence of local DT segments reconstructed using at least 7 of the 8 detecting layers of a station is asked. In this case the selection is driven by the presence of a 7/8 hits segment coming in a range of radial angles  $|\psi| \leq 30^\circ$  with respect to the perpendicular to the chamber. This allows to cope with the TRACO angular acceptance (see 3.2.2). The segments provide a good way to determine the particle local position and direction and they can be used to study the trigger radial and bending angle resolution as well.

In order to determine the fraction of events where the system generates a fake copy (*ghost*) of the trigger segment, when a single muon crosses a

station, a cut on the total number of hits recorded by the readout system is used. The requirement of the presence of, at most, 12 hits within the station under investigation allows remove events where multiple muons crossed one single DT chamber or where electronic noise was present. This ensures that the amount of second trigger segments delivered within a chamber has to be attributed to the trigger sorting algorithm and not to the presence of muon pairs or introduced noise.

Finally, when theta trigger analyses are performed, a different selection criteria can be adopted. The  $\theta$ -view of the trigger system, in fact, is not presently used by the data acquisition system, apart from the confirmation mechanism exploited to accept uncorrelated  $\phi$ -triggers. The request of the presence of a correlated trigger in the  $\phi$ -view, within the station under study, is therefore enough to ensure an unbiased  $\theta$ -trigger selection. This criteria can be also used to compute  $\theta$ -trigger efficiency without using the segment information, since the presence of a correlated  $\phi$ -trigger confirms the passage of the muon in the  $\theta$  SL.

The list of requests used to perform selections of the analyzed sample can be summarized as follows:

1. Coincidence, within a sector, of at least two trigger segments, at the same BX, in stations others than the one under investigation;
2. Presence of a 7/8 hits reconstructed segment with  $|\psi| \leq 30^\circ$  incident angle w.r.t. the perpendicular to the chamber;
3. Presence of, at most, 12 detected hits in the  $\phi$  SLs;
4. Presence of a correlated  $\phi$ -trigger (to carry out  $\theta$  trigger studies).

### 5.3 DT Local Trigger Performances

In ideal conditions the DT Local Trigger must provide precise estimation of the coordinates of a crossing particle and unambiguously identify its timing origin in terms of BX. As previously outlined the system is not designed to operate on cosmic data, therefore a slight worsening of its performances, with respect to the ones foreseen at the LHC, is expected.

In the following the analysis of the DT Local Trigger behaviour during the CRAFT exercise is reported. An overview of the system behaviour during

bunched beam tests can instead be found in [51, 52]. A way of making system synchronization using cosmic data (different than the one presented in [53]) is also described, together with a comparison between the outcomes of the trigger electronics and its software emulator code. When non explicitly mentioned, the results are obtained using a data sample collected with stable magnetic at 3.8 T.

### 5.3.1 BX Identification and Primitives Quality

The ability of the trigger to identify the crossing time of a particle and assign it to a precise BX is a fundamental requirement of the system. Unfortunately cosmic muons come asynchronous in time and the linear drift assumption required by the mean-timer computation (see 3.1.2) can produce BX mis-identification in case a particle crosses the chamber closed in time to the BX clock sampling. Moreover, uncertainties from approximate system synchronization can further worsen the situation. Perfect interlock between stations is, in fact, not achievable with cosmics because the wide range of possible particle trajectories expected in this case does not allow to unambiguously determine muons time-of-flight across the detector. Under these assumptions perfect BX identification is not presently foreseen.

The selection criteria described in 5.2.1 allow to determine the BX origin of a crossing particle within a single sector, reducing the effects due to synchronization problems and making BX identification studies possible. The “*expected*” BX used to evaluate the trigger performances is defined as the one where the coincidence of the (at least) two triggers requested for data selection has been found. The difference between this value and the one measured by the station under investigation, for the four stations of a sector, is shown in Fig. 5.6. Triggers belonging to different quality ranges are displayed separately. The peak referring to correct BX identification shows that good BX measuring is achieved in about 82% of cases when a HH trigger is found. In the case of lower trigger qualities, the determination of the trigger BX is less precise, as expected.

Another indication of the performances of the trigger is the quality of the trigger segments. An higher quality, in fact, implies the contribution of a higher number of cells in the primitive reconstruction, thus a better estimation of its parameters. Fig. 5.7 shows the quality distribution for segments reconstructed at the expected BX in the up-most sectors of the

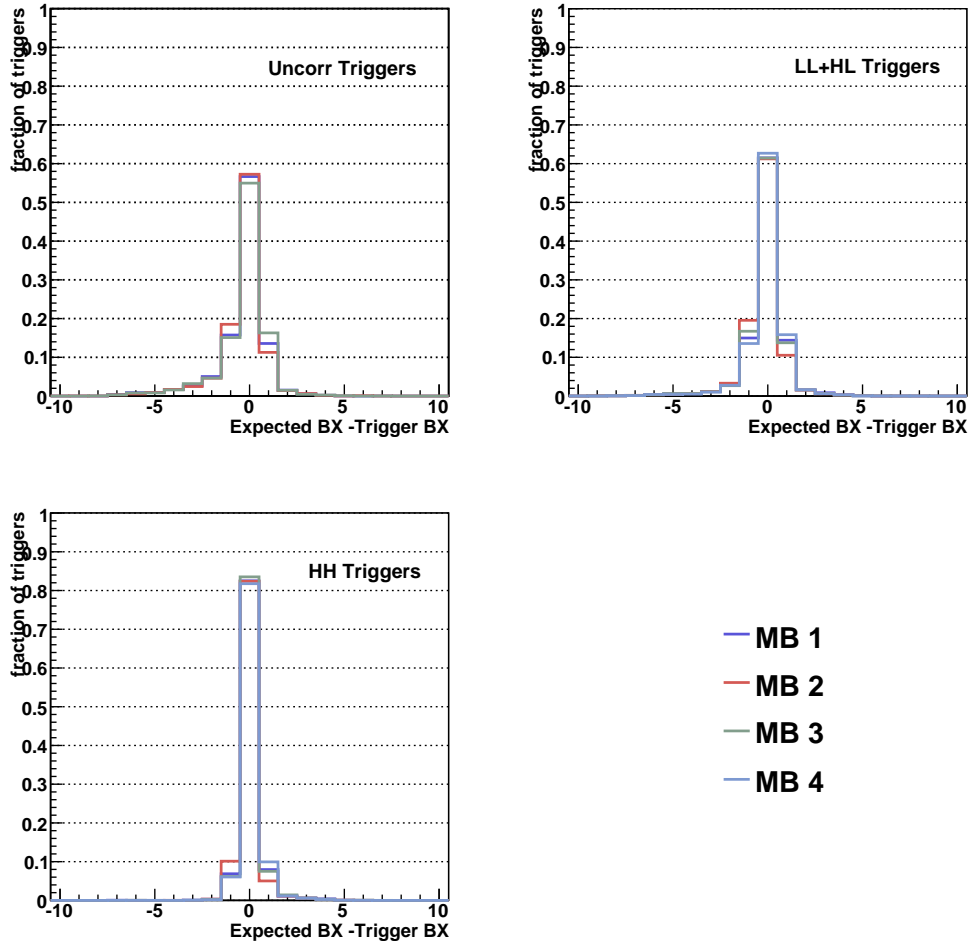


Figure 5.6: *BX* distribution for uncorrelated, *LL+HL* and *HH* triggers. Different colors refer to different station types.

DT system. The labelling used in the plots is in line with the one defined in Tab. 3.2. Differences among different types of stations are due to geometrical acceptance and illumination from cosmic. As can be seen the distribution is quite similar for the various sectors, the horizontal ones performing slightly better. This can be understood considering that cosmic rays come mostly along the vertical direction illuminating oblique sectors in angular ranges

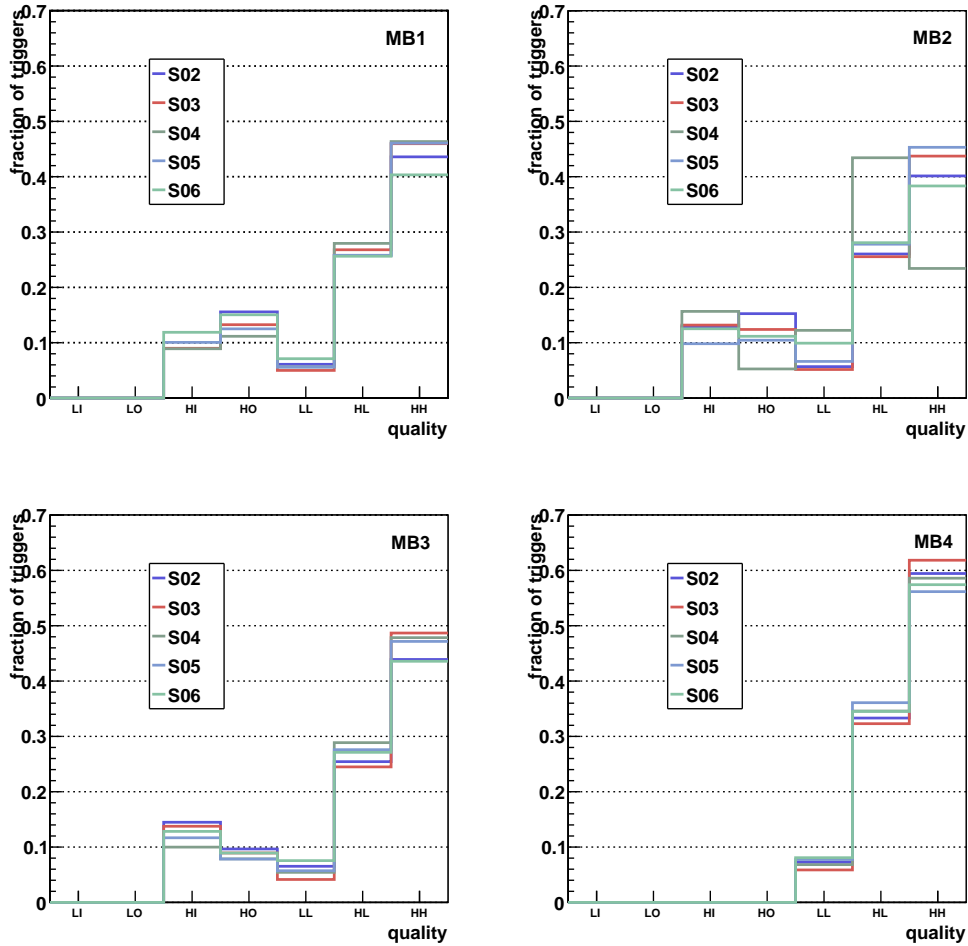


Figure 5.7: *Quality distribution of the correct BX triggers for the top sectors (S2/3/4/5/6) of a wheel. Different plots refers to different station types.*

where the system is not supposed to operate at its best. The absence of uncorrelated L triggers in the distribution is due to the special configuration conditions adopted for cosmic data-taking and the lack of H triggers in MB4 stations comes from the absence of the  $\theta$  SL in these chambers. This prevents the uncorrelated H trigger confirmation mechanism to be operated. The high fraction of HL triggers in the MB2 station of sector 4 is related to

a High Voltage (HV) problem during the run that forbade half a layer to function properly, thus reducing the expected HH trigger fraction, and is well understood.

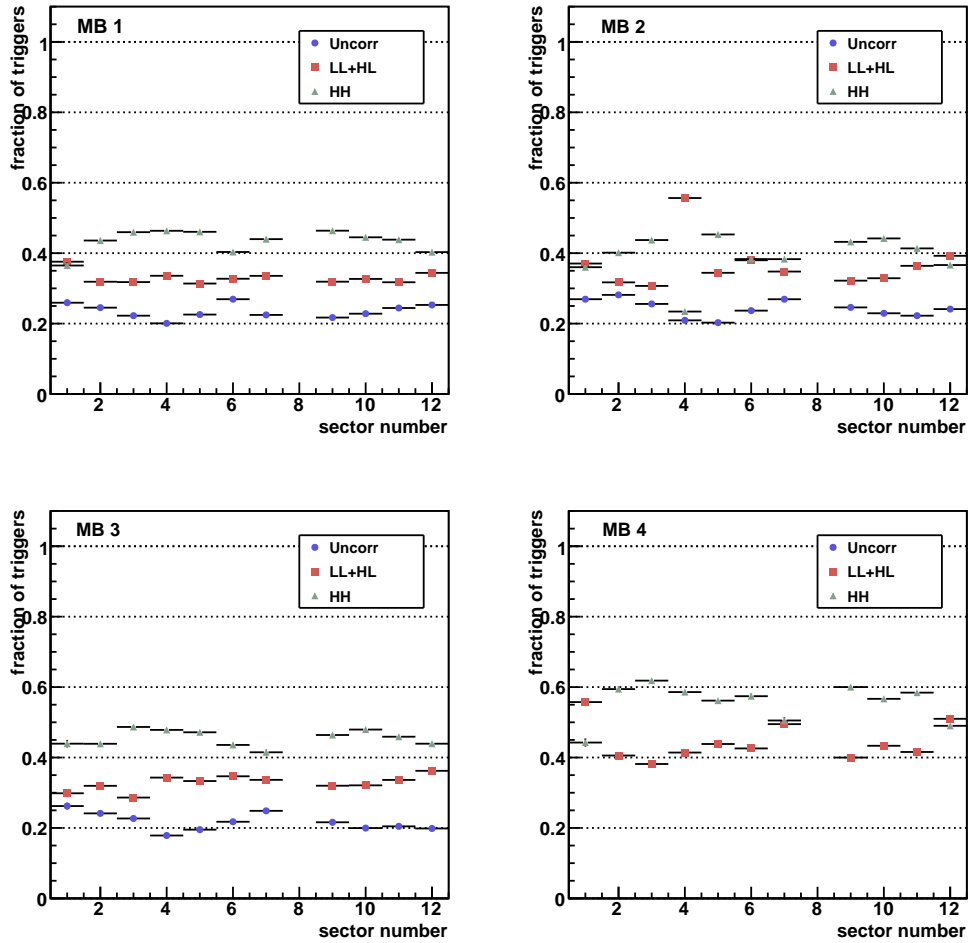


Figure 5.8: *Distribution of the fraction of uncorrelated, LL+HL and HH triggers at expected BX as a function of sector number. Different plots refer to different station types.*

Similar observations can be gathered from Fig. 5.8 where the fraction of uncorrelated, HH+HL, and HH triggers, detected at the expected BX, is

shown as a function of the DT sector number. Missing points are related to sectors that were not included in the readout during the run. The trend of HH and uncorrelated fraction clearly shows that the system performs better when tracks come in the angular range close to the perpendicular to the chamber (as expected in the case of high  $p_T$  LHC muons). The aforementioned HV problem is clearly visible also in this plot.

Taking into account the radial and bending angle information (respectively  $\phi$  and  $\phi_B$ ) delivered by the trigger is possible to perform quality studies to test the uniformity of the system response. The outcomes of such studies are reported in Fig 5.9 and 5.10 where the fraction of uncorrelated, LL+HL and HH triggers is shown as a function of the muon impact angle and position along the chamber. The plots are computed for the sector where the HV problem was found. In general, good uniformity with respect to position is found. Station boundaries where system is supposed to perform differently have been excluded from the computations. The regions of low HH efficiency in the MB4 are due to a group of masked cells and to the hole between the two chamber constituting the double MB4 station. The HV problem is clearly visible in MB2 where half a chamber is characterized by a very low fraction of HH triggers. A non null population of HH triggers in the zone is probably due to detection noise and is confirmed by data-emulator comparison studies (see 5.5). A noticeable dependence of the quality assignment with respect to the angular impact parameter is found in Fig. 5.10. In this case the absence of a plot for the MB3 station is due to the absence of bending angle information for these chambers at the readout level (see 3.2.4).

To fulfill the requests asked to the LHC physics program (described in 1.2), the DT Local Trigger system has to efficiently recognize muon pairs crossing one single chamber at the same BX. The expected rate of di-muon events is about 1% of the single muon rate. A ghost suppression mechanism able to reduce the presence of fake DT regional triggers (coming from multiple trigger segment produced by the passage of a single muon), below the level requested for efficient muon pair identification has thus to be provided.

Fig. 5.11 shows the fraction of events where a second trigger is delivered at the correct BX (for a sample where a single muon is expected) as a function of the sector number. MB1/2/3 stations have been proved to deliver similar fraction of second tracks, thus they have been grouped together in the plot. The uncorrelated trigger suppression, performed with the cosmic trigger configuration in MB4, leads to a reduced fraction of second segments,

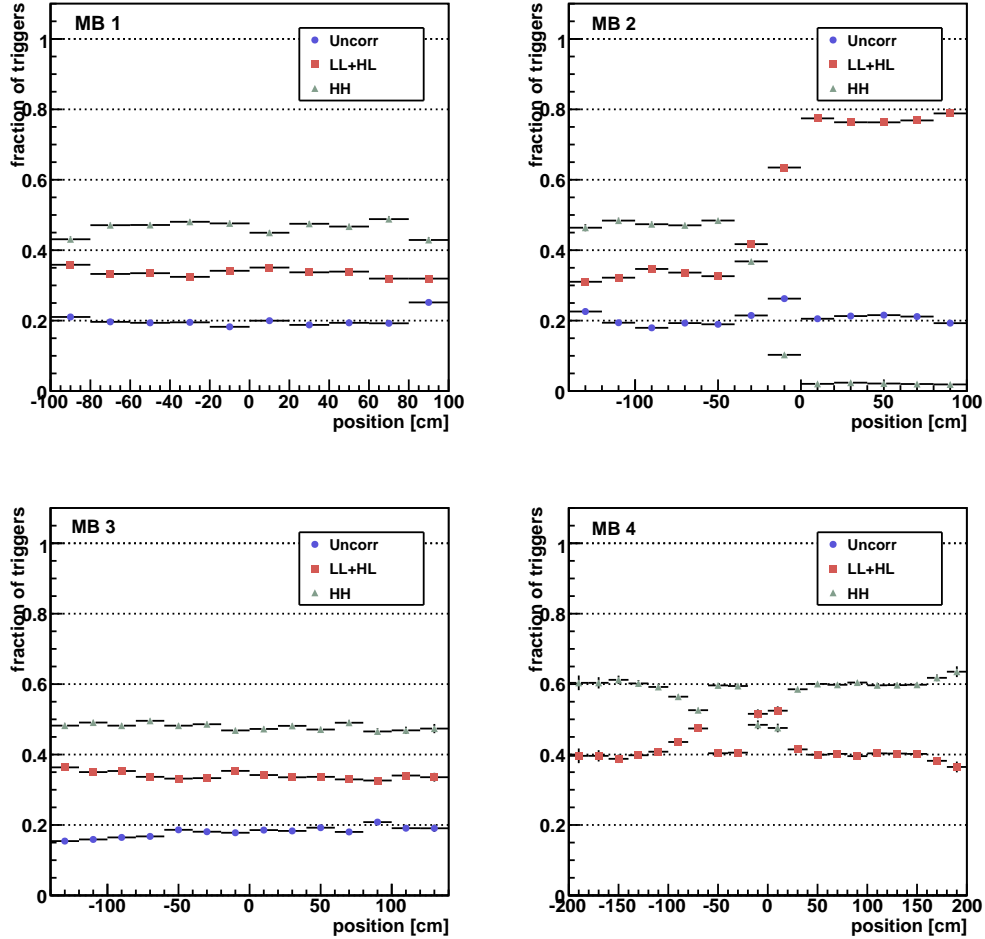


Figure 5.9: *Distribution of the fraction of uncorrelated, LL+HL and HH triggers at expected BX as a function of the trigger position along the chamber as measured by the trigger. Different plots refer to different station types.*

therefore results coming from these stations have been plotted separately. The fraction of second tracks is of the order of 3% for MB1/2/3 and 1.5% for MB4s. This is in line with previous analysis results and a negligible ghost track generation, at the regional trigger level, is expected from simulations if the PHTF is operated in closed LUT mode and an uniform distribution of

### 5.3 — DT Local Trigger Performances

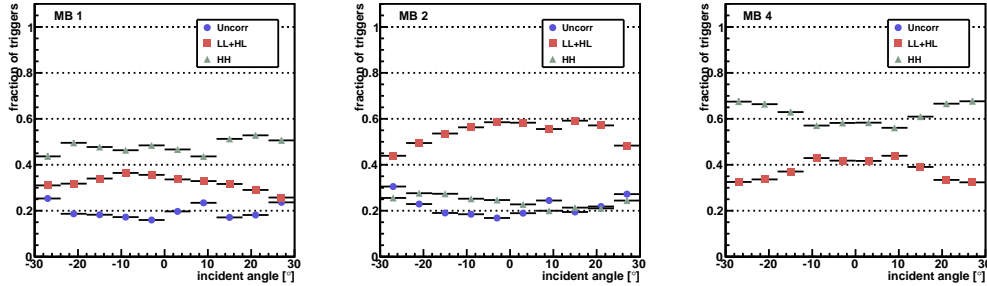


Figure 5.10: *Distribution of the fraction of uncorrelated, LL+HL and HH triggers at expected BX as a function of the muon impact angle as measured by the trigger. Different plots refer to different station types. Plots coming from MB3 stations are not showed because the system does not deliver MB3 direction measurements.*

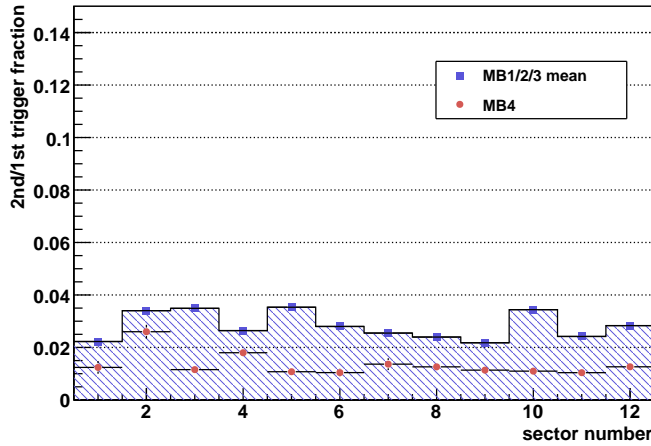


Figure 5.11: *Fraction of events where the system detects two trigger segments at the expected BX as a function of the sector number. MB1/2/3 stations behaves in the same way so their outcomes have been averaged in the plot.*

second tracks is found.

A study on the relationship between the quality of the first and second

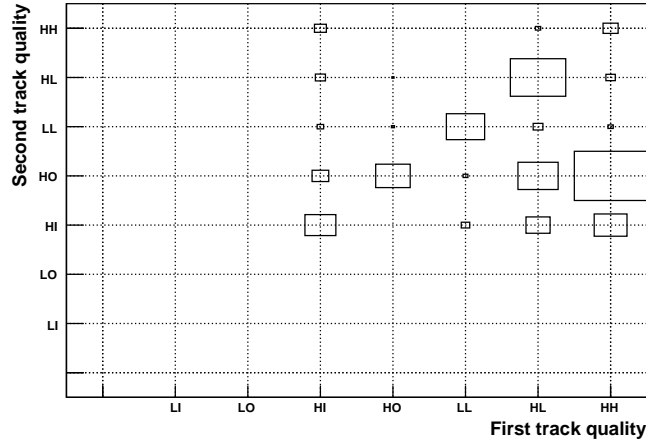


Figure 5.12: *Quality of second track segments as a function the quality of the first tracks for triggers at expected BX.*

tracks is shown in Fig. 5.12. The quality of the second segment is often equal or less than the one of first tracks. The rare exceptions are foreseen by the ghost suppression logic and are well understood. The diagonal band of the plot, corresponding to triggers of the same quality for first and second tracks is quite populated. The distribution of the difference of direction and position between first and second tracks shows how many of these trigger primitives are exact copies the one of the other. The result of this analysis is displayed in Fig. 5.13 . It proves that about 55% of these events are very likely to be exact copies of the first trigger segments that are not canceled by the ghost suppression mechanism. These events have been selected and a plot of their distribution along the chamber (depicted in Fig. 5.14) shows sharp peak pattern replicated with a step which matches the TRACO size. This proves that such kind of ghosts only come from special zones along the chamber. Moreover the quality distribution of these ghost primitives, depicted in Fig. 5.15, shows that a high fraction of these triggers is made of TRACO correlated segments, that are not supposed to be suppressed in the standard TS configuration.

Full information coming from the DT  $\theta$ -trigger is not presently delivered by the hardware. Moreover the  $\theta$ -view of the DT trigger system has not

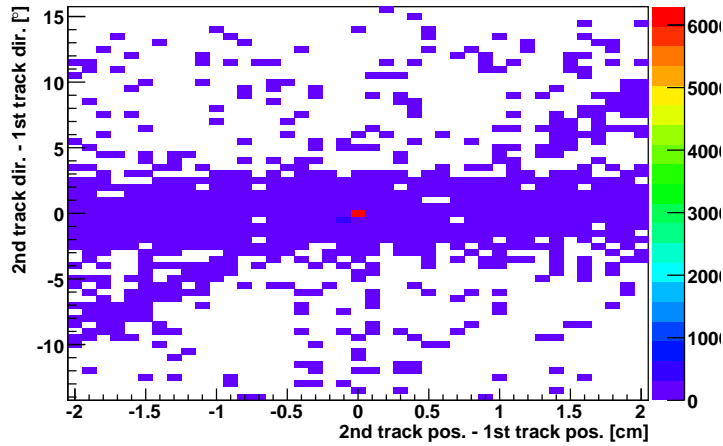


Figure 5.13: *Distribution of first - second track segment position and direction difference for triggers where the quality of the two segment is identical.*

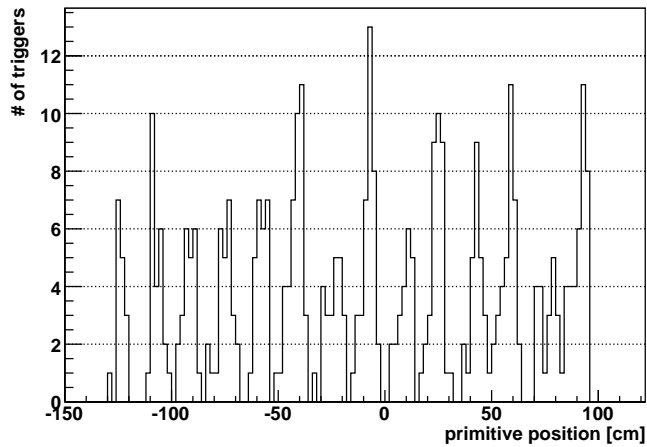


Figure 5.14: *Distribution of identical track copies as a function of the position along the chamber.*

been used at all in data taking, apart for the confirmation of uncorrelated H triggers performed at TRACO level. However partial information on the

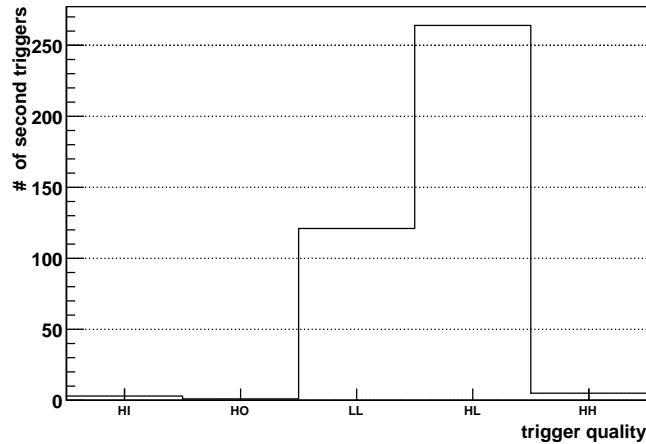


Figure 5.15: *Quality distribution of identical track copies.*

$\theta$ -trigger output coming from a dedicated readout infrastructure (used to debug the system during commissioning) was available.

As already said a simplified data selection criteria, was adopted to perform  $\theta$ -trigger studies. In fact, if a correlated  $\phi$ -trigger is found, the  $\theta$ -view of the trigger system is not taken into account at all during data acquisition, therefore no correlations are expected. Fig. 5.16 shows the BX assigned to a  $\theta$ -trigger as a function of its quality. The standard quality labelling is purely conventional in this case, in fact only LO and HO bins, representing L quality and H quality theta triggers are filled in the plot. As expected, in this case the BX identification ability of the system is rather poor. Among other things, this explains why bounds on trigger quality have been tightened to perform  $\phi$ -trigger selection with cosmics. Improvements are foreseen at the LHC, when muons from bunched interactions will cross DT chambers at a fixed latency.

The selection criteria based on the use of correlated  $\phi$ -triggers allows also to estimate the timing origin of the particle in terms of BX. The measurement of the fraction of events when a trigger is delivered, by the  $\theta$ -view of the system, at the BX expected by  $\phi$ -trigger selection is shown in Fig. 5.17. Efficiencies of the order of 60% and 84% are measured respectively for H triggers or triggers of any quality. The response of the system as a function of the

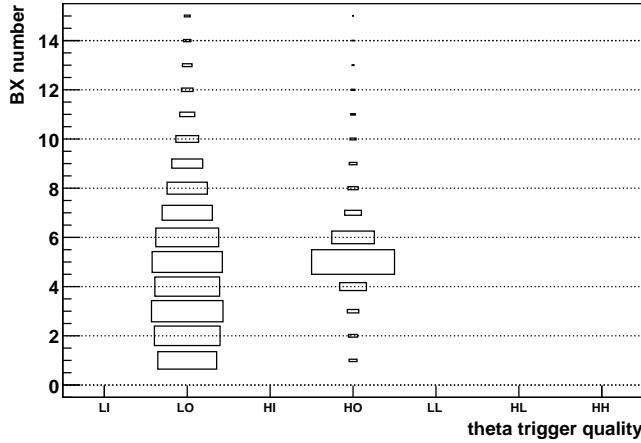


Figure 5.16: *BX* distribution for  $\theta$ -triggers as a function of the primitive quality.

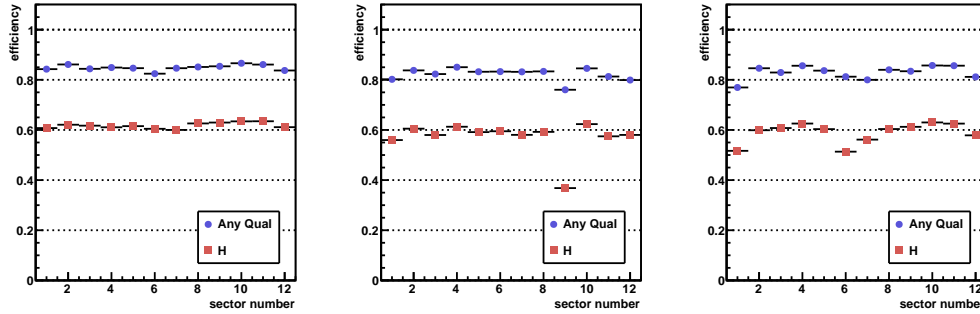


Figure 5.17: *Efficiency of BX identification of the  $\theta$ -trigger as a function of the sector number. Red squares and blue circles refers respectively to H triggers and any quality triggers.*

sector number is quite inhomogeneous especially in MB3 stations. However fluctuations are expected in this case because the low level of redundancy of the DT detector in  $\theta$ -view implies a higher sensitivity of the system to any sort of hardware problem (i.e. noisy or dead cells). Moreover cosmic

rays are poorly detected by the  $\theta$  SL of skew sectors because, in this case, particles can cross  $\theta$  cells along the wire direction, and the DT system does not perform properly in these conditions.

### 5.3.2 Comparison with Local Reconstruction

The track segments coming from the fitting algorithm used for offline reconstruction provide an accurate method to compute position and direction of incoming muons within the chamber. Thus they can be used to cross check the precision of the trigger  $\phi$  and  $\phi_B$  measurements as well as to check correctness of the TRACO LUTs. Fig. 5.18 shows the position along the chamber for tracks reconstructed with more than 4 hits as a function of the position delivered by correlated triggers. The top plot refers to MB1 type chambers and the bottom to MB2s. Data coming from sectors 3, 4 and 5 have been summed together as well as ones from all positive wheels (in black) and negative ones (in red), as the LUTs used by these stations are identical. Good correlation between primitives and reconstruction is observed. However a displacement of the correlation line of about 20 cm is clearly visible in the plot referring to MB2s of negative wheels.

More detailed studies performed using the emulator code (see 5.5) showed that this is due to an error in the LUTs computation for these kind of chambers. A measure of the trigger position resolution comes from the computation of the difference between the position information as delivered from trigger primitives and reconstructed segments. Results are shown in Fig 5.19. As in the previous case, only correlated triggers are used. The RMS of Gaussian fits performed on the residual distributions are of about 0.8 *mm* for MB1s and 1.0 *mm* for MB2s, in agreement with bunched beam tests [51].

The same studies have also been performed taking into account the radial direction of the incoming muon ( $\psi = \phi + \phi_B$ ) with respect to the perpendicular to the chamber. Results from this analysis are shown in Fig 5.20 where the  $\psi$  information (in radians) obtained from the reconstructed segment is plotted as a function of the one obtained by the trigger. A sharp correlation is observed also in this case. Residual plots have been computed as well and they are depicted in Fig. 5.21. Results from Gaussian fits on these distributions show that the resolution on the incident angle measurement for correlated triggers is of the order of 4 *mrad*, in line with what expected from 3.2.2 and measured during test beam studies [51].

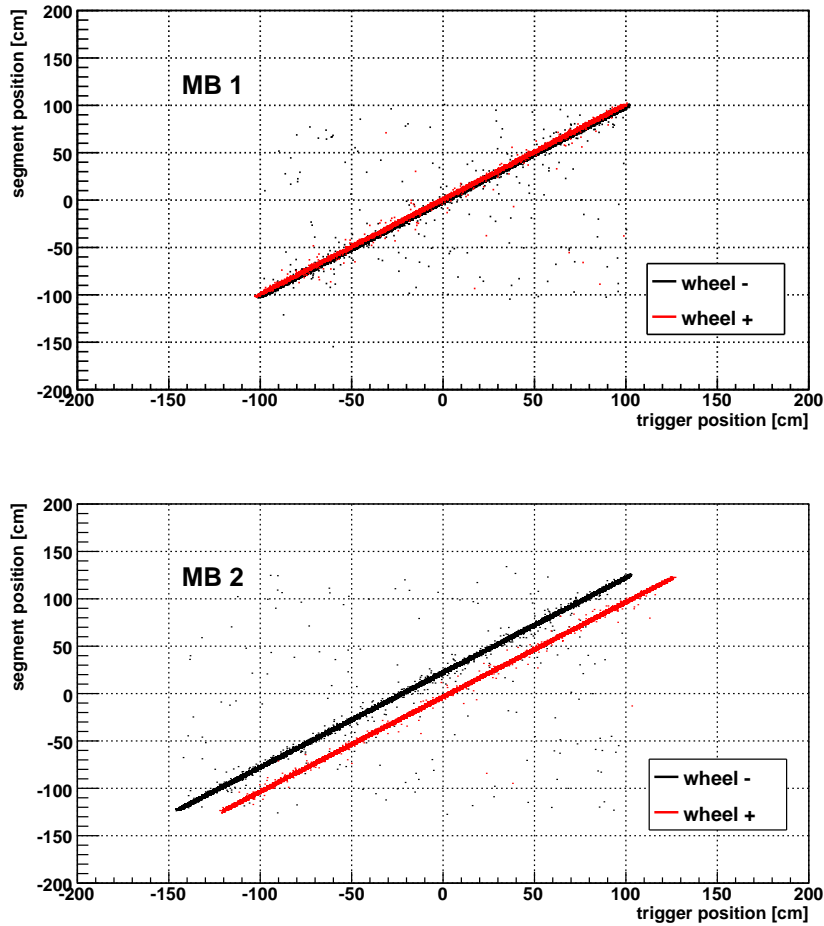


Figure 5.18: *Position measurement coming from reconstructed segments as a function of the same information computed using trigger primitives for MB1 (top) and MB2 (bottom) stations. Black points refer to negative wheels and red ones to positive ones.*

The presence of a reconstructed segment within a station is also used to perform trigger system efficiency measurements. The latter is defined as the fraction of events where the system delivered a primitive with respect to the events where a segment (satisfying the selection criteria described in 5.2.1) is

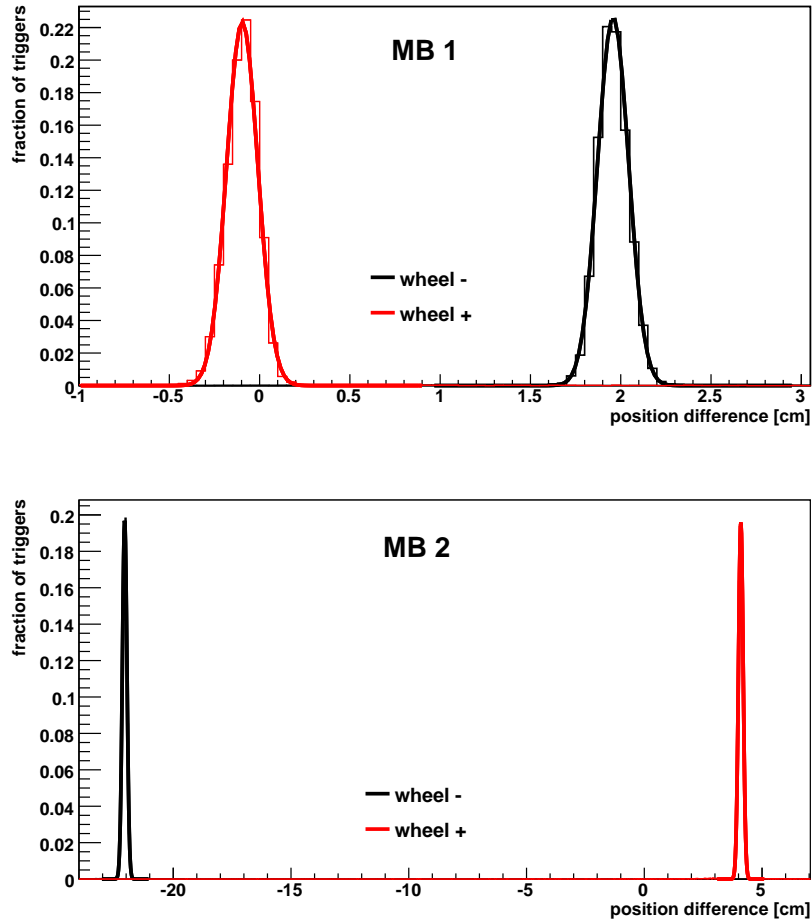


Figure 5.19: *Distribution of the difference between the position information as computed using reconstructed segments and trigger primitives for MB1 (top) and MB2 (bottom) stations. Black points refer to negative wheels and red ones to positive ones.*

found. More detailed efficiency studies can be computed separating triggers by quality.

Fig. 5.22 shows the mean efficiency within a station for various trigger quality ranges as a function of the triggering sector number. Efficiencies of

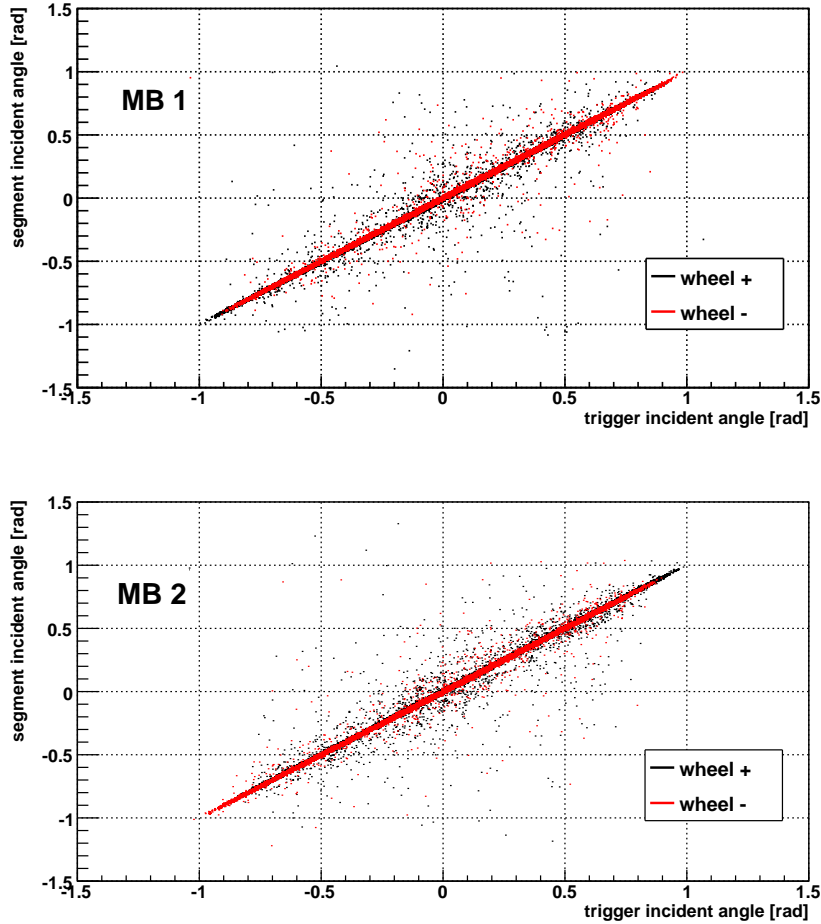


Figure 5.20: *Direction measurement coming from reconstructed segments as a function of the same information computed using trigger primitives for MB1 (top) and MB2 (bottom) stations. Black points refer to negative wheels and red ones to positive ones.*

about 95%, 80% and 50%, almost flat with respect to the sector are obtained for any quality, correlated and HH triggers respectively. The slight increment in performances for horizontal sectors observed in quality plots is not visible in performances for horizontal sectors observed in quality plots is not visible in this case because only muons coming in the  $\psi \leq 30^\circ$  angular range have

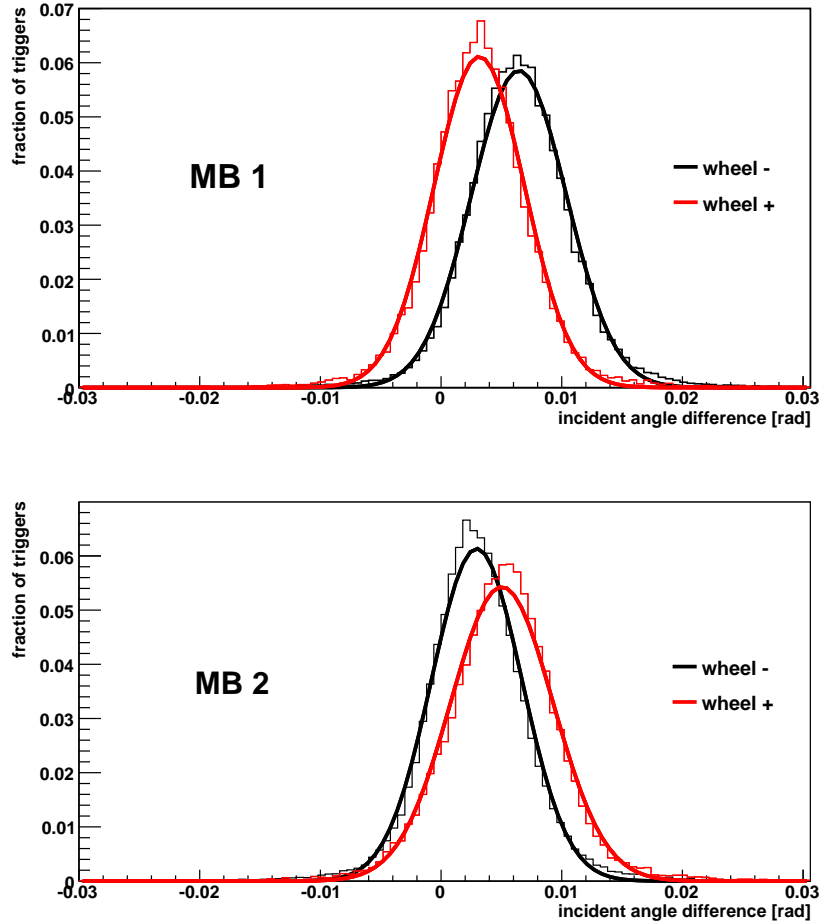


Figure 5.21: *Distribution of the difference between the direction information as computed using reconstructed segments and trigger primitives for MB1 (top) and MB2 (bottom) stations. Black points refer to negative wheels and red ones to positive ones.*

been selected for computations (as outlined in 5.2.1). An effect on HH trigger efficiency, due to the aforementioned HV problem is visible in the MB2 station of sector 4. However the lack of efficiency for HH triggers is almost completely recovered including all correlated trigger primitives. Inefficiencies in sectors

### 5.3 — DT Local Trigger Performances

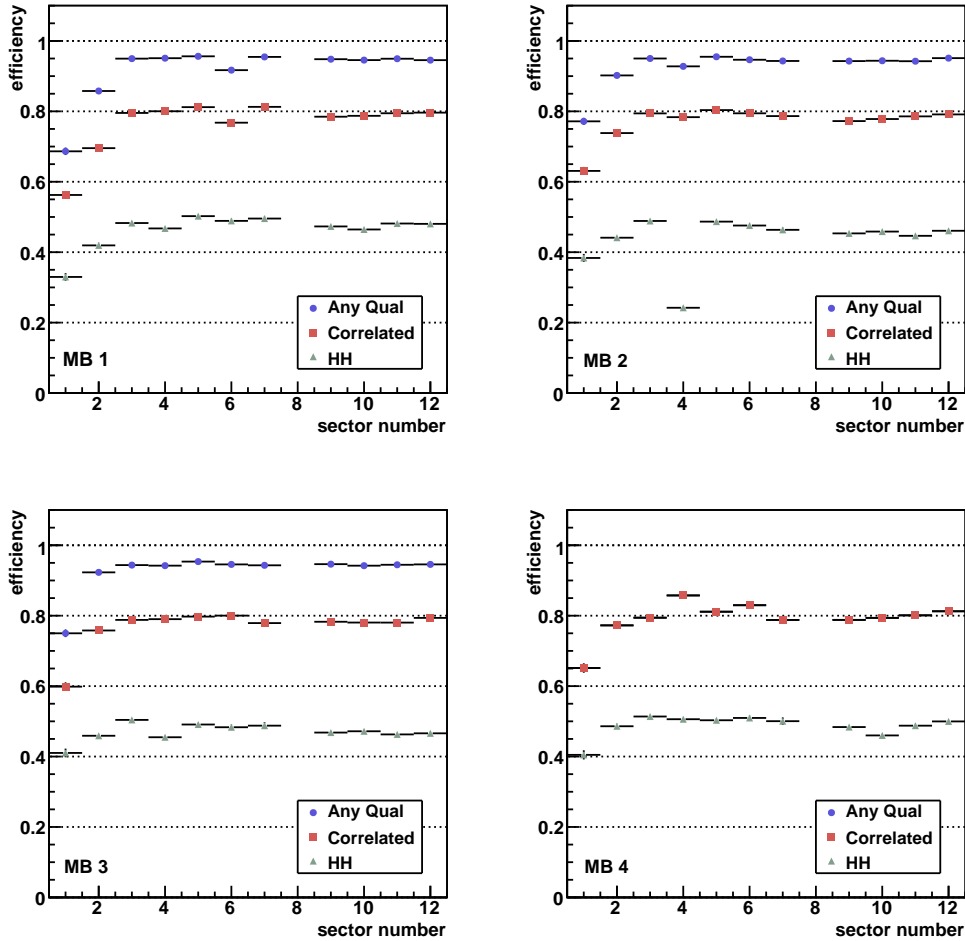


Figure 5.22: Mean trigger efficiency respect to reconstructed segments (for various trigger qualities) as a function of the sector number. Different plots refers to different kind of stations.

1 and 2 have been proved to be due to temporary readout problems. This effect is also visible in data-emulator comparison studies (see 5.5).

Tests to study the uniformity of the system response as a function of muon segment direction and position within a chamber were also performed. Figs. 5.23 and 5.24 show trigger efficiency as a function of these variables. Good

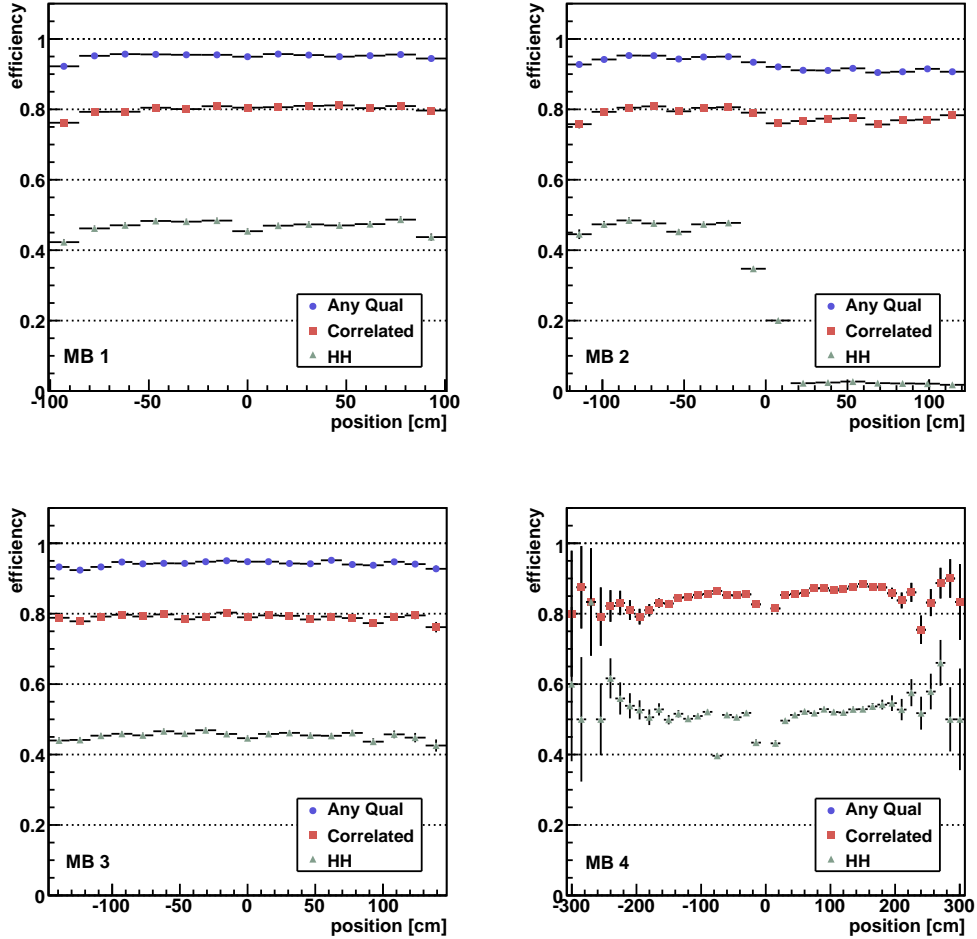


Figure 5.23: *Trigger efficiency respect to reconstructed segments (for various trigger qualities) as a function of the segment position along the chamber. Different plots refers to different kind of stations.*

uniformity with respect to position is found independently from the trigger quality. The HH quality efficiency is instead shown to slightly depend on the impact angle parameter  $\psi$ . The effect of the half missing layer is clearly visible and it slightly affects the efficiency of half of a chamber. In the region where the HV is not working, an HH null efficiency is in principle expected.

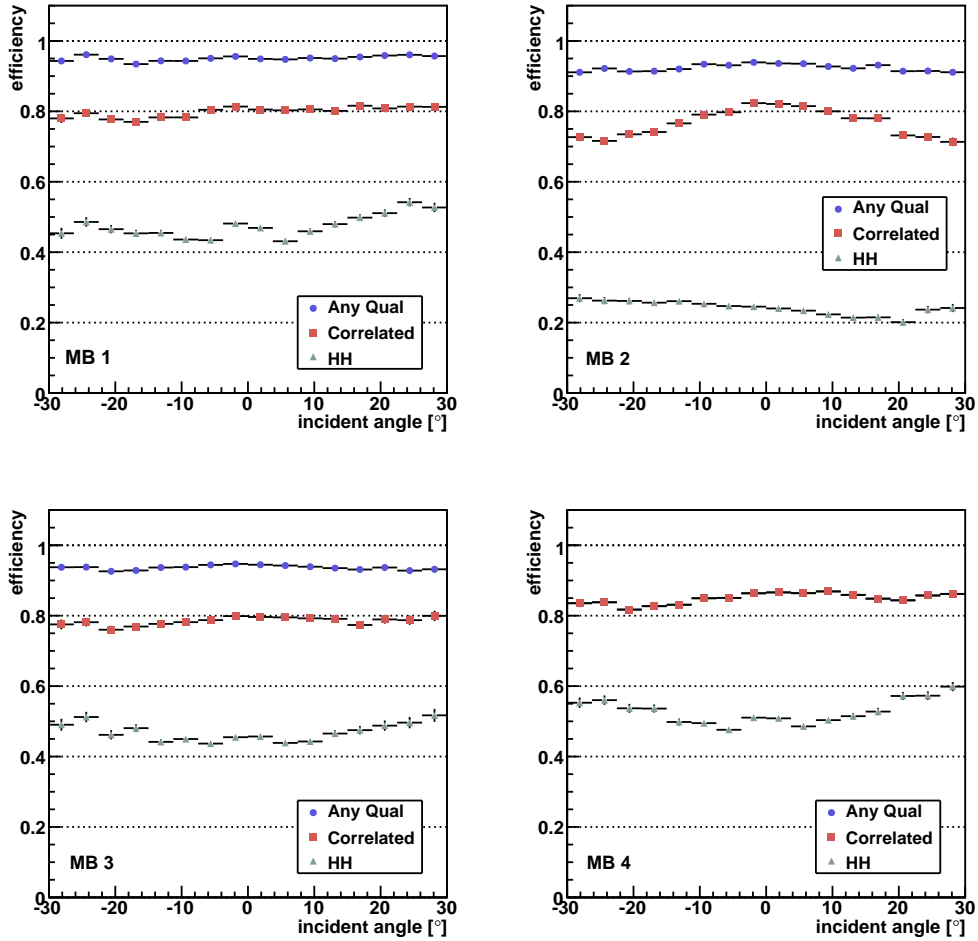


Figure 5.24: Trigger efficiency respect to reconstructed segments (for various trigger qualities) as a function of the muon radial direction. Different plots refers to different kind of stations.

The presence of a non null fraction of HH triggers in this part of the chamber is probably due to electronic noise and is well reproduced by the emulator (see 5.5). HH efficiency drops in MB4 are explained considering the spacing between double stations in sector 4 and the presence of a group of masked cells. The increasing error bars at the MB4 borders of the position related

plots come from a lack of statistics due to cosmic angular distribution and to the sample selection criteria.

MB4 efficiency seems to be slightly higher than the others, this is due to the fact that in MB4 uncorrelated triggers are not selected and, since both trigger and reconstruction computations are based on DT hits, a light correlation between them is present. This slightly modify the segment quality distribution, introducing a some bias in the efficiency estimation.

Track segment reconstruction was also used to measure the muon arrival time. In fact introducing a  $t_{0ev}$  offset (common among all cells) as an additional free parameter to be computed during the line fit minimization, it is possible to evaluate the time of passage of a particle with respect to the  $t_{Trig}$  time pedestal. This information is particularly important during cosmic ray studies. The asynchronous nature of cosmic muons in fact allows to perform a phase scan of the trigger performances as a function of the particle time of passage within a chamber. Efficiency computations as a function of  $t_{0ev}$  are shown in Fig. 5.25.

A clear downgrade of trigger efficiency is visible in regions roughly separated by 25 ns time intervals. The “any quality” efficiency is almost flat with respect to  $t_{0ev}$  but reconstruction of high quality (correlated or HH) triggers is highly inhibited in these timing regions. This is a known characteristic of the system, as the BTI segment reconstruction does not perform optimally on boundaries between BXs. Out of the optimal regions the fraction of generated L triggers is higher because one single cell hit may be more easily detected at a different clock sampling step (see 3.2.1). This also causes a reduction of the number of correlated segments at the TRACO level because the downgrade of BTI performances produces an higher fraction of wrongly reconstructed tracks, which decreases the possibility of matching between segments coming from the two SLs.

The timing position where “*worst performances*” are observed seems to be shifted for the MB4 stations. This can be explained considering that the absolute value of the  $t_{0ev}$  correction is related to the  $t_{Trig}$  estimation. Therefore differences in the time pedestals within a chamber can cause this kind of displacement. In the timing region where the trigger performs at its best the HH and correlated efficiency are found to be approximately 60% and 85%.

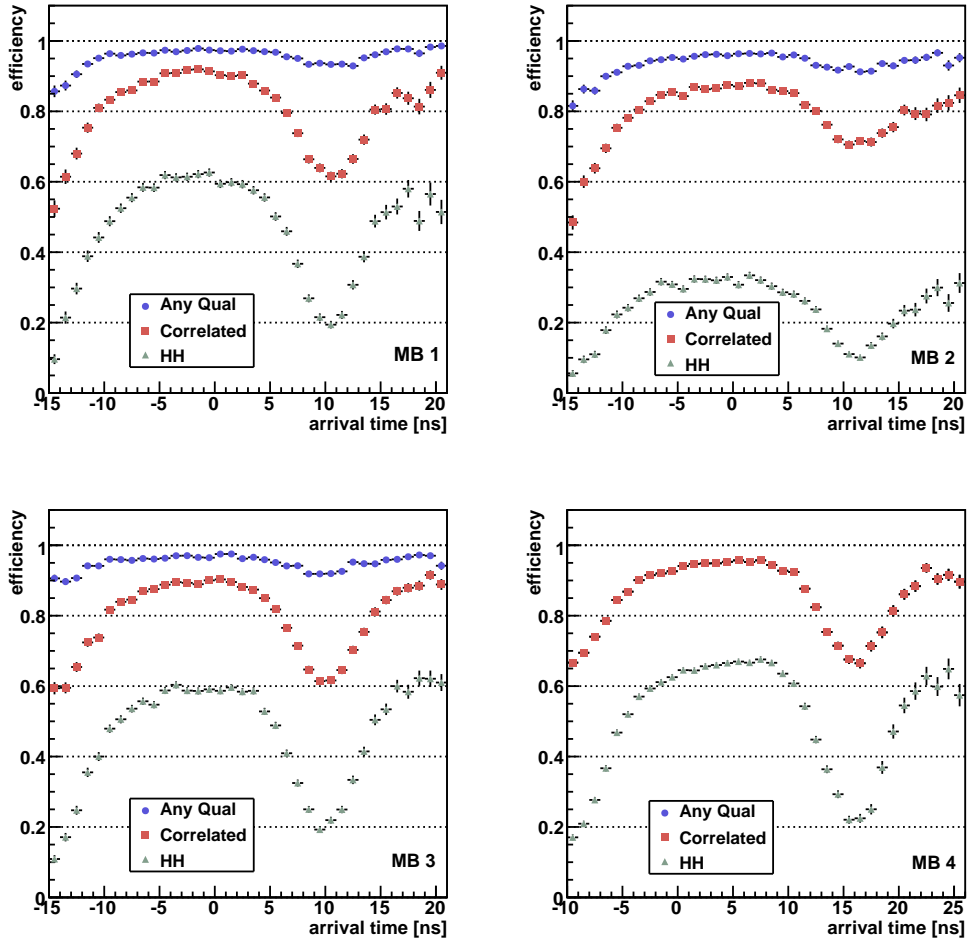


Figure 5.25: Trigger efficiency respect to reconstructed segments (for various trigger qualities) as a function of the  $t_{0ev}$  parameter. Different plots refers to different kind of stations.

### 5.3.3 Effects of the Magnetic Field

Up to now, all the presented results have been obtained using samples collected during CRAFT with a 3.8 T stable field. The same studies have been performed also using data collected in absence of magnetic field to evaluate

the system performances in these conditions.

The first effect which was studied is related to a possible shift in the BX assignment. Under magnetic field the drift path of the electrons along the cell is bent, therefore the particles cover a longer distance before reaching the anode wire. This results in an apparent reduction of the  $v_d$  parameter.

To measure how this can affect the trigger BX assignment, the means of the BX distributions within a chamber, computed in case of presence and absence of the magnetic field, have been subtracted the one to the other to look for possible displacements. Results, aligned with respect to the shifts found in MB4s (where the residual magnetic field effect is expected to be small) are shown in Fig. 5.26. As can be seen, an offset of about 2 ns is found for the MB1s of the outermost wheels. However differences are small, and of the order of system synchronization uncertainties. Therefore no significant downgrade due to an increment in BX mis-identification is found in this scenario.

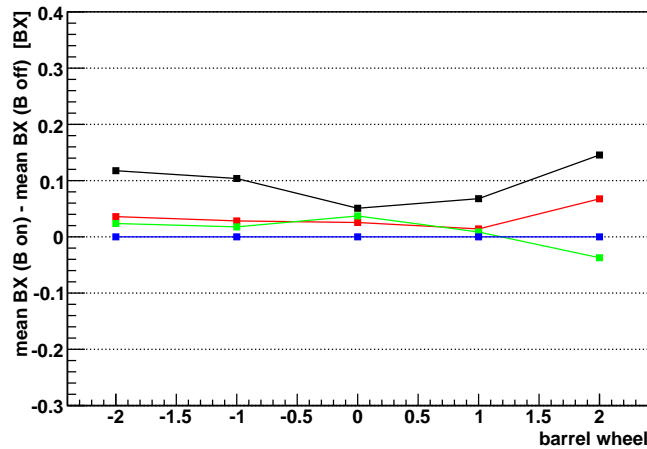


Figure 5.26: *Difference between the mean BX value within a station in case of presence and absence of magnetic field as a function of the wheel number. Data from different sectors has been summed together and the differences are computed respect to those obtained in MB4 stations.*

Effects related to a possible downgrade of the trigger resolution in  $\phi$  and  $\phi_B$  measurements have also been studied. Fig. 5.27 shows the residual

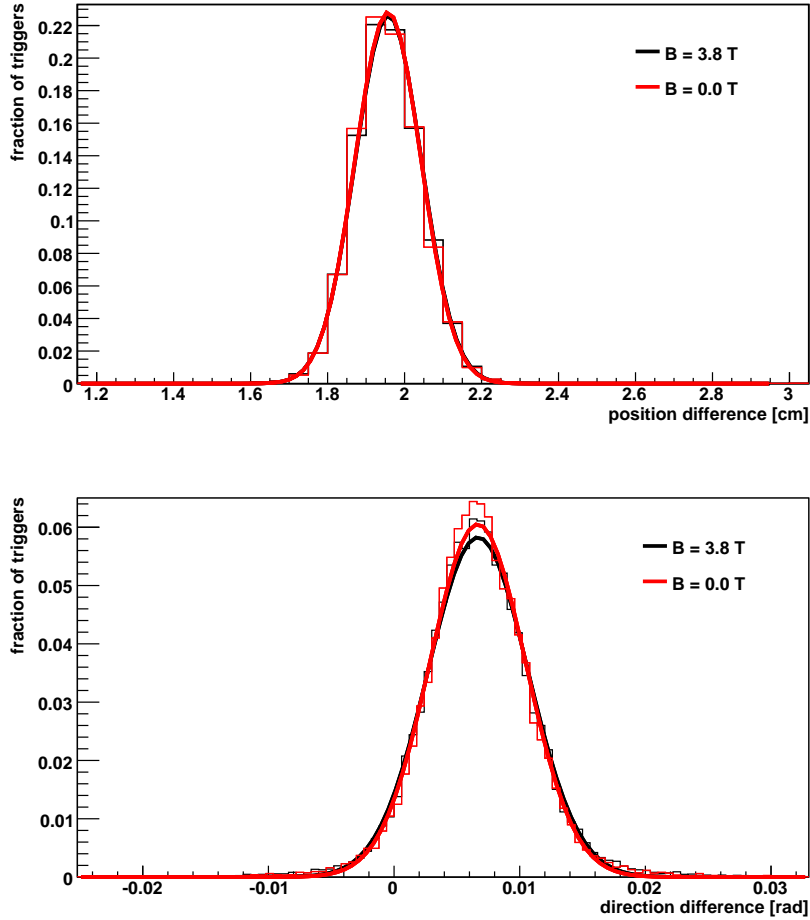


Figure 5.27: *Position (top) and direction (bottom) residual plots computed comparing trigger and local reconstruction information. Black and red lines shows the system behaviour when magnetic field is respectively 3.8 and 0 Tesla.*

distribution of trigger position (top) and direction (bottom) with respect to reconstructed track segments. Results have been obtained using correlated triggers found in MB1 stations of wheel -2 (where the residual field is expected to be higher than in the rest of the barrel). Black lines refer to the case where

Information	B Field	Fit Mean	Fir RMS
Position [cm]	3.8 T	2.0	0.09
Position [cm]	0 T	2.0	0.09
Direction [mrad]	3.8 T	6.7	3.9
Direction [mrad]	0 T	6.7	3.8

Table 5.1: Results of the fits performed on the plots of Fig. 5.27.

magnetic field was on and red lines to the one where no field was present. Table 5.1 shows the mean and RMS of the Gaussian fits for the two cases. The fact that the means of the distributions are not centered around zero comes from errors in the LUTs generation. No effect coming from the presence of the magnetic field is observed.

Finally studies concerning quality assignment and trigger efficiency have been carried out. Fig 5.28 and 5.29 show respectively the quality distribution within a sector and the efficiency as a function of position within a chamber with and without magnetic field. A small increment in performances is observed in case of absence of magnetic field. However as in previous comparison this effect is negligible and does not affect the overall trigger performances with cosmics.

## 5.4 Synchronization Studies

As previously outlined, the use of cosmic muons, together with the  $t_{0ev}$  computation, allows to perform a phase scan of the trigger efficiency as a function of the muon arrival time. In this scenario, it is possible to recognize the timing region, within a BX, where the system performs at its best. This information, among other things, can be used to develop a mechanism to synchronize the DT Local Trigger system.

Up to now, a strategy based on a “brute-force” scan of the performance of every single chamber, as a function of the fine-delay parameter used to perform synchronization, has been developed. A description of the possible algorithms to be operated in this scenario is given in [53]. All of them are based on the fact that muons coming from bunched  $p$ - $p$  collisions cross a single station in a timing region located at a fixed latency with respect to

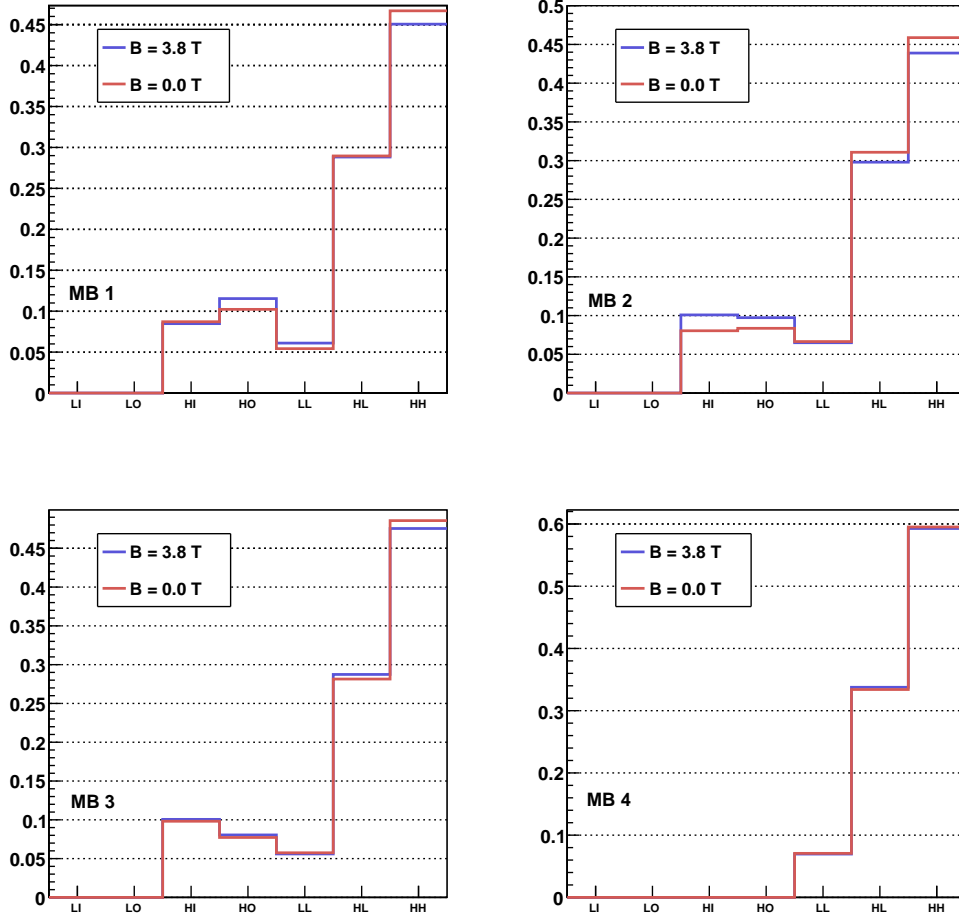


Figure 5.28: Trigger quality distribution for the different stations of a sector. Blue and red lines refer respectively to 3.8 and 0 Tesla magnetic field conditions

the bunch crossing time. The observables generated by these algorithms are thus sensitive to variations of the fine-delay parameter, and the best timing configuration can be found looking at them.

Cosmic muons, instead, come uniformly distributed in time but getting advantage of the  $t_{0ev}$  computation is still possible measure the moment of

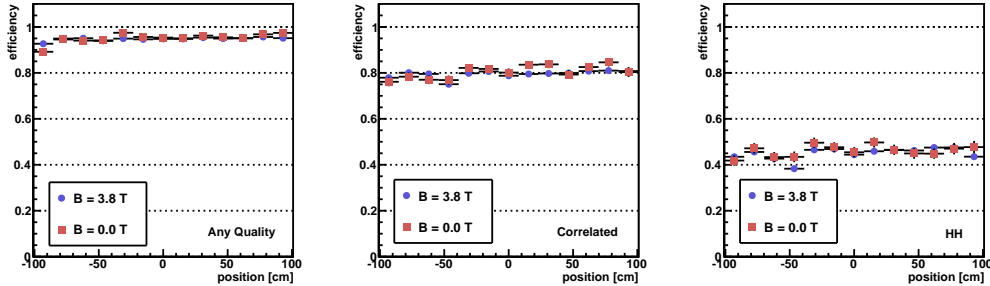


Figure 5.29: *Trigger efficiency respect to reconstructed segments as a function of the position along the chamber. Different plots refer to different trigger qualities and different colors refers do 3.8 and 0 Tesla magnetic field conditions.*

crossing of a single particle within a station. Therefore the  $t_{0ev}$  and the  $t_{Trig}$  timing parameters can be conveniently summed to evaluate the exact phase with respect to the bunch crossing timing, where the trigger system performs at its best. Upon uniform machine clock distribution by the Trigger and Timing Control system (TTC) the

$$t_{phase} = MOD(t_{Trig} + t_{0ev} + t_{fd}, t_{BX}) \quad (5.1)$$

formula measures timing position within the BX ( $t_{phase}$ ) of each single triggering station (apart from a global phase offset common to the whole detector). In the above computation  $t_{fd}$  is the delay adjustment parameter used to synchronize the system and  $t_{BX}$  is the time interval between two consecutive bunch crossings (25 ns). The inverse of the HH efficiency previously defined, plotted as a function of  $t_{phase}$ , can be used to measure the “worst” working point of the system. The region of best functioning can then be identified shifting by half a BX from that point.

Fig. 5.30 shows the inverse of the HH efficiency for different sectors. All the fine synchronization parameters  $t_{fd}$  were set to 0 during CRAFT, therefore all the stations of the same type are expected to perform similarly. The peak located at about 13 ns refers to the working point where the station performs at its worst. As expected, peaks measured in the same kind of station, for different sectors, results quite similar (independently from the  $t_{Trig}$  values used for the computation), proving the reliability of the method.

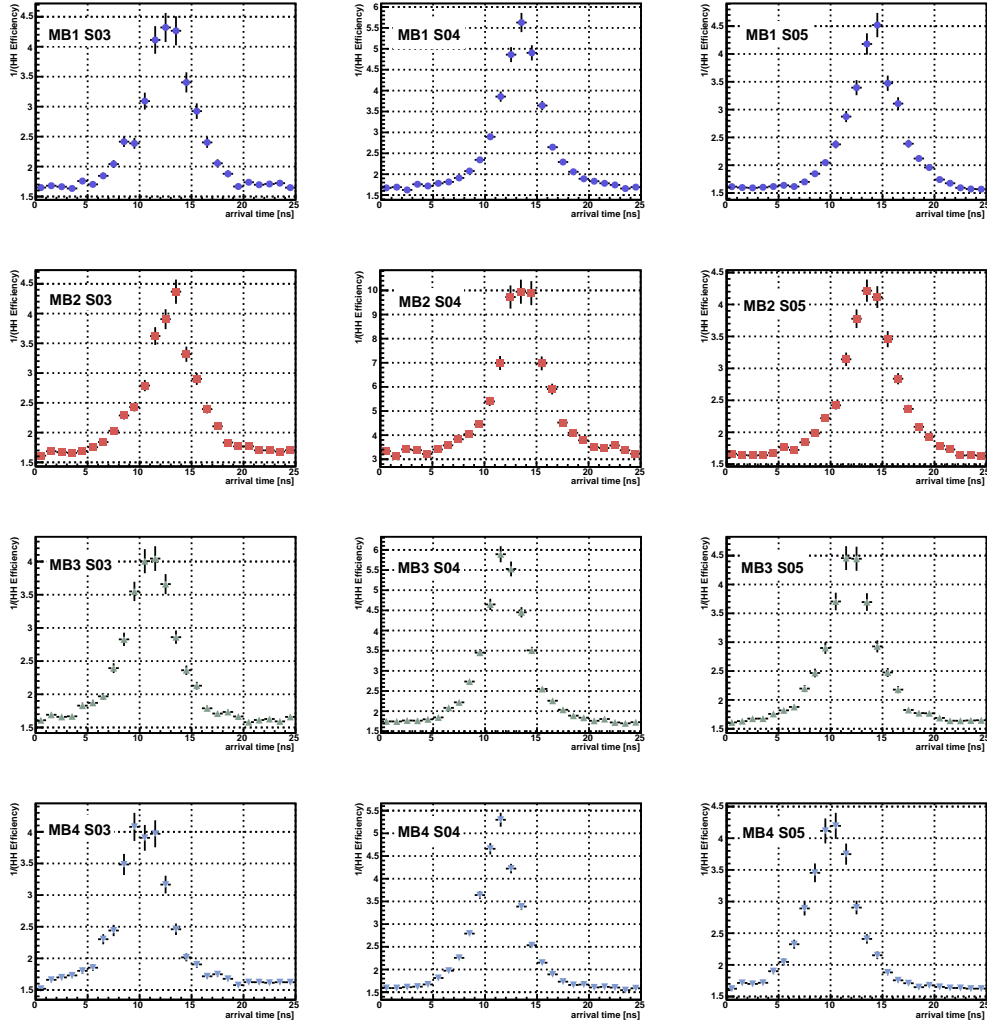


Figure 5.30: *Inverse of the HH efficiency computed for various sectors and stations as a function of  $t_{\text{phase}}$ .*

Fig. 5.31 shows the same ratio computation performed taking into account tracks crossing the chamber at different impact angles. Performing a fit with a Gaussian plus a constant term it is possible to measure the position and width of the peak. As outlined in Table 5.2 the results of the fit show

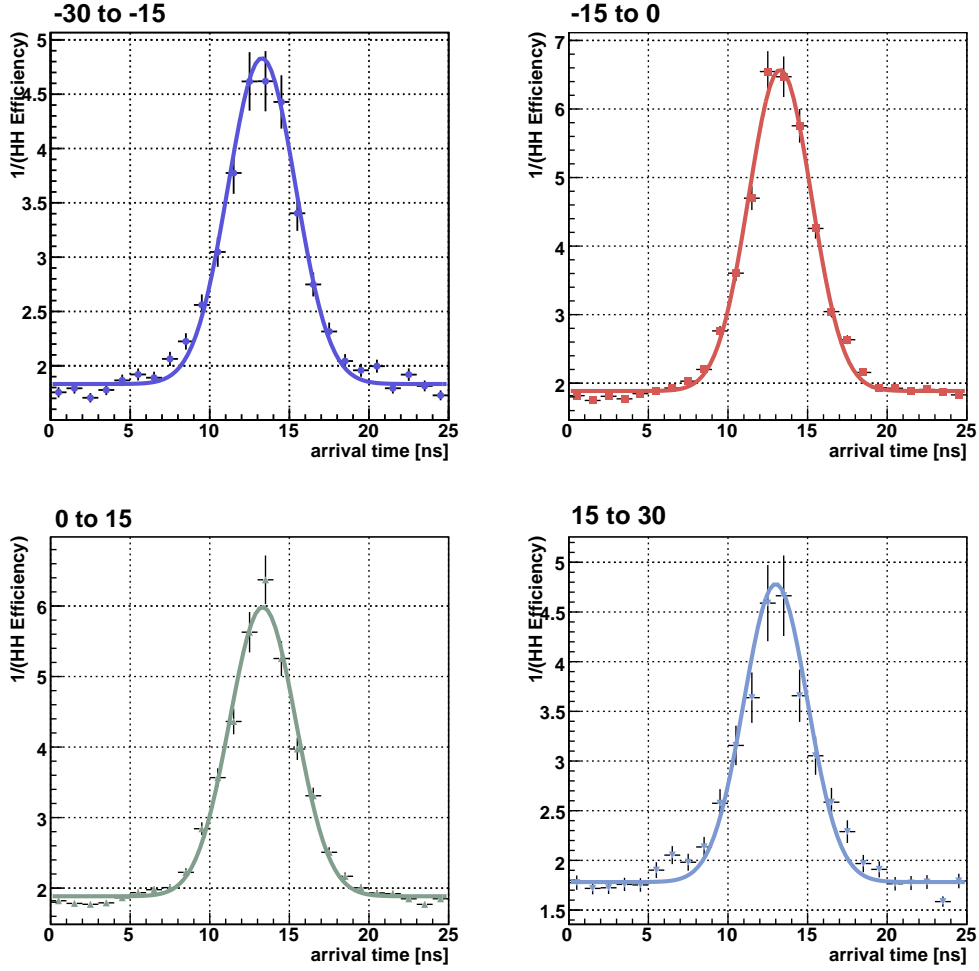


Figure 5.31: *Inverse of the HH efficiency computed for various impact angle ranges (within a single station) as a function of  $t_{phase}$ .*

that these values are quite insensitive to the muon impact angle. This ensures that measurements can be reliably performed, using cosmic rays, even in oblique sectors.

To study how the presence of the magnetic field downgrade the ability to identify the peak, comparisons between runs with and without field have been performed. Fig. 5.32 and Table 5.3 show the outcome of the study for

Angle range	Fit Mean [ns]	Fir RMS [ns]
-30° to -15°	13.3	2.1
-15° to 0°	13.3	2.0
0° to 15°	13.3	2.1
15° to 30°	13.0	2.0

Table 5.2: Results from the fits performed on the plots of Fig. 5.31.

B Field [T]	Station	Fit Mean [ns]	Fir RMS [ns]
3.8	MB1	13.8	2.4
0	MB1	13.9	2.4
3.8	MB2	13.3	2.3
0	MB2	13.2	2.1
3.8	MB3	11.7	2.0
0	MB3	11.9	2.3
3.8	MB4	11.9	2.3
0	MB4	11.9	2.2

Table 5.3: Results from the fits performed on the plots of Fig. 5.32.

the four station of a single sector. The peak RMS is stable and of the order of 2.3 ns proving that the “good performances” plateau is about 16 ns wide, and almost independent from magnetic field conditions.

As soon as bunched data will be available, the number of locally reconstructed segments as a function of  $t_{phase}$  is expected to be confined in the timing region where most of the muons coming from the impact point crosses the investigated station. The difference between the mean of this distribution and the peak characterizing the “worst” working point obtained with cosmics can thus be adjusted to ensure optimal trigger performances.

## 5.5 Comparison with the Emulator

A comparison of the performances of the trigger electronics with respect to the outcome of the emulator code presented in 4.1 has also been carried out. The study of the statistical matching between the two has already been

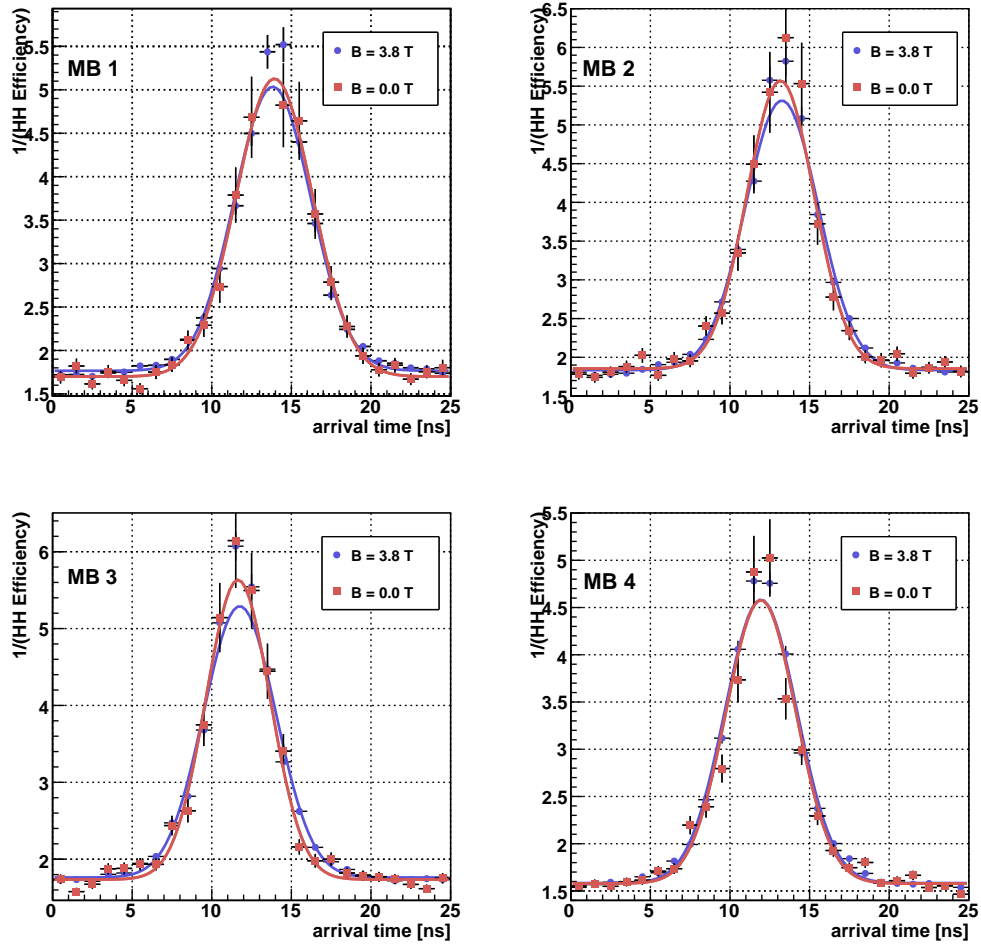


Figure 5.32: *Inverse of the HH efficiency within a sector as a function of  $t_{phase}$ . Results in presence and absence of the magnetic field are shown.*

performed elsewhere [51, 52], however a detailed analysis on this topic is still interesting both to validate recent software code changes 4.1 and to operate hardware commissioning.

A preliminary synchronization between the two systems is mandatory in order to obtain good matching. This is due to the fact that the emulator code receives in input digitized information coming from the detector readout

while the real BTIs sample discriminated signals directly on the on-board electronics. Therefore a fine subtraction of the time pedestals included in the readout digis is needed to make hardware and emulator operate in similar conditions. A first observation coming from statistical comparison of the efficiency, as a function of  $t_{0ev}$ , for the two subsystems, allows to verify that time pedestals have been properly subtracted. Fig 5.33 shows the outcome of this test for a single station on the basis of efficiency computed using triggers of various qualities ranges. A good correspondence between data and emulator is observed.

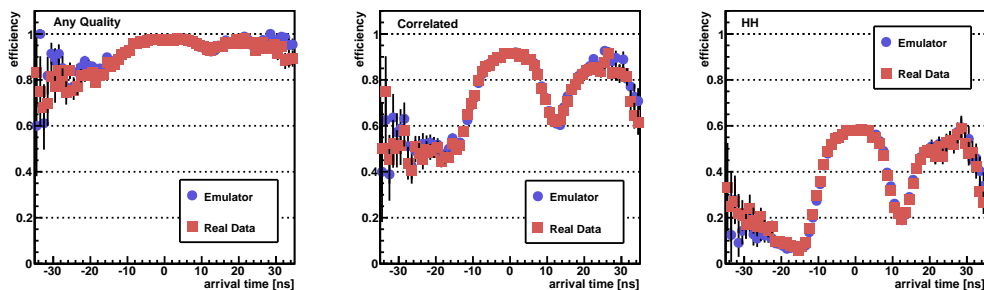


Figure 5.33: *Trigger efficiency respect to reconstructed segments as a function of the  $t_{0ev}$  parameter for real data and emulator. Different plots refers to efficiencies computed using triggers of different qualities.*

Good statistical matching is also observed in Fig. 5.34 where the quality distributions for emulator and hardware are shown for the four stations of a sector. Fig. 5.35 instead shows the event by event correlation between the quality information as obtained by hardware and emulator for the station where the synchronization has been checked. As can be seen a 100% matching is not achieved, however a correspondence of about 87% is found.

This is due to differences between emulator and real trigger BTI input rather than to problems in the sorting logic <sup>1</sup>. As an example it is impossible to operate wire by wire time pedestals subtraction with perfect accuracy. Moreover small differences are expected between the analog information seen

<sup>1</sup> In fact many parts of the emulator code have been tested to perfectly match the hardware system, upon injection of some million of test patterns configurations, during the trigger electronics development phase.

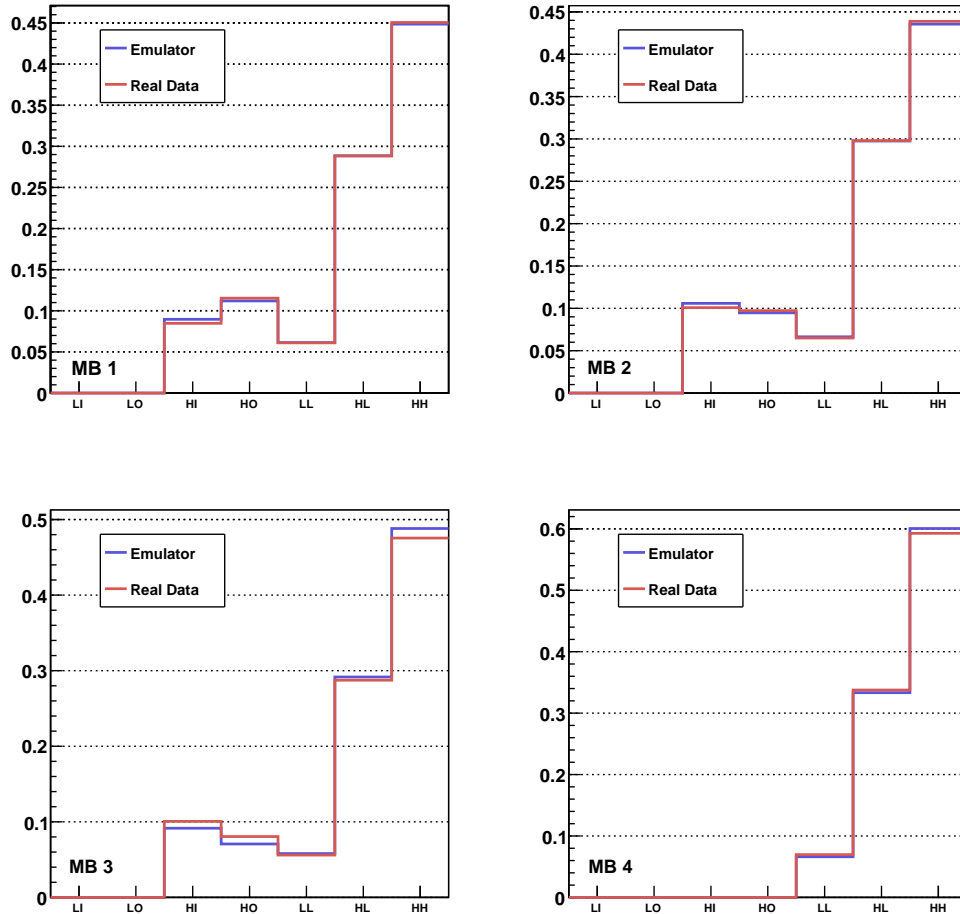


Figure 5.34: *Quality distribution for the various station of a sector. Results form real data (red) are compared with emulator outcome (blue)*

by the hardware BTI and the digitized information used by the emulator. This forbids to start the trigger processing in identical conditions for hardware and software and makes perfect matching impossible. Despite this, statistical studies still allow to correctly spot many problems<sup>2</sup>.

<sup>2</sup>Some improvements are expected at LHC when trigger synchronization on bunched

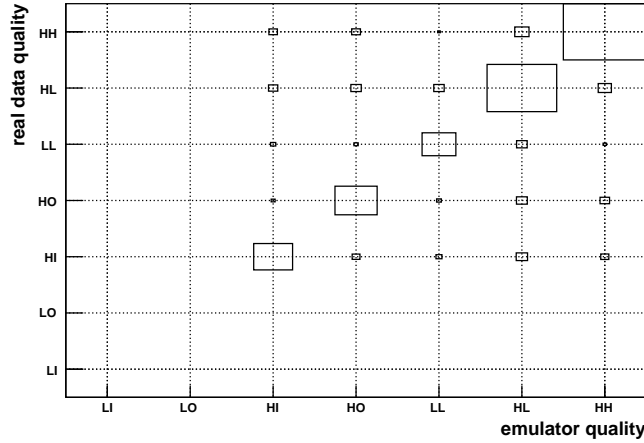


Figure 5.35: Real data trigger quality as a function of emulator outcome for a properly synchronized station.

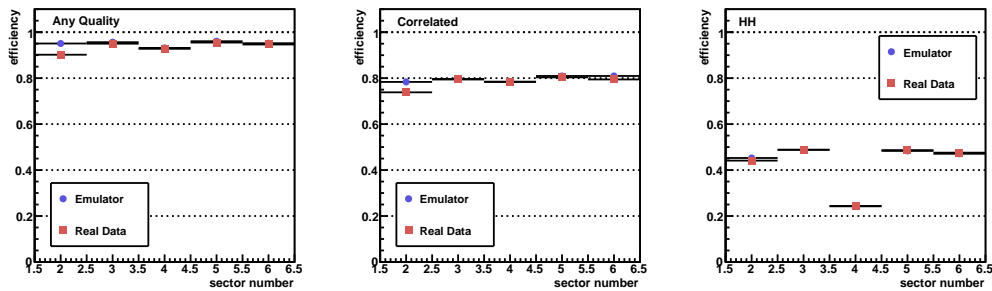


Figure 5.36: Mean trigger efficiency within a station respect to reconstructed segments as a function of sector number for real data and emulator. Different plots refers to efficiencies computed using triggers of different qualities.

Fig. 5.36 shows the mean trigger efficiency for MB2 type chambers of the five top sectors of a wheel measured using hardware and emulated data. As expected, very good matching is found for many of them. Mismatches are

data will be performed. In any case perfect event-by-event matching is not expected even in this case.

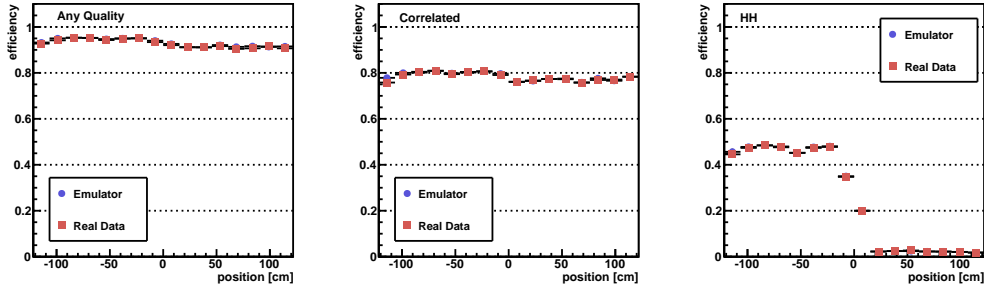


Figure 5.37: *Trigger efficiency respect to reconstructed segments as a function of the position along the chamber for real data and emulator. Different plots refers to efficiencies computed using triggers of different qualities.*

evident in sector 2 and further investigations of the problem allowed to spot inconsistencies in the readout information delivered by the system during the processed run. On the contrary problems due to misbehaviours of the DT detection system are correctly emulated by the software. This allows to verify that, in such cases, the error is not coming from the trigger. As an example Fig. 5.37 shows the comparison of real and emulated efficiency as a function of the position along the chamber. The HH trigger inefficiency mentioned in the previous section is reproduced by the emulator with high accuracy, as it is not due to a trigger problem.

Information	Info Source	Fit Mean	Fir RMS
Position [cm]	real data	4.1	0.09
Position [cm]	emulator	-0.1	0.08
Impact Angle [mrad]	real data	-5	5
Impact Angle [mrad]	emulator	-2	4

Table 5.4: *Outcome from the fits performed on the plots of Fig. 5.38.*

Another possible use of the emulator on real data is in the testing of the correctness of the LUTs used by the hardware. Comparison between trigger output and offline reconstruction (computed as in 5.3) are shown in Fig. 5.38. Position (top) and direction (bottom) plots for MB2s of posi-

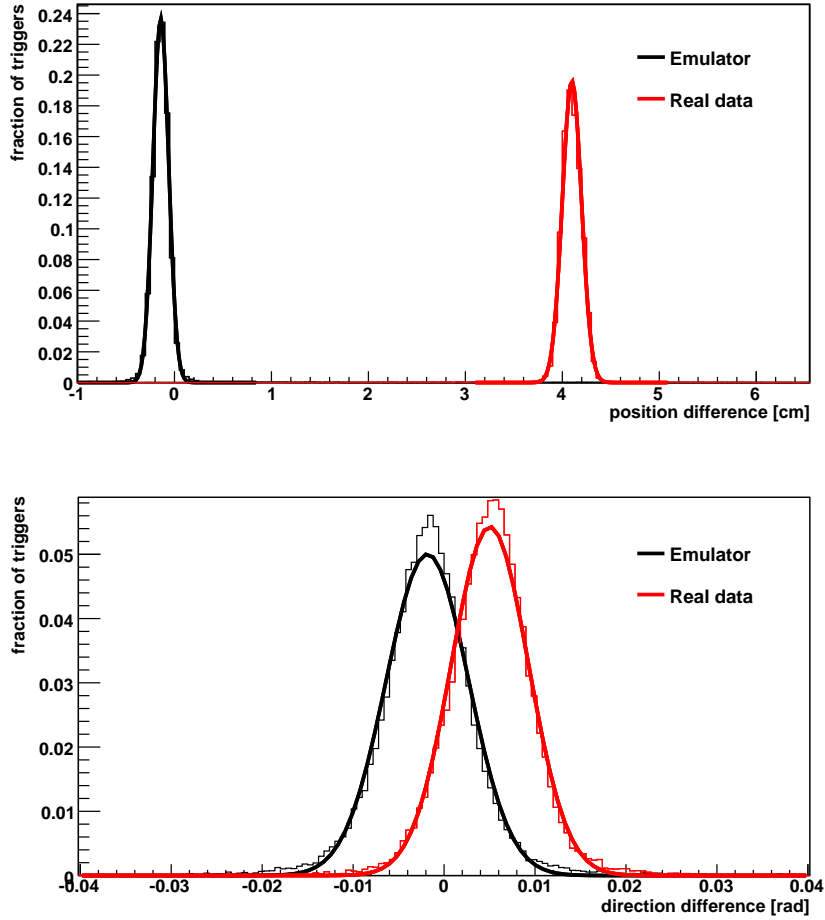


Figure 5.38: *Position (top) and direction (bottom) residual plots computed comparing trigger and local reconstruction information for MB2 stations of positive wheels. Black and red lines shows the system behaviour for emulator and real data respectively.*

tive wheels are shown for emulator (black) and real data (red). Emulated LUTs are dynamically computed by the software using the aligned detector geometry description. A systematic displacement of about 4 cm is found in real LUTs position whereas emulated ones are in good agreement with

segment reconstruction. This proves that the LUT displacement is due to a incorrect assignment of the hardware parameters which will be easily fixed. The RMS of Gaussian fits performed on the distribution are resported in table 5.4. They show that system resolution is almost unaffected by systematics displacement in LUTs computation. Up to now misalignment in  $\phi$  and  $\phi_B$  reconstruction have only slightly affected trigger functioning. This is related to the fact that the PHTF trigger is presently operated in open LUT mode. However these kind of problems will increase in importance as soon as the system will run with closed LUTs. Therefore a prompt identification and correction of such misbehaviours is mandatory to ensure good system performances at the LHC startup.

# Conclusions

In this thesis the performances of the CMS Drift Tubes Local Trigger System are studied. Results from data collected during the Cosmic Run At Four Tesla (CRAFT) commissioning exercise, a globally coordinated run period where the full experiment was involved, are presented. The DT Local Trigger has been a fundamental component of the data acquisition process since the beginning of the commissioning of the detector, therefore analysis concerning its functioning are relevant both to study the performances of the system itself and to validate the quality of the collected data.

Studies of the various aspects related to local trigger segment generation were carried out. The accuracy of the trigger reconstruction algorithm was investigated. Results coming from this analysis showed that the precision of positional and directional measurements is of 1 *mm* and 4 *mrad* respectively, in line with design expectations. The correct functioning of the ghost suppression mechanism was also tested and this study demonstrated that a low fraction of second tracks (of about 2-3%) is generated by the local trigger electronics when single muons cross the detector. Efficiency analysis were also performed and showed that the trigger correctly operates muon identification in about 95% of the cases in which a high quality muon track segment is also reconstructed offline. Good uniformity of the results among various sectors was found and about 50% of the delivered triggers have been proven to be generated using information coming from all the detecting layers of a chamber, again in line with the expectations. A comparison between the behaviour of the DT Local Trigger in absence and presence of the magnetic field was also carried out. The results of this test confirmed that, in the latter case, no evident worsening of the trigger performances is found.

The asynchronous nature of cosmic muons allowed to test the response of the system as a function of the particle time of crossing. The DT Local Trigger algorithm is in fact known to perform at its best when the signal

## CONCLUSIONS

---

produced by an incoming muon is detected in a timing region located at a fixed latency with respect to the trigger sampling phase. A dedicated study allowed to measure the position and the width of this region. This granted to develop a method that can be used to perform proper system synchronization at LHC.

A comparison between the results obtained by the hardware trigger and its software emulation was also performed. As a part of the work for this thesis the DT Local Trigger emulator was migrated to the software framework presently used by the experiment. Furthermore the code, developed to operate on simulation, was adapted to run smoothly on data coming from the real detector. A comparison between the outcomes of the hardware and the emulator has thus been performed. A statistical matching of the order 98% has been found and this allowed to use the emulator as a powerful tool to perform hardware validation studies.

Finally a large part of the software code developed for this study has been migrated to the online Data Quality Monitoring infrastructure of the experiment, and also included in the suite of programs used to perform prompt offline analysis. Both these instruments played an important role in the study of the quality of collected data, and will be used to perform validation of the samples used for offline physics studies as soon as LHC will start to produce collisions.

# Bibliography

- [1] D. Boussard et al., “*The Large Hadron Collider conceptual design*”, CERN/AC/95-05 (1995).
- [2] Lyndon Evans and Philip Bryant (editors), “*LHC Machine*” JINST 3 S08001D (2008).
- [3] LHC Homepage, <http://lhc.web.cern.ch/lhc/>
- [4] F. Halzen A.D. Martin, “*Quarks and Leptons: an introductory course on modern particle physics*”, Wiley (January 6, 1984), ISBN 0471887412.
- [5] G. Altarelli and M. L. Mangano (editors), “*Proceedings of the Workshop on Standard Model Physics (and more) at the LHC*”, CERN Yellow Report, CERN-2000-2004 (2000).
- [6] F.Gianotti, “*Collider Physics at LHC*”, CERN Yellow Reports 2000-07 (2000).
- [7] Particle Data Group, “*Review of particle Physics*”, Phys. Rev. D66 (2002).
- [8] P.Higgs, Phys. Rev. Lett. 12 (1964) 132 and Phys. Rev. 145 (1966) 1156; F.Englert and R.Brout, Phys. rev. Lett. 13 (1964) 321; G. Guralnik et al., Phys. Rev. Lett. 13 (1964) 585.
- [9] M. Spira and P. M. Zerwas, “*Electroweak symmetry breaking and Higgs physics*”, CERN-TH/97-379 (1997).
- [10] G. Altarelli and G. Isidori, “*Lower limit on the Higgs mass in the standard model: An update*”, Phys. Lett. B337 141 (1994).

## BIBLIOGRAPHY

---

- [11] T. Hambye and K. Riesselmann, “*Matching conditions and Higgs mass upper bounds revisited*”, Phys. Rev. D55 7255 (1997).
- [12] The LEP Working Group for Higgs boson searches, “*Search for the standard model Higgs boson at LEP*”, Phys. Lett. B 565 63, (2003).
- [13] Peter Renton “*Global Electroweak Fits and the Higgs Boson Mass*”, 34th International Conference on High Energy Physics (ICHEP 2008), arXiv:0809.4566 (Sep 2008).
- [14] The CMS Collaboration, “*CMS Physics Technical Design Report, Volume 1: Detector Performance and Software*”, CERN/LHCC 2006-001, (February 2006).
- [15] The CMS Collaboration, “*CMS Physics Technical Design Report, Volume 2: Physics Performance*”, CERN/LHCC 2006-021, (26 June 2006) and Journal of Physics G, Nuclear and Particle Physics, Volume 34, Number6, (June 2007).
- [16] F. Gianotti, M. Pepe Altarelli, “*Precision Physics at the LHC*”, hep-ex/0006016 (2000).
- [17] V Buege et al, “*Prospects for the precision measurement of the  $W$  mass with the CMS detector*”, CMS Note 2006-061 (2006).
- [18] S. P. Martin, “*A Supersymmetry Primer*”, hep-ph/9709356v5 (2008).
- [19] S. Heinemeyer, W. Hollik, D. Stockinger, A. M. Weber, G. Weiglein, “*Precise Prediction for  $m_W$  in the MSSM*”, JHEP 0608 052, (2006).
- [20] <http://www.ifca.es/~heinemey/uni/plots/index.html>
- [21] The CMS Collaboration, “*The Compact Muon Solenoid Technical Proposal*”, CERN/LHCC 94-34, LHCCp1 (1994).
- [22] The CMS Collaboration, “*The CMS experiment at the CERN LHC*”, JINST 3:S08004 (2008).
- [23] The CMS Collaboration, “*The Tracker Project: Technical Design Report*”, CERN/LHCC 98-6, CMS TDR 5 (1998).

## BIBLIOGRAPHY

---

- [24] The CMS Collaboration, “*Addendum To The Tracker Technical Design Report*”, CERN/LHCC 2000-016, CMS TDR 5 Addendum 1 (2000).
- [25] The CMS Collaboration, “*The Electromagnetic Calorimeter Project: Technical Design Report*”, CERN/LHCC 97-33, CMS TDR 4 (1997).
- [26] The CMS Collaboration, “*The Hadronic Calorimeter: Technical Design Report*”, CERN/LHCC 97-31, CMS TDR 2 (1997).
- [27] The CMS Collaboration, “*The Magnet Project: Technical Design Report*”, CERN/LHCC 97-10, CMS TDR 1 (1997).
- [28] The CMS Collaboration, “*The Muon Project: Technical Design Report*”, CERN/LHCC 97-32 (1997).
- [29] The CMS Collaboration, “*The Trigger And Data Acquisition Project, Volume 1, The L-1 Trigger: Technical Design Report*”, CERN/LHCC 2000-038, CMS TDR 6.1 (2000).
- [30] The CMS Collaboration, “*The Trigger And Data Acquisition Project, Volume 1, The High Level Trigger: Technical Design Report*”, CERN/LHCC 2002-26, CMS TDR 6.2. (2002).
- [31] F. Gasparini, M. Benettoni, E.Conti, G. Zumerle, “*Changes In The Design Of The CMS Barrel Drift Chambers*”, CMS IN 1999-05 (1999).
- [32] J. Puerta-Pelayo, M.C. Fouz and P. Garcia-Alba, “*Parametrization of the Response of the Muon barrel Drift tubes*”, CMS NOTE 2005/018 (2005).
- [33] R. Veenhof, “*Garfield, a Drift-Chamber Simulation Program user’s guide*”, CERN Program Library W5050 (1994).
- [34] M. Andlinger et al., “*Bunch crossing identification at LHC using a mean timer technique*”, Nuclear Instrumentation and Methods, A336:91-97 (1993).
- [35] M. Aguilar-Benítez et al., “*Construction and test of the final CMS Barrel Drift Tube Muon Chamber prototype*”, Nucl. Instrum. Meth. A480 (2002).

## BIBLIOGRAPHY

---

- [36] M. Cerrada et al., “*Results from the Analysis of the Test Beam Data taken with the Barrel Muon prototype Q4*”, CMS NOTE 2001/041 (2001).
- [37] M. Aguilar-Benítez et al, “*Study of magnetic field effects in drift tubes for the barrel muon chambers of the CMS detector at LHC*”, Nucl. Inst. Meth. A416 243 (1998).
- [38] C. Albajar et al., “*Test beam analysis of the first CMS muon chamber*”, Nucl. Inst. Meth. A525 465 (2004).
- [39] F.R. Cavallo et al., “*Test of MB3 Muon Barrel Drift Chamber with Cosmic Rays*”, CMS Note (2003) 2003/017 (2003).
- [40] R. Martinelli, A. J. Ponte Sancho, P. Zotto, “*Design of the Track Correlator for the DTBX Trigger Status*”, CMS NOTE 1999-007 (1999).
- [41] A. Montanari, “*Track Sorter Slave Reference Manual*”, CMS NOTE 2002-011 (2002).
- [42] I. D’Antone, G. M. DallaValle, S. Marcellini A. Montanari, F. Odorici, G. Torromeo, “*Track Segment Sorting in the Trigger Server of a Barrel Muon*”
- [43] C. Grandi and S. Marcellini, “*Simulation of the Trigger Server of a Barrel Muon Station in CMS, CMS IN 2001-028 (2001). Station in CMS*”, CMS TN 1996-078 (1996).
- [44] L. Guiducci. “*Design and test of the Off-Detector Electronics for the CMS Barrel Muon Trigger*”, CMS-TS 2006-010, (2006).
- [45] *CMSSW Application Framework*,  
<https://twiki.cern.ch/twiki/bin/view/CMS/WorkBookCMSSWFramework>
- [46] *Framework and Event Data Model Offline Guide*,  
<https://twiki.cern.ch/twiki/bin/view/CMS/SWGuideFrameWork>
- [47] *Description of the cmsRun Python Configuration Syntax*,  
<https://twiki.cern.ch/twiki/bin/view/CMS/SWGuideAboutPythonConfigFile>
- [48] *The CMS Database Project*,  
<https://twiki.cern.ch/twiki/bin/view/CMS/DatabaseWikiHome>

## BIBLIOGRAPHY

---

- [49] M. Aldaya, P. Garcia-Alba, “*Measurement of the charge ratio of cosmic muons using CMS data*”, CMS NOTE 2008-016 (2008).
- [50] A.Perrotta “*Commissioning and Early Measurements of the DT Muon Detector of CMS at the LHC*”. CMS CR 2008-91 (2008).
- [51] P. Arce et al., “*Bunched beam test of the CMS drift tubes local trigger*”, Nucl. Instrum. Meth. A534:441-485 (2004).
- [52] M. Aldaya et al., “*Results of the first integration test of the CMS drift tubes muon trigger*”, Nucl. Instr. Meth. A579:951-960 (2007).
- [53] M. Aldaya et al, “*Fine synchronization of the CMS muon drift tubes local trigger* Nucl. Instum. Meth. A564:169-177 (2006).